A STUDY OF TRIMUON AND DIMUON EVENTS PRODUCED BY 10.5 GEV μ^- ON LEAD

BY

JOSEPH A. LE BRITTON

Ph.D. Thesis

THE UNIVERSITY OF ROCHESTER

DEPARTMENT OF PHYSICS AND ASTRONOMY

ROCHESTER, NEW YORK

A STUDY OF TRIMUON AND DIMUON EVENTS PRODUCED BY 10.5 Gev μ^- ON LEAD

by

Joseph A. Le Britton

Submitted in Partial Fulfillment
of the
Requirements for the Degree

DOCTOR OF PHILOSOPHY

Supervised by Professor A. C. Melissinos
Department of Physics and Astronomy

The University of Rochester
Rochester, New York

1979

VITAE

Joseph Andrew Le Britton was born on October 4, 1953 in Worcester, Massachusetts. He graduated from Shrewsbury High School in Shrewsbury, Massachusetts in 1971 and entered Worcester Polytechnic Institute. Majoring in physics, he received the Bachelor of Science degree with high distinction in June 1975. While at WPI he participated in research on theoretical general relativity and experimental studies of electron paramagnetic resonance in solids.

In the summer of 1975 he entered the University of Rochester and began working with Dr. Adrian C. Melissinos on the construction of Experiment AGS632 (muon-nucleus scattering). During the school years of 1975-6 and 1976-7 he was a teaching assistant in Introductory Electricity and Magnetism, Modern Physics, and Mechanics Lab. He worked on the analysis of a prototype muon focussing lens for high energy muon beam transport in the summer of 1976. After finishing course work at Rochester, he began working full time at Brookhaven National Laboratory for the Rochester-BNL-NSF collaboration on the analysis of Experiment 632 (the subject of this thesis) and the running and analysis of Experiment AGS687 (dimuon production in π N interactions). He lived at Brookhaven from June 1977 to December 1978 during which time he was supported as a Research Assistant by the University of Rochester.

ACKNOWLEDGEMENTS

I am indebted to Dr. Adrian Melissinos for the opportunity to have worked with him during my years at Rochester. Not only is he an energetic and knowledgable physicist, but his good nature and wit make graduate school a pleasure, not the long hard struggle it is reputed to be. I will always remember the enjoyment derived from his never-ending enthusiasm and appreciation for physics.

The series of two muon experiments on which I have worked were the combined efforts of Josh Alspector, Sam Borenstein, George Kalbfleisch, Dick Strand, and Jim Scharenguival of Brookhaven National Laboratory, Al Abashian of the National Science Foundation, and Bill Metcalf, Dennis McCal, Marty Miller, Adrian Melissinos, and myself from the University of Rochester. I have worked closely with each of them and consider myself fortunate to have been involved with such a small friendly group of fine physicists.

In particular, I thank Bill Metcalf for the years he's spent as my friend, colleague, and teacher. The success of the experiments is primarily due to his firm knowledge and long hours of hard work. My fellow graduate students Dennis McCal and Marty Miller deserve special thanks for their work on the construction and analysis of the experiments and for their companionship during the hundreds of hours at the desks and computers.

I thank Jack Sanders of Brookhaven, whose numerous talents and good humor were invaluable over the years. His friendship and efforts above and beyond the call of duty are appreciated by all of us.

I am indebted to the staff of the Rochester Cyclotron Lab for their work on the construction of the apparatus. In particular, thanks go to Ray Soosar for his efforts and the many interesting conversations. Amine Marzouk's work in the machine shop and Al Covert's work on the drawings were essential to the completion of the experiments. I thank Dave McCumber and Brian Wormington for work on the design of the electronics, which functioned flawlessly.

A well-deserved thanks goes to the technicians at Brookhaven, most notably Penny Austin for her cheerful attitude and valuable aid in the computing, Ed Frantz for keeping the electronics in good working order, and Marty Van Lith for his assistance in the construction and maintenance of the apparatus.

I would like to thank Dr. Steve Olsen for his help in the design of the chambers and for the many good times. I thank Dr. Kwan-wu Lai for his continued interest in our work.

The staff of the Rochester Physics Department has helped me over many hurdles. I thank Betty Cook for her continued interest in helping myself and all of the students. Special thanks are due Edna Hughes for her flawless

preparation of the manuscripts. I am indebted to Mike Anthony and Betty Bauer for helping me through the frequent administrative red tape.

Perhaps more than anyone else, it is my friends who have helped make my graduate career a success. It was their support that provided the day to day motivation. To mention them all could fill pages, but I am particularly ingratiated to Drs. Jolie Cizewski, Gary Warren, Frank Bletzacker, Bill Rish, and Norman Kanter, Messrs. Andy Haas, Tove Matas, Dave Schultz, Paul Ganci, and Fried Elliot, and Ms. Liz Howard.

Finally, I dedicate this thesis to my family; my sisters Jane, Diann, and Kathy, and especially my parents Joe and Mary. Without their encouragement and support my education would not have been possible.

ABSTRACT

In a general study of muon-nucleus scattering at the Brookhaven National Laboratory Alternating Gradient Synchrotron's 10.5 Gev muon beam, we have observed 158 trimuon and 637 dimuon final states using a leadglass target. The sensitivity of the experiment was approximately one event per picobarn per nucleon. It is shown that the majority of the trimuon events are due to muon trident production. The total and differential cross sections are in excellent agreement with the predictions of quantum electrodynamics. In addition, it is shown that muons obey Fermi-Dirac statistics at a confidence level of 8 standard deviations. About 10% of the trimuons appear to be due to other processes, most probably diffractive production of the ρ^0 meson by virtual photons. Upper limits are given on the production and decay of particles possessing a three-muon decay mode and on the inelastic virtual photon Compton scattering cross section. The dimuon events can be entirely accounted for by tridents where one muon lies outside of the acceptance and by the production and muonic decay of π and K mesons. Upper limits on prompt single muon production are given.

TABLE OF CONTENTS

LIST OF TABLES

LIST OF FIGURES

CHAPTER 1

PROMPT MUON PRODUCTION

1A. INTRODUCTION

Muon production with muon beams is a largely unexplored phenomenon exhibiting a great variety of physical processes of interest in the contemporary study of elementary particles. In addition to testing the predictions of conventional models, prompt muon production has the potential for revealing unexpected new physics. The possibilities range from testing quantum electrodynamics to observing the production and muonic decay of new particles. Indeed, the study of such interactions can only lead to a better understanding of the muon, whose role in the family of elementary particles has remained a puzzle since its discovery in 1937[1].

The results presented here represent the study of two and three muon final states as part of a larger investigation of muon-nucleus interactions at 10.5 Gev/c incident momentum. Experiment AGS632 was mounted and performed in

the East Experimental Area of the Brookhaven National Laboratory Alternating Gradient Synchrotron from 1974 to 1976. Other motivations were to measure the atomic number dependence of deep inelastic muon scattering[2] and to test scaling and the parton model[3].

1B. MUON TRIDENTS

The 'muon trident' process is the coherent production of a muon pair by an incident muon in the field of a target nucleus. The four first-order Feynman diagrams for the reaction are shown in Figure 1-1. The reaction's primary significance is that it can be used to test muon electrodynamics and statistics. Since it is a pure quantum electrodynamic process, theory makes specific predictions on the size and form of the differential cross sections. The presence of two identical muons in the final state allows a check of muon statistics. The existence of fermion exchange between muons has not been well measured, yet it is essential to do so in the interest of the fundamental muon-electron universality puzzle[1].

The spin-statistics theorem of quantum electrodynamics was first proven by Pauli in 1940[4]. It states that non-zero half-integer spin fields must obey Fermi-Dirac statistics, while fields with integer spin obey Bose-Einstein statistics[5]. This has been well-proven experimentally in the cases of stable particles. Electrons are known to be fer-

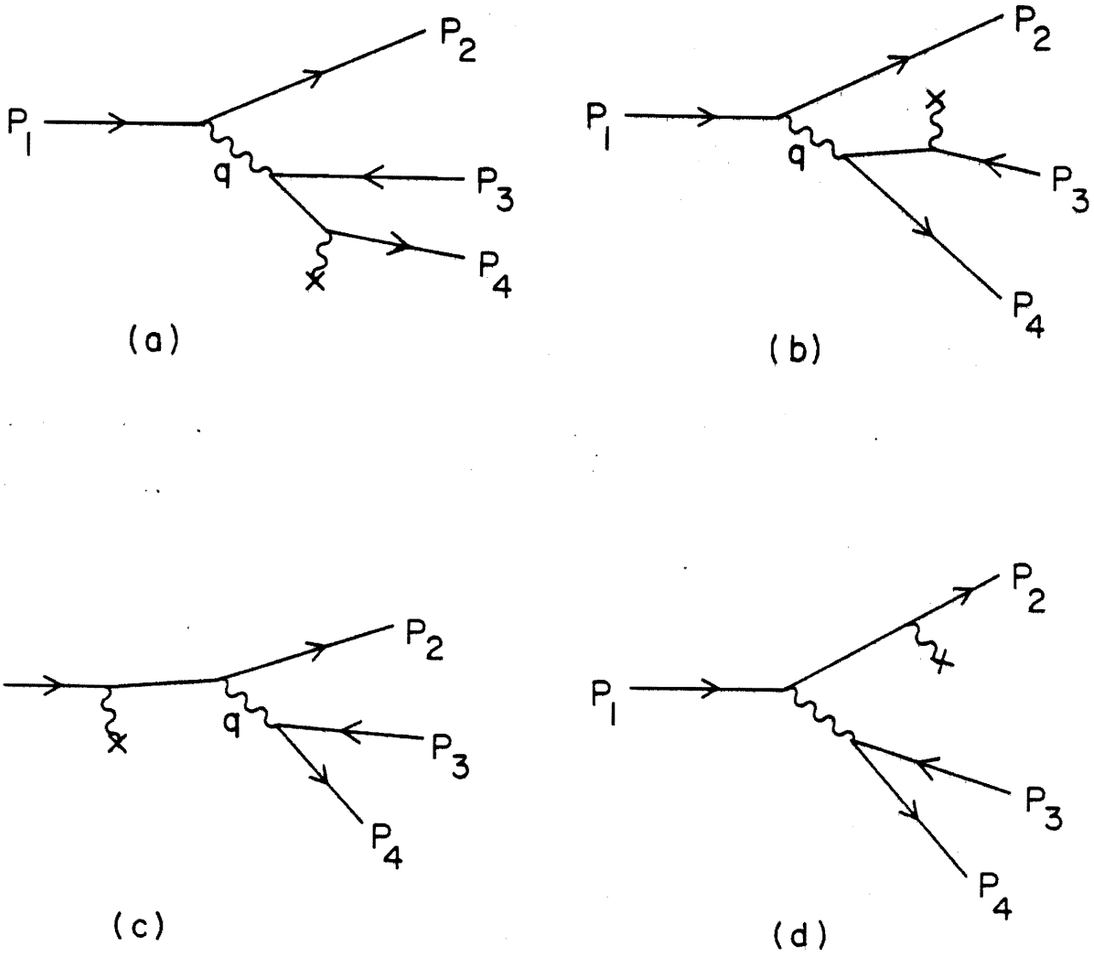

Figure 1-1. The four first order (one photon) Feynman diagrams for the muon trident process. In (a) and (b) the incident muon pair-produces muons off the nucleus via a spacelike virtual photon. In (c) and (d) the beam muon 'dissociates' into a muon pair via a timelike virtual photon.

mions from atomic structure, while nucleons are known to obey the Pauli principle from the shell structure of nuclei. The black body radiation spectrum indicates that photons obey Bose-Einstein statistics. However, in the regime of unstable particles, it is extremely difficult to experimentally observe a system containing two identical particles. In this regard tridents are unique. To date, this reaction presents the only opportunity to directly measure this fundamental property of muons.

The first electron trident experiment was performed by Criegee et al.[6] with a 31.5 Mev electron beam on a copper target. The corresponding process for muons occurs at higher energies ($\sim$6 Gev incident energy to achieve the same yield). Due to the lack of intense high energy muon beams in the 1960's, muon tridents could only be seen with cosmic rays. Morris and Stenerson[7] obtained a total cross section σ = 2 μb per nucleon, far in excess of the expected .04 μb per nucleon from a calculation of Murota, Ueda, and Tanaka[8]. Barton and Rogers[9] found an upper limit of .4 μb per nucleon compared to the predicted value of .002 μb per nucleon. (These cross sections correspond to the yield expected in each particular apparatus).

It was not until a calculation by Brodsky and Ting[10] that the complete expression for the trident differential cross section was given. Subsequent analysis was carried out by a number of theorists[11]. The complexity of the ma-

trix elements make them difficult to evaluate. Tannenbaum[12] was able to integrate the differential cross section using a Monte Carlo technique. This method will be described in detail in section 3B. The cross section was finally measured reliably by Russell et al.[13] with 10.5 Gev muons on lead at the AGS. Their measured cross section integrated over the apparatus was 51 $\pm$ 7 nb per lead nucleus, which agrees well with the QED prediction of 60 $\pm$ 2 nb per nucleus.

The antisymmetry of the final state of the trident process under the interchange of the two identical muons introduces four exchange amplitudes in addition to the four normal amplitudes shown in Figure 1-1. The interference of normal and exchange amplitudes depresses the total cross section. This depression arises in that region of phase space where the wave functions of the two like-charge muons overlap significantly, that is, where they have a small opening angle and similar momenta (i.e. low effective mass, see section 3B). Hence, both the total cross section and the shape of the effective mass distribution of the two identical muons should reflect fermion exchange between muons. Russell et al.[13] observed this effect, as can be seen in their effective mass distribution (Figure 1-2). In addition, their total cross section is about 40% below the expected 82 $\pm$ 2 nb per nucleus if muons did not undergo fermion exchange. This was the first clear evidence that muons obey Fermi-Dirac statistics.

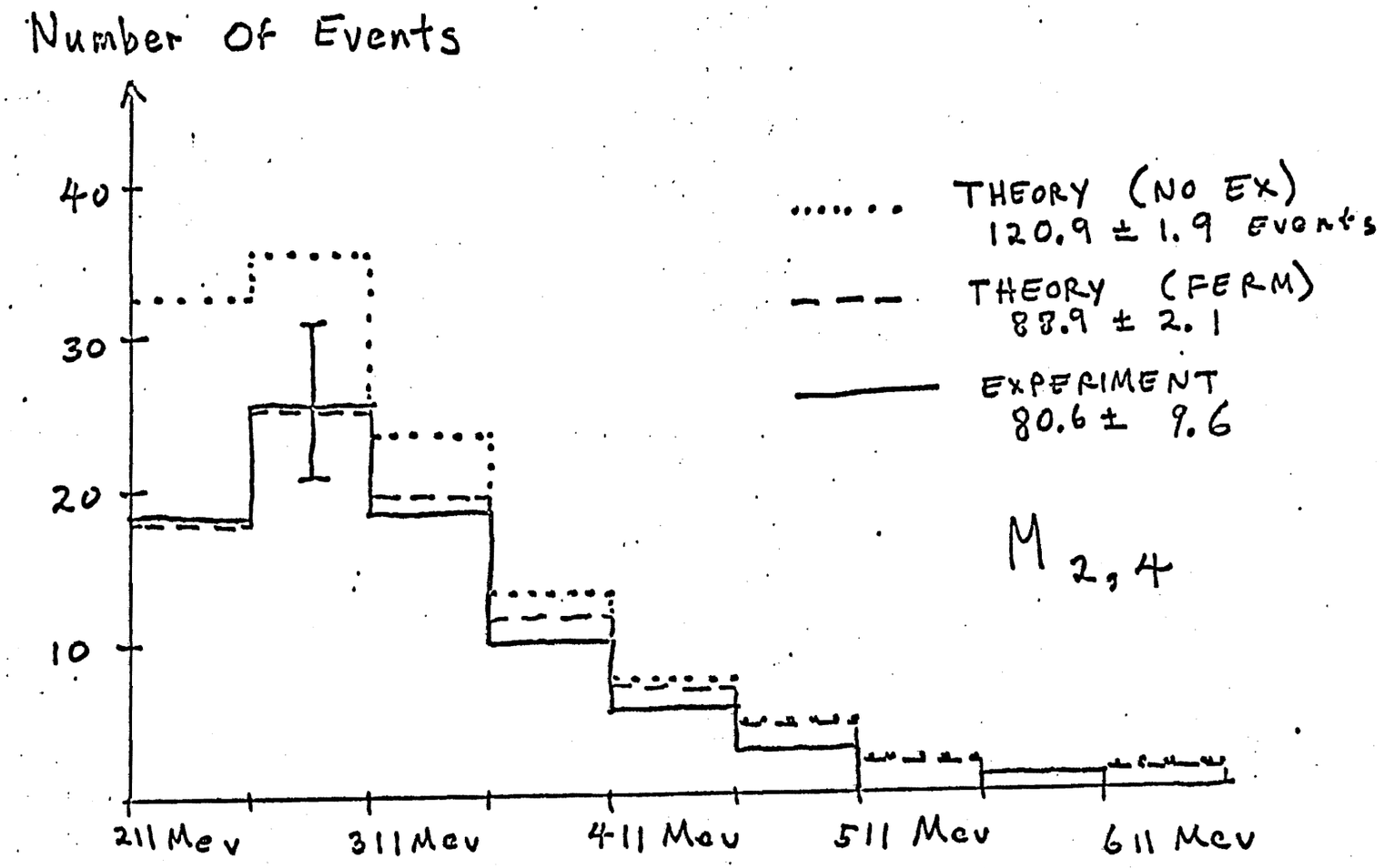

Figure 1-2. The effective mass distribution of the two like-charge final state muons from the muon trident experiment of reference 13. The suppression of events at low mass is the signature of fermion exchange between muons.

1C. OTHER TRIMUON PROCESSES

While we expect the trident process to be the dominant mechanism for trimuon production in this energy region, other processes must be considered. One possible reaction is the diffractive production of vector mesons by virtual photons with subsequent decay into a muon pair[14].

$$\gamma_v + \mathrm{Pb} \rightarrow \underbrace{V^o}_{\hookrightarrow\, \mu^+\mu^-} + \mathrm{Pb} \qquad V^o = \rho\,,\omega,\phi\,,\psi,\ldots \tag{1.1}$$

Examples of this process are shown in Figures 1-3a-d. Pomeron exchange (diffraction, Figure 1-3a) is predicted in the vector dominance model to be roughly energy independent and dominant where the four-momentum t transferred to the nucleus is low. In this region, the process is coherent off the nucleus ($\sim A^2$), while at large t it becomes incoherent ($\sim A^1$). At low energies, an energy dependence can arise from low-lying Regge trajectories (ρ',f). Production of the ρ meson in this way is not expected to mask out the trident signal since tridents are produced predominantly at low mass and the cross section falls very steeply with mass. Also, the low-mass vector mesons have such small branching ratios into muon pairs that their $\mu^+\mu^-$ signal is strongly suppressed. However, diffractive production roughly balances energy and thus can only be distinguished from QED tridents in terms of the predicted kinematics.

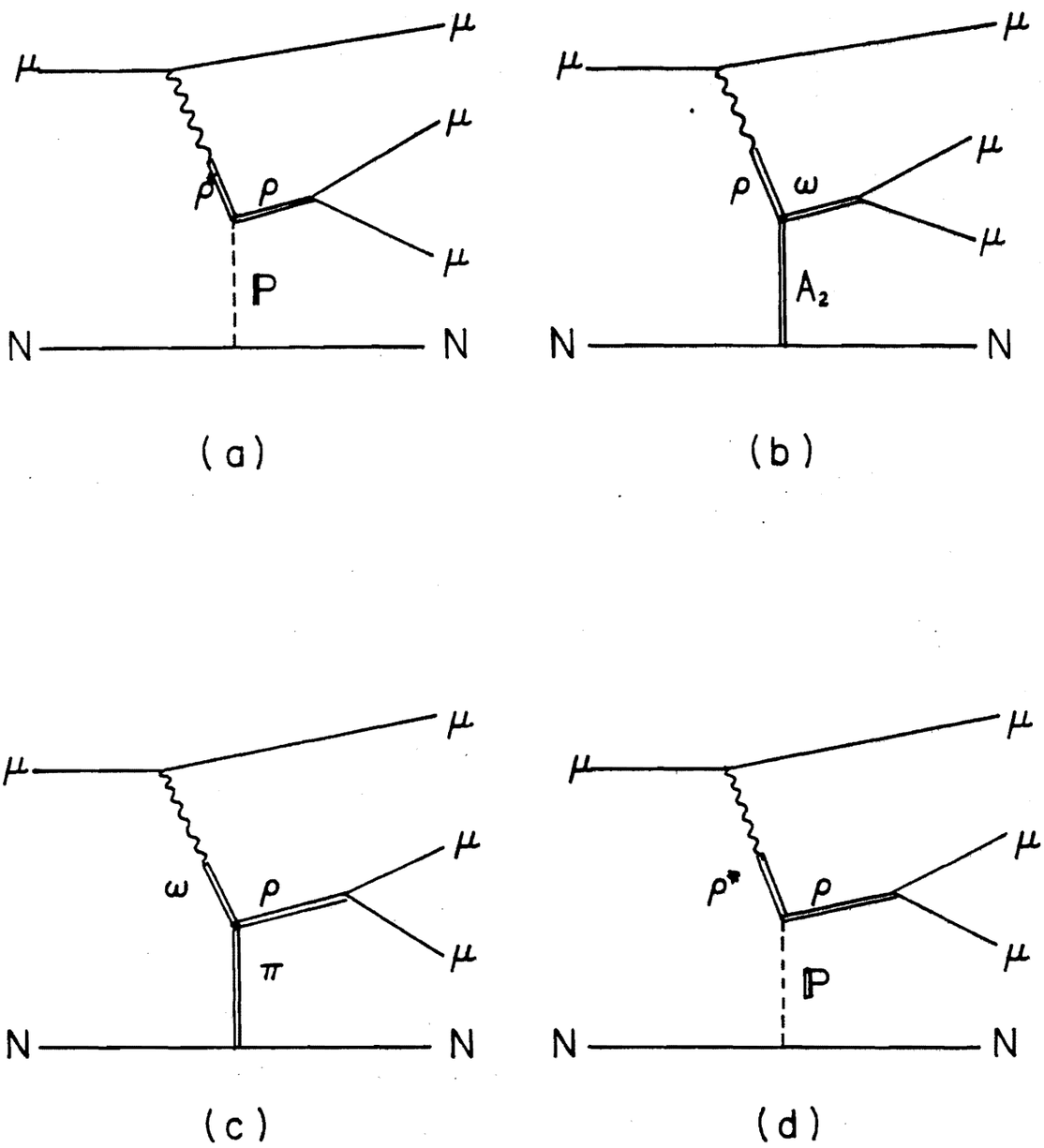

Figure 1-3. Vector meson production by virtual photons as a source of trimuons. (a) coherent Pomeron exchange, (b) and (c) quantum number exchange and (d) incoherent Pomeron exchange.

One can consider other VMD processes such as quantum number exchange, examples of which are shown in Figures 1-3b,c. These types of reactions do not balance energy and are incoherent (since the exchanged field must somehow alter the target nucleus). They represent a non-negligible background only in a high-statistics experiment and in fact are most negligible for heavy nuclei such as lead. Another possibility is production in which the nucleus or nucleon is left in an excited state (Figure 1-3d)

$$\gamma_v + N \rightarrow V^o + N^* \qquad (1.2)$$

Again, this is expected to be small in comparison to coherent Pomeron exchange, yet can be indistinguishable from it since the missing energy can be very small.

Photoproduction (both real and virtual photons) of vector mesons has been studied quite extensively experimentally on a wide variety of nuclear targets[15,16]. These experiments must detect the $\pi^+\pi^-$ decay mode in order to obtain high statistics, since thier primary goal is to extract vector dominance model parameters (namely the photon-vector meson coupling, the $\gamma N \rightarrow V^o N$ cross section,and the real part of the scattering amplitude). Many complications arise in the analysis of such data, so useful results can only come from precision measurements.

Since a ρ-decay trimuon involves the highly-suppressed $\mu^+\mu^-$ decay mode (BR = 7×10^{-5}) a high statistics test of VMD is not possible here. However, since this may contribute to the background under the QED trident process, the previously recorded accurate data allow a realistic estimate of its contribution. This is discussed further in section 5B.

Experiments on the photoproduction and electroproduction of muon pairs have revealed that the total $\mu^+\mu^-$ production cross section is significantly higher than that predicted from Bethe-Heitler production and meson decay alone[17]. One process that may account for part of this excess yield is Compton scattering of a photon off of a nucleon constituent (parton) followed by the decay of the scattered (virtual) photon into a muon pair (Figure 1-4). A theoretical calculation of this mechanism has been performed[18] in the interest of accounting for the prompt muon yields from high energy muon beams[19].

While the Compton process can reveal information on the structure and properties of nucleon constituents, it is a difficult one to detect and analyze experimentally. The total cross section is very small ($\sim$ 5 pb per nucleon) and does not vary appreciably with energy. This estimate is close to the sensitivity of this experiment ($\sim$1 pb per nucleon), so we might optimistically expect a few events. Although this reaction occurs at a level well below the

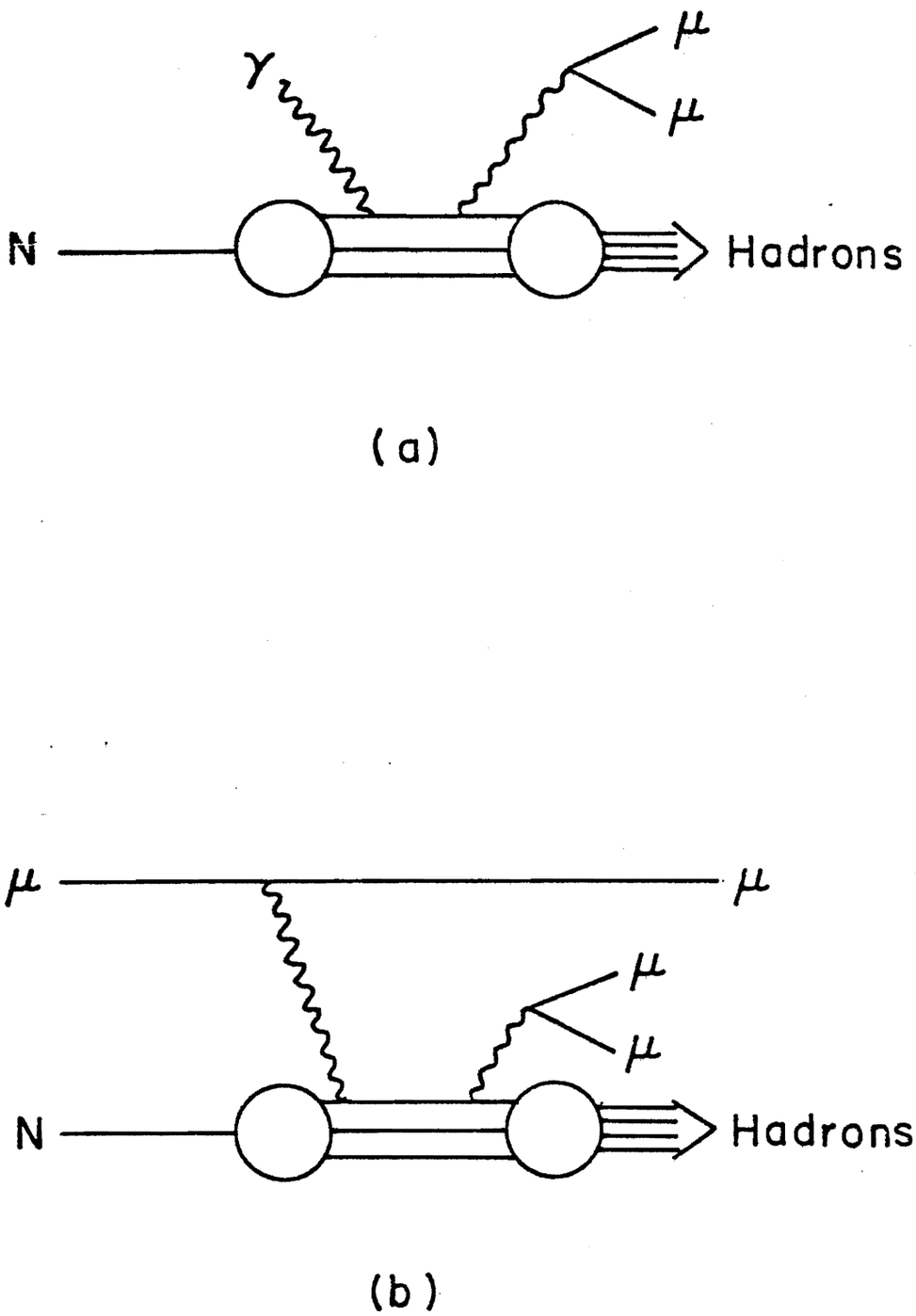

Figure 1-4. Inelastic Compton scattering as a source of prompt muon pairs from (a) real and (b) virtual photons.

radiative and Bethe-Heitler trident mechanisms, it is sufficiently different kinematically that appropriate cuts can separate the two. For example, in trident production very little energy is transferred to the target and a substantial fraction of the incident energy can be given to the produced muon pair. On the other hand, Compton pair production off a parton is an inelastic process off the nucleon and characteristically has a fast scattered muon and very slow produced muons in the final state. This can be seen in Figure 1-5 where the predicted energy spectrum of the two like-charge muons as given in reference 21 is shown. At FNAL energies there is some hope of detecting all three muons (at 200 Gev, the scattered muon is predicted to have typically 185 Gev while the produced muons have $\sim$4 Gev). At AGS energies, the three muons have much less energy to share ($\sim$ 10 Gev). The fact that energy-symmetric final states are the events with the best acceptance (see section 5A) compounds the difficulty of the measurement. Results on a search for this process are discussed in section 5C.

Finally, it is altogether possible that trimuons with muon beams could arise from an exotic process unrelated to the better known mechanisms discussed above. A clear signature of new physics would be an enhancement in the three-muon mass distribution. Perhaps there exists a heavy charged lepton accessible at AGS energies which carries the muon quantum number and thus could possess a three muon decay mode. Pati and Salam[20] have conjectured that a quark

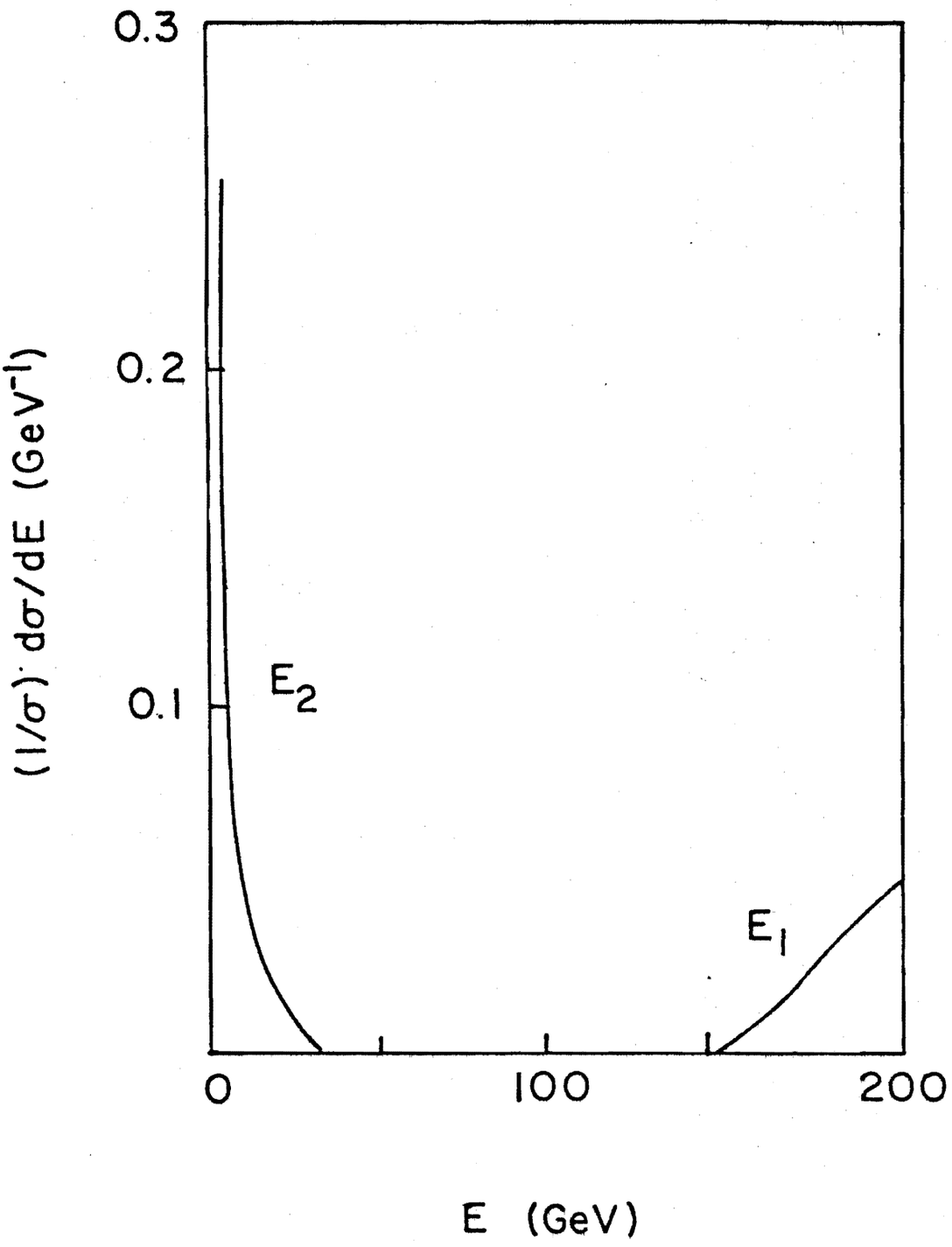

Figure 1-5. The theoretical distribution of the energies of the two like-charge muons produced in virtual photon Compton scattering as given in reference 21.

may dissociate into three muons. Another possibility is that muons can undergo an electric dipole transition into an excited state μ^* in the field of the target nucleus (Primakoff effect[21]) and then decay into three muons (see Figure 1-6). In section 5C upper limits on the production and decay of such objects are given.

1D. MUON PAIRS

We have searched for the process

$$\mu^- + N \rightarrow \mu^-\mu^\pm + X \qquad (1.3)$$

in which a single muon is detected in addition to the scattered muon. Such a 'pairs signal' is not expected on the basis of conventional models, but could result, for example from the production and decay of an exotic neutral particle which carries the muon lepton number

$$\mu^- + p \rightarrow M^o + n \qquad (1.4)$$
$$\hookrightarrow \mu^+\mu^-\nu$$

as predicted by some gauge theories[22].

Prompt single muons have been studied at FNAL energies and have been attributed to the decay of charmed particles produced in deep inelastic muon scattering[23]. Another possibility is the (radiative or hadronic) production of a pair

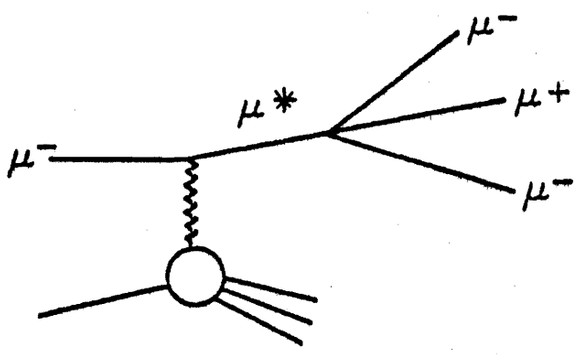

Figure 1-6. Primakoff excitation of a 'heavy muon' in the field of a target nucleus.

of heavy leptons, one of which decays into $\mu \nu \nu$. While these processes are of considerable interest in studying the new particles, they have no relevance to the data quoted here. At a beam energy of 10.5 Gev/c, the maximum virtual photon-nucleon center of mass energy W is approximately 4.5 Gev. This is to be compared with the charm threshold of $\sqrt{s}$ = 4.7 Gev and τ threshold of $\sqrt{s}$ = 4.6 Gev. Hence, any prompt muons seen at this energy cannot be explained by the decay of known new particles.

The main difficulty in extracting a prompt muon signal is the background from conventional processes, which may overwhelm the expected low level of exotic reactions. First, muon trident production in which one muon lies outside of the experimental acceptance will appear as a dimuon. Secondly, at these energies (3-4 Gev per final state muon on the average) the muonic decay of π and K mesons produced in a deep inelastic collision is indistinguishable from a genuine prompt muon. Any signal must first be analyzed in terms of these backgrounds before new physics can emerge. The detailed study of these processes is described in Section 5E.

Even if a source of prompt muons at this energy cannot be established, the experimental sensitivity of about 1 picobarn per nucleon places limits on such a reaction.

REFERENCES

1. A. Entenberg, University of Rochester thesis,1974 (unpublished)

2. G. Grammer and J. Sullivan in Electromagnetic Interactions of Hadrons, Vol. 2 (1978), A. Donnachie and G. Shaw eds.

3. J. Bjorken, Phys. Rev. 179, 1547 (1969)

4. W. Pauli, Phys. Rev. 58, 716 (1940)

5. R. Streater and A. Wightman, PCT, Spin, Statistics and All That (Benjamin, New York, 1964)

6. L. Criegee et al., Z. Physik 158, 433 (1960)

7. M. Morris and R. Stenerson, Nuovo Cimento 53B, 494 (1968)

8. Murota, Ueda, and Tanaka, Progr. Theoret. Phys. (Kyoto) 16, 482 (1956)

9. J. Barton and L. Rogers, Proc. of the 11th Int. Conf. on Cosmic Rays, Vol. 4, Budapest, Hungary (1969)

10. S. Brodsky and S. Ting, Phys. Rev. 145, 1018 (1966)

11. J. Bjorken and M. Chen, Phys. Rev. 154, 1335 (1967); G. Reading Henry, Phys. Rev. 154, 1534 (1967); G. Homma et al., J. Phys. Soc. Jap., 36, 1230 (1974)

12. M. Tannenbaum, Phys. Rev. 167,1308 (1968)

13. J. Russell et al., Phys. Rev. Letts. 26, 46 (1971)

14. H. Traas and D. Schildknecht, Nucl. Phys. B14, 543 (1969)

15. See for example H. Alvensleben et al., Nucl. Phys. B18, 333 (1970)

16. See for example C. del Papa et al., Phys. Rev. D19,1303 (1979)

17. D. Caldwell et al., Phys. Rev. Letts. 33, 868 (1974); J. Davis et al., Phys. Rev. Letts., 19,1356 (1972)

18. V. Ganapathi and J. Smith, Phys. Rev. D19, 801 (1979)

19. C. Chang et al., Phys. Rev Letts. 39,519 (1977)

20. J. Pati and A. Salam, Phys. Rev. Letts. 31,661 (1973); Phys. Rev. D10, 275 (1975)

21. H. Primakoff, Phys. Rev. 81, 899 (1951)

22. J. Bjorken and C. Llewelyn-Smith, Phys. Rev. D7,887 (1973)

23. F. Bletzacker and H. T. Nieh, SUNY-Stony Brook preprint ITP-SB-77-44 (unpublished)

CHAPTER 2

THE EXPERIMENT

2A. BEAM

The AGS muon beam is situated on the C-line of the East Experimental Area. It was initially designed by a Harvard-Columbia-Rochester group[1] and later upgraded to 10.5 Gev/c [2]. The beam line is shown in Figure 2-1. Protons from the AGS are incident on the C target which is followed at 0° by a system of quadrupoles (Q1-Q5) tuned to a momentum $<p>$ = 16 Gev/c. Pions are then momentum-selected with a series of three dipoles (D1-D3) of total bend angle 5.4°. The momentum slit which can accept up to $\Delta p / p = \pm 10\%$ is located at dipole D3. The pion decay path is 18 meters long with three quadrupoles (Q6-Q8) to focus the decay muons onto the hadron absorbers. These absorbers consisted of 1.2 meters of Carbon and a total of 6 meters of Beryllium, or 16 pion absorption lengths. Muons undergo an energy loss of $\sim$3 Gev in the filters and multiple scattering of $\Delta\theta_{rms}$ = 8.00 mrad. Muons are next momentum selected by a dipole

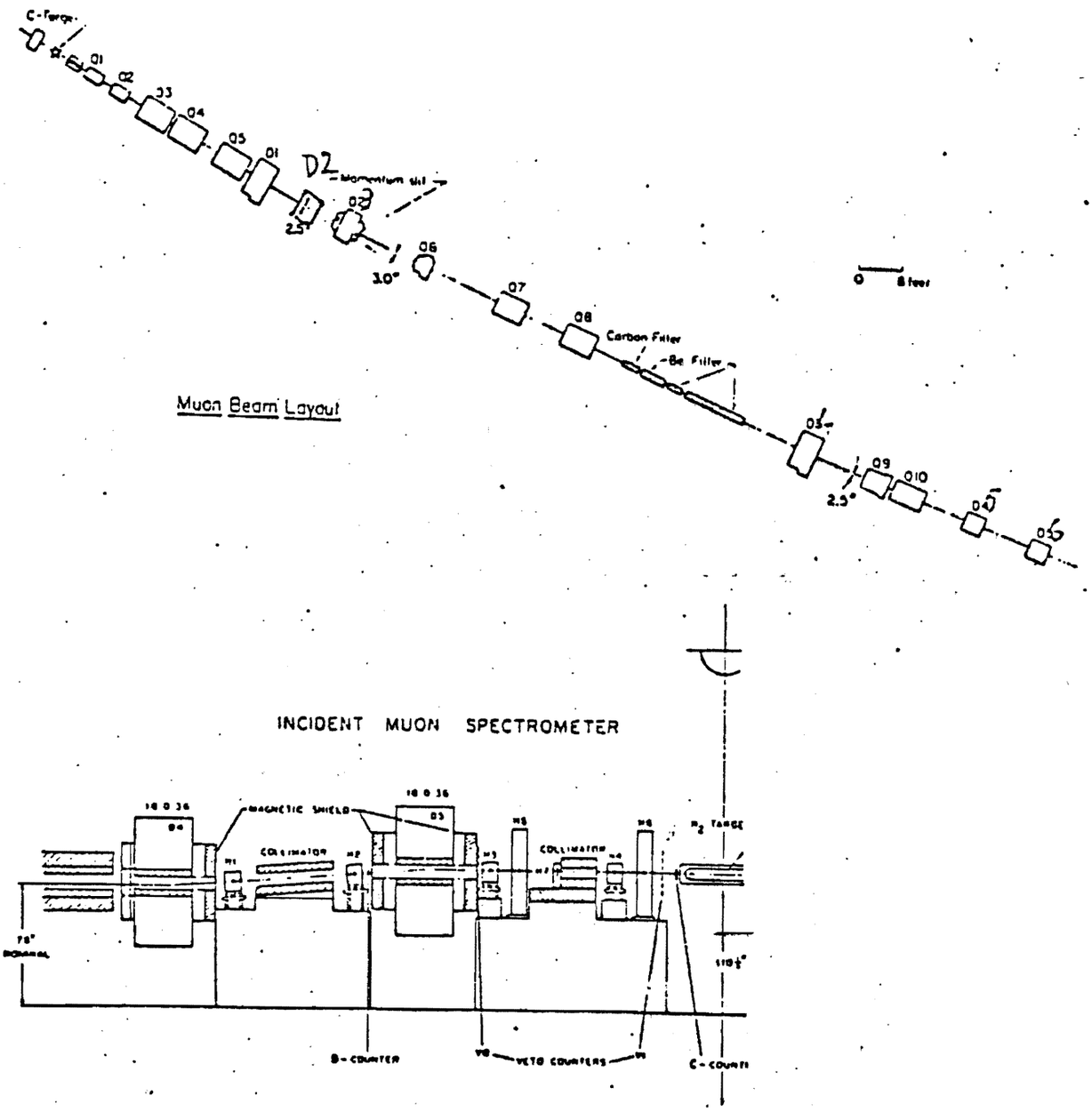

Figure 2-1. The muon beam on the C1 line of the Brookhaven AGS. At the bottom is shown the system of magnets and hodoscopes used to tag the momentum of incident beam muons.

(D4) with a 2.97° bend and then focussed with a quadrupole doublet (Q9-Q10). Collimation was further aided by gun-barrel concrete blocks.

The beam is then defined and momentum analyzed in the following way. It is pitched upward 50 mrad by dipole D5 and then brought back to horizontal by dipole D6. This trajectory is monitored by an entrance hodoscope system of seven planes (H1-H7) containing a total of 218 elements. In addition, three 5"x5" beam definition counters are placed in the system (A,B,C counters) with the C counter at the entrance to the experiment. A wall of veto counters (V) surrounded the entrance to suppress accidental triggers from the beam halo (the halo to beam ratio was 2 to 1).

A valid veam track was defined as the counter combinations

$$\text{BEAM} = A \cdot B \cdot C \cdot (H1 \ldots H7) \cdot \bar{V} \qquad (2.1)$$

The hodoscope system was cross-calibrated by measuring the momentum of beam muons allowed to pass through the spectrometer. The measured beam spectrum is shown in Figure 2-2 with $\langle p \rangle$ = 10.5 Gev/c and FWHM = 2.6 Gev/c. Table 2-1 gives the geometrical parameters of the beam at the target entrance. Typical fluxes were $.6 \times 10^6$ μ^- or 1.8×10^6 μ^+ per AGS pulse of 10^{12} protons on the C target.

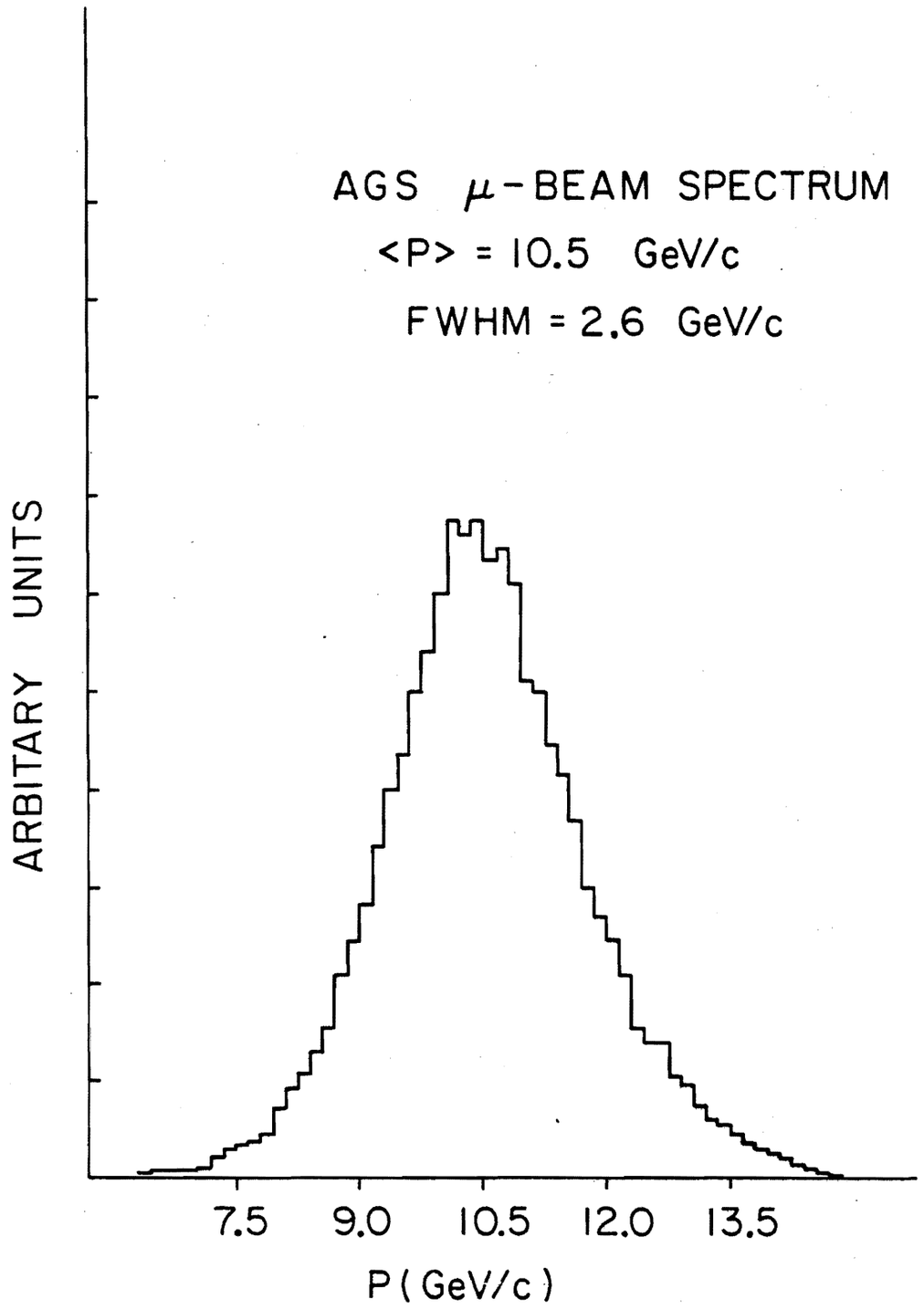

Figure 2-2. The measured muon beam momentum spectrum

TABLE 2-1

Muon Beam Parameters

Momentum	10.5 Gev/c
Horizontal size (FWHM)	6.3 cm
Vertical size (FWHM)	6.6 cm
Horizontal angular spread	13 mrad
Vertical angular spread	11 mrad
Halo to beam ratio	2/1
Pion contamination	< .01%

2B. MAGNET

The wide-aperture spectrometer is shown in Figure 2-3. The trajectories of particles crossing the spectrometer are bent due to the 120D36 dipole magnet. Its integrated field strength was $\int Bdl \sim 10$ kG-m, corresponding to a horizontal transverse momentum kick of $p_t = .3$ Gev/c. On either side of the magnet were 1-foot thick steel slabs which shielded the rest of the apparatus from fringe fields. The dimensions of the aperture and shielding are listed in Table 2-2.

A calibration of the magnetic field was performed in the initial stages of the construction of the apparatus. A long flip coil was systematically swept over the entire aperture. Measurements were performed at points on a 4" x 4" grid in the X-Y plane. The results are shown as a function of X (horizontal) at various values of Y (vertical) in Figure 2-4 at a magnet current of 3.2 kamps, the value set during all data-taking runs.

Of course a full understanding of the random and systematic errors associated with the field measurement was necessary in interpreting the results of off-line kinematic analysis. One check was to measure the momentum of beam tracks and compare the result with the expected beam spectrum. This was also useful in calibrating the entrance hodoscope system for tagging beam momenta.

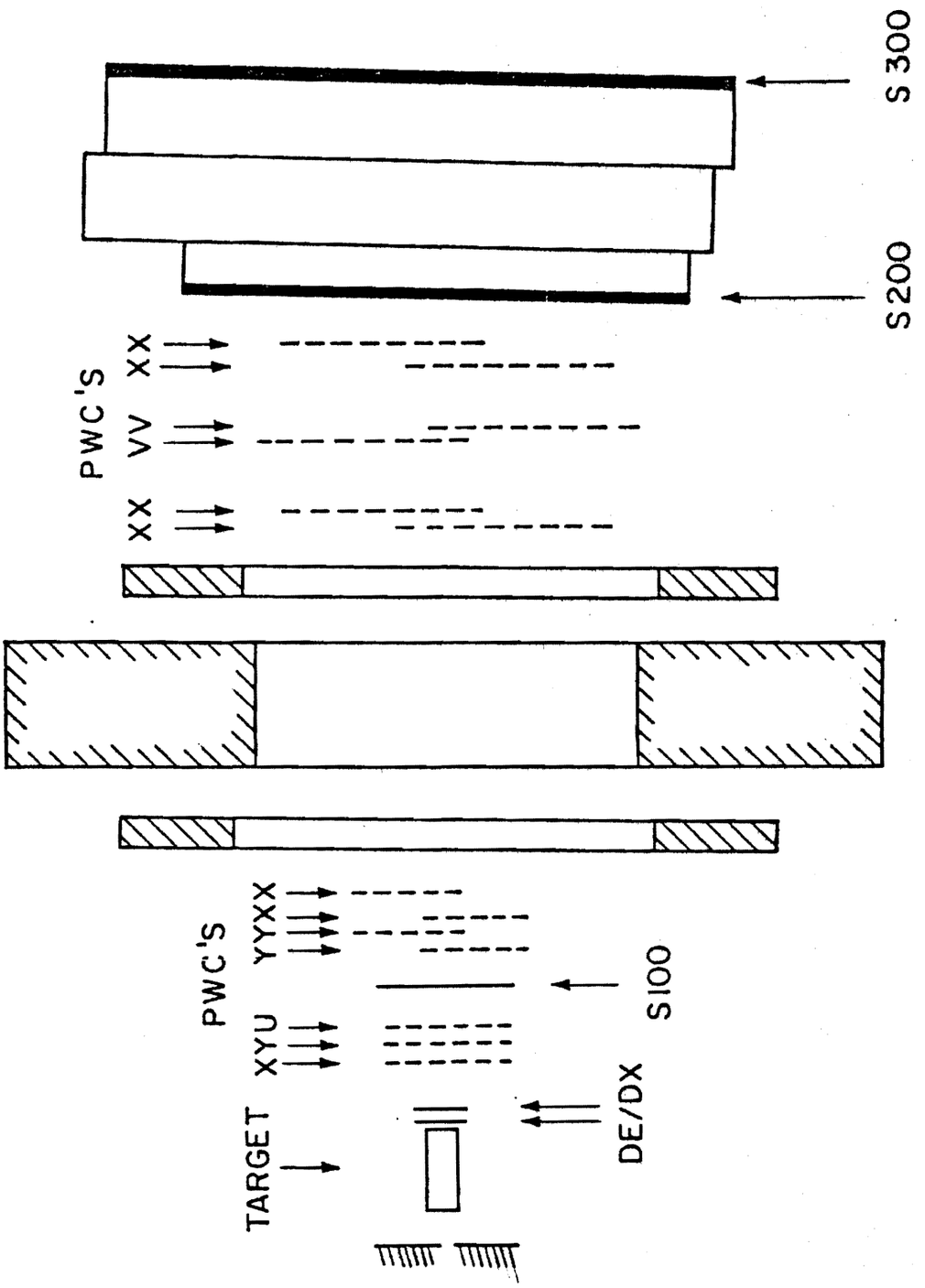

Figure 2-3. The AGS632 wide-aperture muon spectrometer

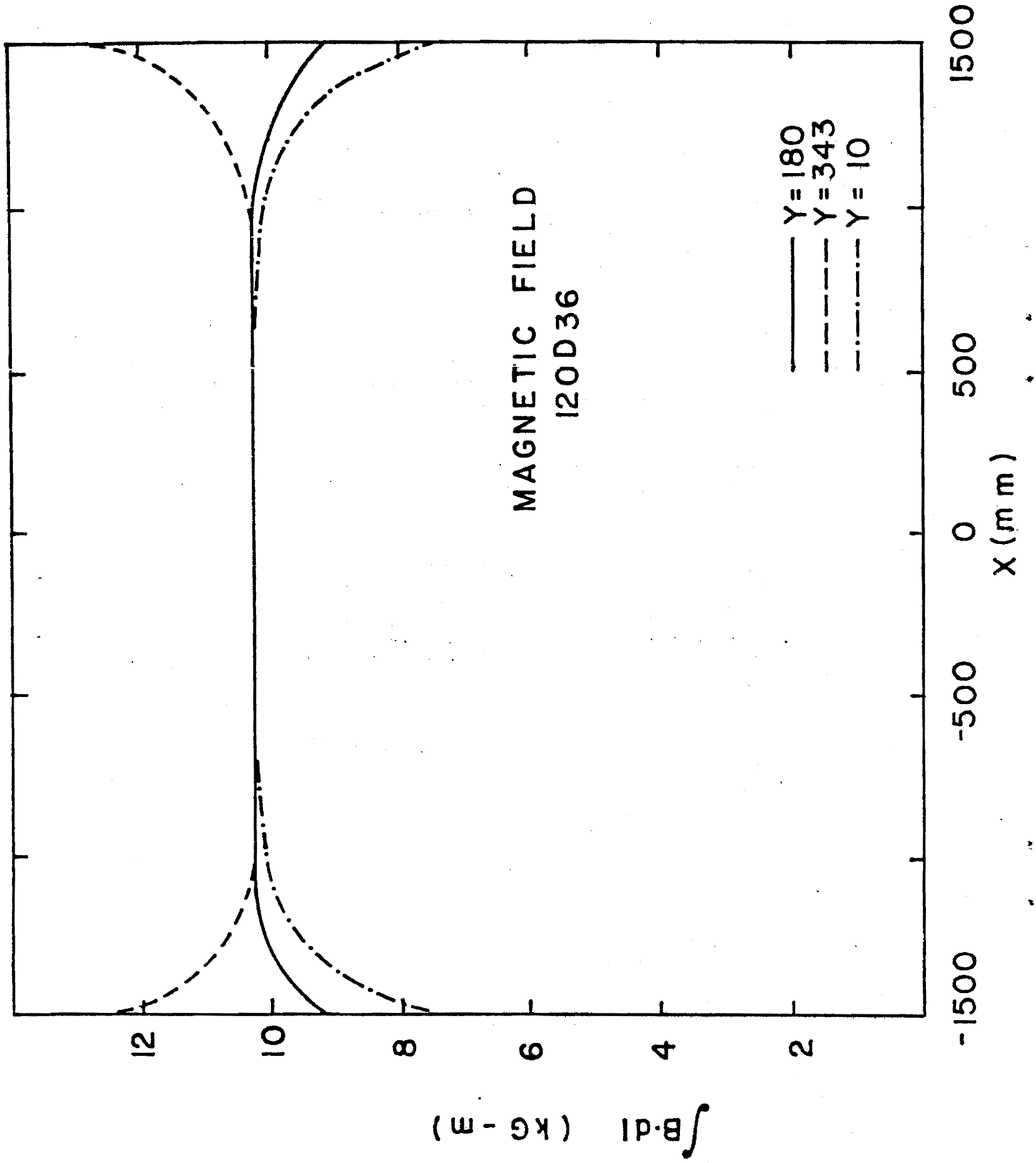

Figure 2-4. The magnetic field of Dipole 120D36 determined by the flip-coil measurement discussed in the text.

TABLE 2-2

Magnet Dimensions

	Aperture Sizes (meters)		
	Width	Height	Depth
Front shield	3.07	1.35	.30
Magnet	4.88	1.35	.91
Back shield	4.59	1.35	.30

A major source of error in measuring the momentum of a track is the finite angular resolution of the chamber system. The front (upstream of magnet) and back (downstream) chambers typically had errors in the X-Z plane

$$\begin{aligned} \Delta\theta_{\text{front}} &= .8 \text{ mrad} \\ \Delta\theta_{\text{back}} &= .6 \text{ mrad} \end{aligned} \tag{2.2}$$

Taking these in quadrature, the error in the 'bend angle' through the magnet was

$$\Delta\theta_{\text{bend}} = 1.0 \text{ mrad} \tag{2.3}$$

The momentum is found through the approximate formula

$$p = \frac{p_t}{\theta_{\text{bend}}} \qquad p_t = .03 \int B \, dl \tag{2.4}$$

where .03 is a unit conversion factor for $\int B \, dl$ in kG-m. Now

$$(\Delta p)^2 = (\Delta p_t/\theta)^2 + (p_t/\theta^2 \cdot \Delta\theta)^2 \tag{2.5}$$

$$(\Delta p/p)^2 = (\Delta p_t/p_t)^2 + (\Delta\theta/\theta)^2$$

For low momentum, say p = 2 Gev/c, we expect $\Delta\theta/\theta \simeq .7\%$, while for p = 8 Gev/c $\Delta\theta/\theta = 2.7\%$. Therefore the angular resolution will dominate the error as long as the field value is correct to within 1-2%. This was found to be consistent with Monte Carlo simulation of the spectrometer when compared with real data.

While random errors in the field values were not found to be a big problem, a systematic error emerged in the analysis of the follow-up experiment to this one (pion beam configuration, reference 3). In measuring the reaction

$$\pi^- p \rightarrow J/\psi + X \qquad J/\psi \rightarrow \mu^+\mu^- \qquad (2.6)$$

the mass of the J/ψ was systematically shifted $\sim$ 2% below its known mass. The problem was ultimately resolved by using the apparatus to measure the process

$$\pi^- p \rightarrow K^o_s \Lambda \qquad K^o_s \rightarrow \pi^+\pi^- \qquad (2.7)$$

and finding what, if any, corrections to the field measurement were necessary to get the well known K^o_s mass. This is described in reference 4, where a systematic error of -2%

was found in $\int Bdl$. This correction was applied to all analysis described hereafter.

2C. CHAMBERS

Particle tracking for this experiment was performed with a set of 13 Multi-wire proportional chambers (MWPC). This type of detector was developed in the late 1960's and its principles of operation have been described extensively elsewhere[5]. Essentially, an MWPC consists of an anode plane of closely spaced parallel wires usually held at ground, with two cathode planes (one on each side) usually held at high voltage. This configuration creates an electric field which directs negative charges towards the anodes (and positive charges away) as shown in Figure 2-5. The assembly is enclosed in a gas-filled chamber. When a charged particle passes through, it ionizes the gas. The electrons released drift toward the nearest anode wire, releasing more electrons on the way. When the heavier (hence slower) positive ions drift away from the anode, they induce a pulse that is read by the experiment's electronics.

A detailed description of the construction and performance of the chamber system is given in reference 4. However, for completeness, the major features will be reviewed here. Chambers 4-13 were constructed at the University of Rochester Cyclotron Lab on a winding machine. Wires were strung on rectangular aluminum tube frames. The cor-

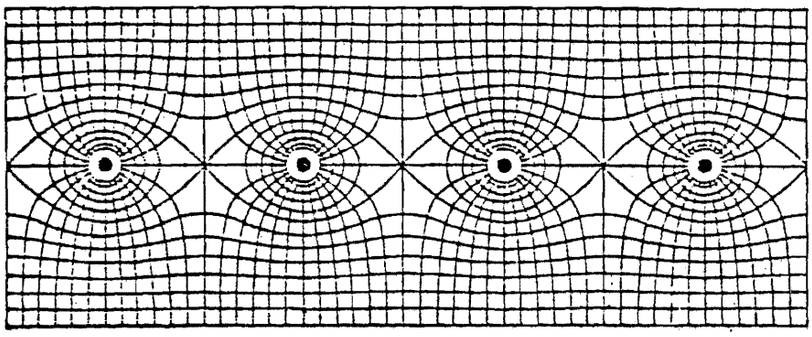

Figure 2-5. The equipotential lines of the electric field near the anode wires of a typical Multi-wire Proportional Chamber.

rect wire spacing was achieved with a lead screw that was turned by a digitized motor system. As the frame turned in the machine, the screw advanced the position of the wire. As wire was fed out from a spool, the tension was kept steady by an analog feedback system which constantly adjusted the rate of rotation of the spool. After the winding was completed, the tension of the wires was set using Bristol wrenches loaded with calibrated springs. Then the wires were glued to the frame. The tension was further tested after gluing by sending ac current through each wire while in the field of a permanent magnet and finding the normal modes of wire vibration.

Each cathode wire was left free on one end. At the other end, high voltage was fed to the cathodes via copper clad G10. The wires were connected to 10 Meg-ohm resistors in groups of ten, and each resistor was soldered to the copper board. The anode wires were individually soldered to an etched board which fed signals to the readout electronics. Amplifier-discriminator cards were plugged into the board, eight anode wires to a card. The dimensions and specifications of the system of wires are given Table 2-3.

Note that careful attention to the tensions on the wires was necessary throughout the winding process. This is due to the fact that nearby wires will repel each other, causing them to vibrate, bow, or even break. Proper tensioning keeps the wires stable in their position up to a

TABLE 2-3

Rochester Chamber Dimensions

Cathode-anode spacing	4.75 mm
Anode spacing	2.00 mm
Cathode spacing	1.5 mm
Anode diameter	.8 mil
Cathode diameter	4.0 mil
Wire length (X)	.5 m
Wire length (Y)	1.0 m
Anode tension	50 grams
Cathode tension	100 grams

certain level of high voltage. For example, the 1 meter anode wires at a tension of 50 grams will remain stable for a Voltage V < 3.25 kV. This limit, however, was considered too low to guarantee the desired electric field strengths. Hence, threads were woven through the anode sense wire at one-third and two-thirds of their length. In principle, this held the wires stable up to a voltage V < 10 kV, more than adequate for proper operation. The major disadvantage of this method was that it reduced the chamber efficiency in the vicinity of the thread.

The completed chamber assembly is shown in Figure 2-6. The assembly was enclosed by 4 mil mylar windows on aluminum frames, and made airtight. A gas mixture of 3 parts Argon to 1 part Magic gas (isobutane with .5% freon) was fed to each chamber. Isobutane works well as an ionizing gas, however the ions tend to form polymers which can coat the sense wires and reduce efficiency. To prevent this, the argon was bubbled through methylal. The methylal readily transfers charge to isobutane ions, thus inhibiting polymerization. The gas mixture was adjusted during testing to maximize efficiency and minimize multiple sparks (several adjacent wires pulsing due to only one charged track).

The chamber system was installed in the configuration shown in Figure 2-3. Their positions were then surveyed (relative to the experiment's coordinate system) using standard techniques to an accuracy of one wire spacing (2

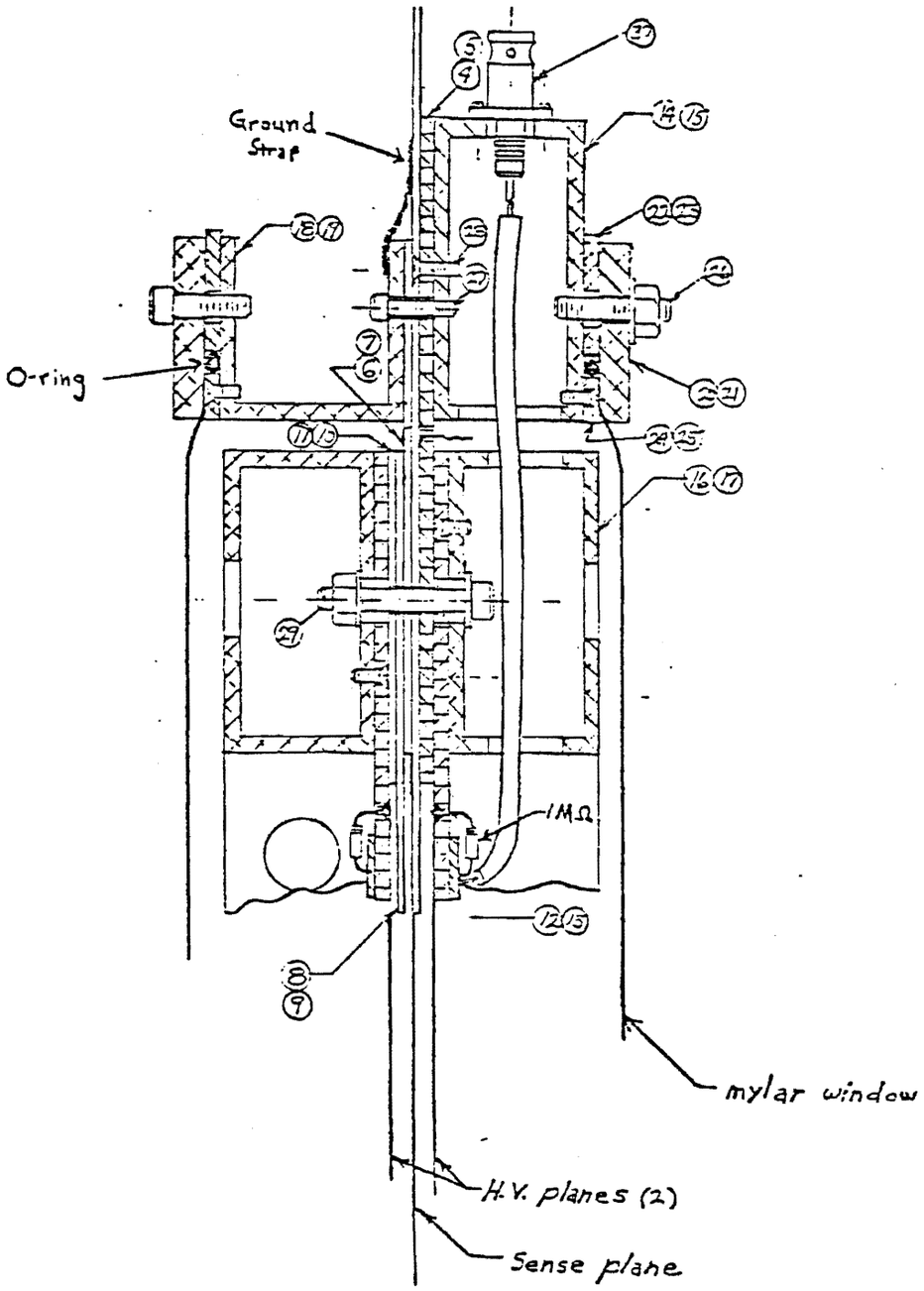

Figure 2-6. A cross section of an assembled MWPC. The materials are listed on the following page.

DET. NO.	REQ'D	FINISHED SIZE	MATERIAL
1	1	1/16 X 13 1/2 X 72	G10 DS
2	1	1/16 X 6 1/2 X 72	G10 SS.
3	2	1/16 X 6 1/2 X 40	G10 SS.
4	2	1/8 X 5 1/2 X 72	G10
5	2	1/8 X 5 1/2 X 42	G10
6	2	1/16 X 4 1/4 X 61 1/2	G10
7	2	1/16 X 4 1/4 X 51	G10
8	2	1/16 X 3 3/4 X 66 1/2	G10 SS
9	2	1/16 X 3 3/4 X 40	G10 SS
10	2	1/16 X 2 3/4 X 66 1/2	G10
11	2	1/16 X 2 3/4 X 42	G10
12	4	1/8 X 3 3/4 X 66 1/2	G10
13	4	1/8 X 3 3/4 X 40	G10
14	2	1 1/2 X 2 1/2 X 67 x 1/8 wall	Al. Tube
15	2	1 1/2 X 2 1/2 X 57 x 1/8 wall	Al. Tube
16	4	1 1/4 X 2 1/2 X 66 1/2 x 1/8 wall	Al. Tube
17	4	1 1/4 X 2 1/2 X 42 1/2 X 1/8 wall	Al. Tube
18	2	1/2 X 1/2 X 70 X 1/8	Al. U
19	2	1/2 X 1/2 X 51 X 1/8	Al. U
20	4	1/4 X 1 1/2 X 70	Al.
21	4	1/4 X 1 1/2 X 48	Al.
22	4	1/8 X 1 X 70	Al.
23	4	1/8 X 1 X 48	Al.
24	4	1/8 X 3/8 X 70	Al.
25	4	1/8 X 3/8 X 48	Al.
26	40	10-32NF X 1" Studs	Thrd. Rd.
27	40	6-32NF X 5/8 Soc. hd Cap	Scr St.
28	120	4-40-NF X 1/4 Flat hd. Scr.	Br.
29	40	10-32-N.F. X 1/4 Soc. Hd. Cap Scr	St.
30	2	UG-931/U	

List of materials for Figure 2-6.

mm.). Data was taken with the spectrometer magnet off so that all observed tracks were straight lines. Chamber positions were found by adjusting their coordinates so as to minimize the χ^2 of the straight tracks relative to the wires. The resulting coordinates are listed in Table 2-4.

The determination of the efficiency of each chamber and The associated corrections to the data will be described in section 4D.

2D. TARGET

The target consisted of twelve 1.0625" slabs of leadglass. Each slab was individually shielded from external light sources and a photomultiplier was attached to the top of each one. This configuration served the purpose of monitoring electromagnetic showers, measuring the hadronic energy deposited in the target, and aided in finding the vertex of multi-muon events. This procedure will be described below.

The composition of the leadglass and its properties are listed in Table 2-5. By weight, it was 56.6% lead (Z=82) with the largest percentages being oxygen (Z=8, 23.6%) and silicon (Z=14, 16.4%). For coherent muonic processes on nuclei at low q^2 , the cross section is proportional to Z^2 moderated by the nuclear form factor. Hence, for studying a coherent reaction such as muon tridents the contribution to the rate from materials other than lead in the target is

TABLE 2-4

MWPC Positions

X Chambers

MWPC	Wires	Spacing	X Range	Height	Z
1	256	3.175	-398.6 to 414.2	812.0	551.1
4	256	3.175	-651.9 to 160.9	812.0	1428.7
7	256	3.175	-152.3 to 660.5	812.0	1844.0
8	736	2.000	-966.9 to 505.1	1000.0	4574.5
9	736	2.000	-372.5 to 1099.5	1000.0	4749.8
12	736	2.000	-1115.0 to 357.0	1020.0	5704.3
13	736	2.000	-202.8 to 1269.2	1040.0	5877.6

Y Chambers

MWPC	Wires	SPACING	Y Range	Width	Z
2	128	3.175	-205.4 to 201.0	812.0	681.9
5	192	3.175	-306.2 to 303.4	812.0	1530.3
6	192	3.175	-310.4 to 299.2	812.0	1649.7

Tilted Y Chambers

MWPC	Wires	Spacing	Y(X=0)	Angle	Width	Z
3	256	3.175	-406.0	14.0°	812.0	769.6
10	512	2.000	-850.0	-10.3°	1000.0	5126.5
11	512	2.000	-850.0	+10.3°	1000.0	5302.5

All coordinates are given in millimeters. The origin of the coordinates is located 210 millimeters downstream of the target.

TABLE 2-5

Leadglass Target Specifications

Material	Composition (% by weight)
PbO	61
SiO_2	35
K_2O	2
Na_2O	1

Physical Properties

Radiation length	2.17 cm
Refractive index	1.72
Specific gravity	4.47
Slab thickness	1 1-16 in

negligible ($\sim$.4% for oxygen, $\sim$ .8% for silicon). However in investigating incoherent processes such as muon induced deep inelastic hadron production or inelastic virtual photon Compton scattering, it is necessary to account for the entire target composition.

The response of the target photomultipliers were calibrated with single 'straight-through' beam tracks. Pulse heights were digitized with ADC's with up to 256 counts. A typical pulse height ADC distribution is shown in Figure 2-7. The ADC distributions were assumed to be Poisson with a lower pedestal. The pulse height behavior was seen to vary for each tube for different data-taking runs, primarily due to adjustments in the photomultiplier high voltage. Hence, independent calibrations were performed for five groups of runs.

Calibration to one mimimum ionizing particle yielded for each tube a value of the pedestal N_o, a mean count $\bar{N}$ and a spread σ. Thus, for a particular event, the number of minimum ionizing particles N_{OBS} in a given slab with ADC count N_{ADC} was taken to be

$$N_{OBS} = \frac{N_{ADC} - N_0}{\bar{N} - N_o} \tag{2.8}$$

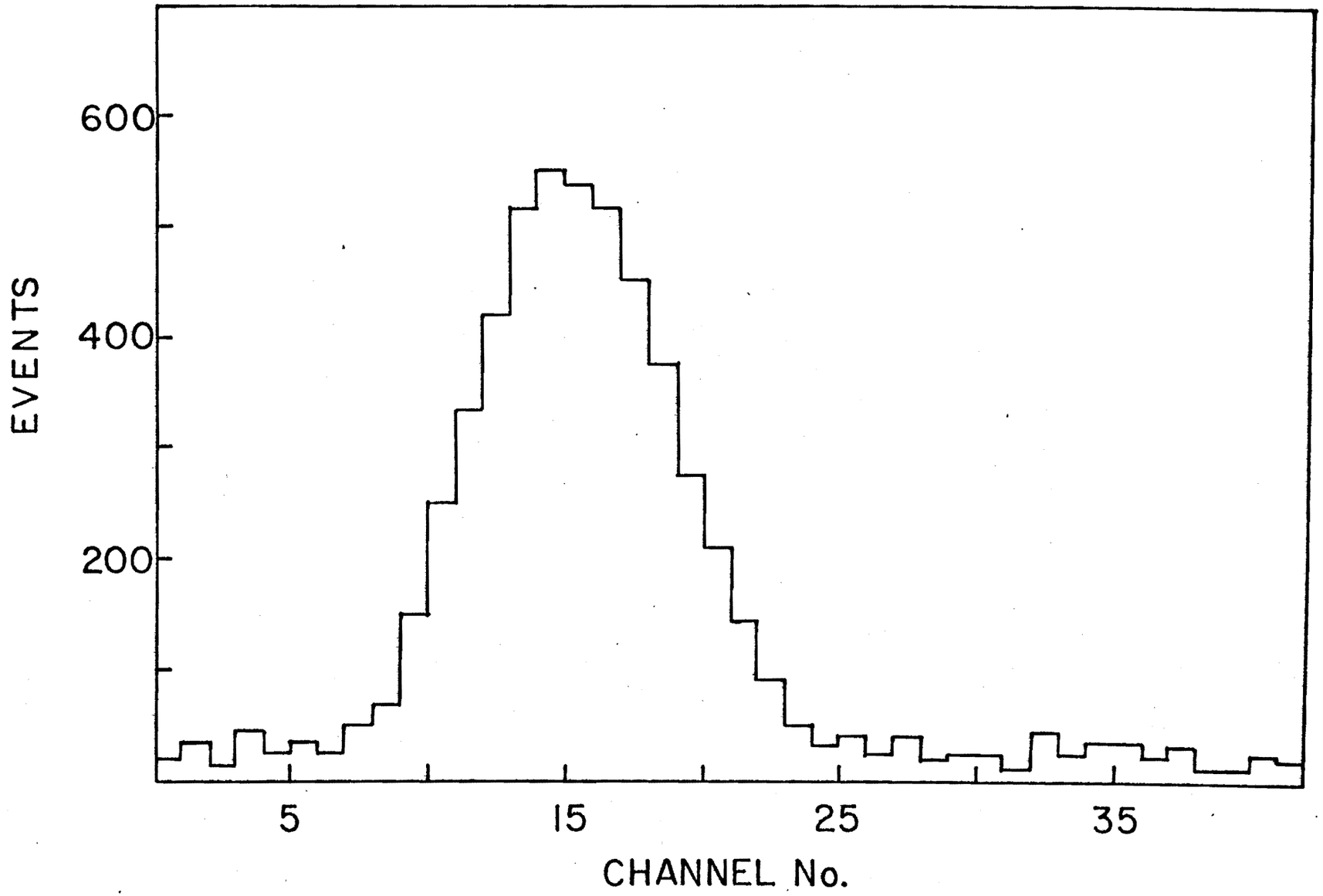

Figure 2-7. ADC distribution from the leadglass photomultipliers corresponding to one minimum ionizing particle.

with an error (assuming Poisson statistics for the number of collected photons)

$$\sigma_{OBS}(N) = \frac{\sigma}{[(N_{ADC} - N_o)\ (\bar{N} - N_o)]^{1/2}} \qquad (2.9)$$

For each event, the 12 values for the number of particles in the 12 slabs was fit to a step function. By taking the lower value of the step to be 1 and letting the higher value float, it was often possible to identify the number of charged particles in the final state and the position of the interaction vertex. The pulse heights and step function fit to a bona-fide trimuon event is shown in Figure 2-8. While this method can, in theory, determine the vertex position to within one-half a slab width ($\simeq$ .5", a significant improvement over the $\simeq$ 4" expected from multiple scattering smearing of the vertex position), in practice sometimes poor light collection efficiency limited the validity of this procedure to no more than 70% of the events. Since the statistics of the trimuon sample were so low, the pulse height information was used for diagnostic purposes but not applied in the final analysis.

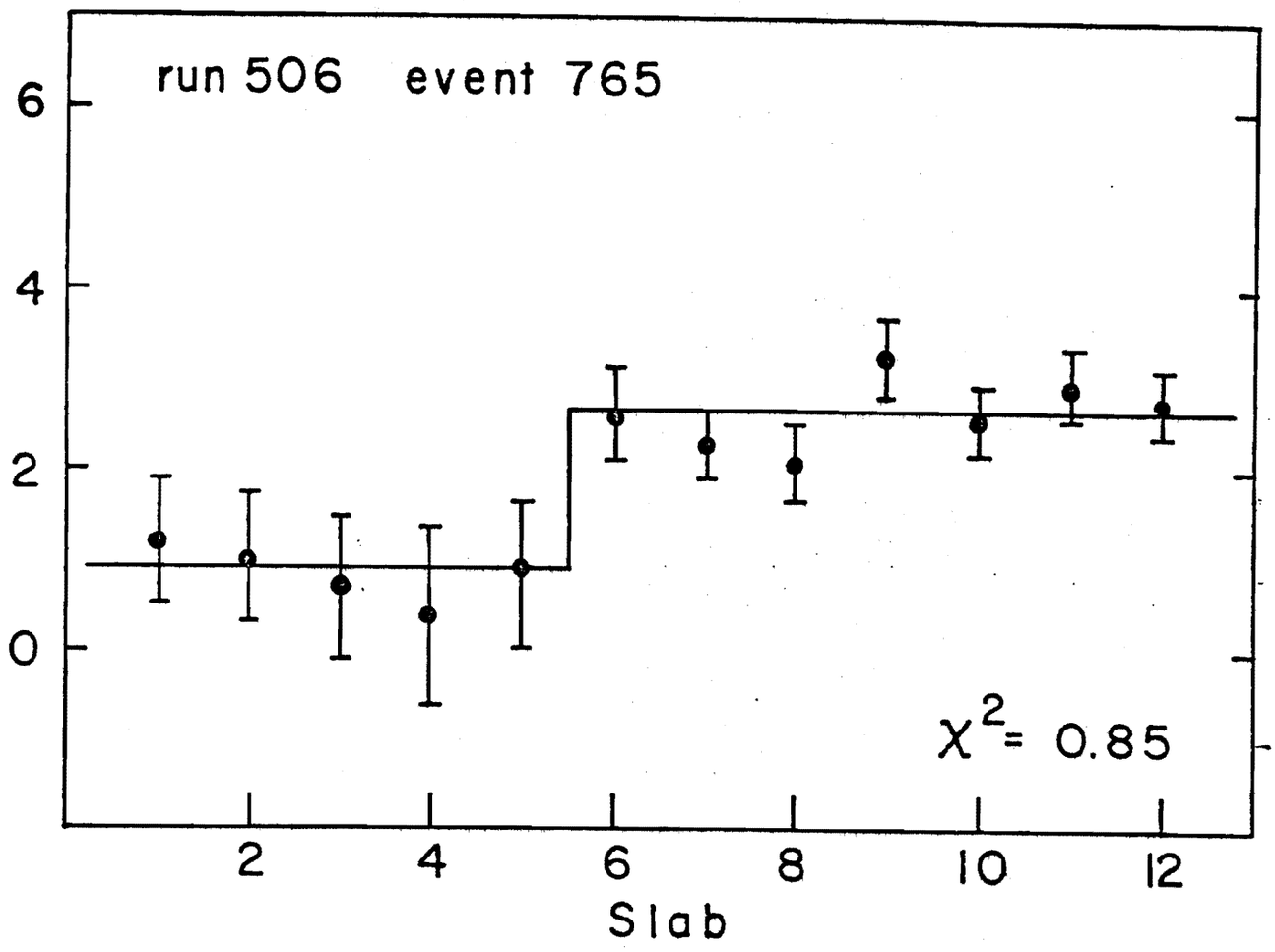

Figure 2-8. The best fit of a step function to the number of minimum ionizing particlesin each slab of the leadglass target. The points are derived from the ADC counts of the target photomultipliers. In this event the incident muon interacts in slab 5 or 6 yielding a final state containing 3 charged particles.

2E. HODOSCOPES AND MUON IDENTIFICATION

The spectrometer relied on three main hodoscopes (banks of scintillation counters) for triggering and muon identification. Their parameters are listed in Table 2-6. The first bank, referred to as the S100 plane consisted of 11 counters. Its position can be seen in Figure 2-3. While these counters were always included as part of the trigger (see following section), their position sandwiched between chambers 1-3 (XYU) and 4-7 (XYYX) provided a valuable tool for off-line track reconstruction. Electromagnetic showers and beam muons caused many sparks unrelated to the event in question to appear in the 7 upstream chambers. The target together with an S100 counter provided a 'road' in which to search for aligned sparks, greatly enhancing the efficiency of the reconstruction program (see section 4A).

Muon identification was provided by the 13 S200 counters and 10 S300 counters mounted front and back of the 5-foot iron muon filter. The iron represents 8.5 pion absorption lengths, while any muon with energy $E > 1.8$ Gev was able to penetrate the entire 5 feet. A 'muon' was defined as an S200 and an S300 counter firing in coincidence. Only pairs of counters which defined a direction that extrapolated into the magnet aperture were allowed. These combinations are listed in Table 2-7. The restriction on counter combinations helped eliminate accidental triggers due to muons from the beam halo coming down the sides of the

TABLE 2-6

Hodoscope Dimensions (inches)

Counter	Width	Height	Thickness
S101, 111	6.5	18.1	.25
S102, 103, 109, 110	4.5	18.1	.25
S104, 105, 106, 107, 108	2.5	18.1	.25
S201, 202, 212, 213	18.3	48.0	.60
S203-211	10.3	48.0	.60
S301-310	18.3	54.0	.60

TABLE 2-7

Muon Combinations for Trigger

Combination	S300	S200's
μ_1	1	1,2
μ_2	2	2,3,4
μ_3	3	3,4,5
μ_4	4	4,5,6
μ_5	5	6,7,8
μ_6	6	7,8,9,10
μ_7	7	9,10,11
μ_8	8	10,11,12
μ_9	9	11,12,13
μ_{10}	10	12,13

apparatus. In addition, the counters form a road for reconstruction.

The S300 counters were each 18 inches wide. This dimension was chosen on the basis of the amount of multiple scattering muons undergo in the iron filter. For example, a 3 Gev muon incident perpendicular on the filter will undergo a 7.5 cm ($\sim$ 3") RMS transverse displacement. Hence, a muon can at worst fire the counter adjacent to the one expected from extrapolation of the reconstructed track. No serious problem occurs for the case of single-muon detection, which after all was the primary concern of the experiment when it was designed. However, the width of the S300 elements makes for ambiguity in muon identification of multi-muon final states, particularly muon tridents. This is related to the fact that the acceptance is best for energy-symmetric trimuons (all 3 particles need $\sim$ 2 Gev to penetrate the iron leaving little of the available 10.5 Gev of energy to be shared among them). Therefore, the probability of two like-charge muons being deflected in the magnet toward the same S300 counter is fairly high. If that happens, it is impossible to absolutely identify both particles as muons. Narrower counters would have enhanced the statistics of the trident data sample. The extent of this problem is discussed in more detaiil in section 4D.

In addition to these three hodoscopes, 2 1-inch thick DE/DX counters were placed 6.4 cm and 17.9 cm downstream of the target. These were for triggering on multi-muon events, and the trigger could be set above some threshold (e.g. at least 2 minimum ionizing charged particles traversing the counters).

2F. TRIGGERS

Data taken with the leadglass target used 4 different triggers simultaneously (referred to as TS^o, TS^1, TS^2, and TS^3) each suiting a specific purpose. They are defined in Table 2-8. All triggers shared the requirement of a valid beam muon (see section 2A). A spacer circuit suppressed the trigger when 2 beam muons arrived within 20 nsec of each other.

The TS^o trigger was designed to record non-interacting beam particles or 'straight-throughs'. This monitored the beam energy spectrum from run to run. More importantly, beam tracks, due to their small angular deflection in the magnet, went through the overlap region of the rear 6 chambers, hence they intersected all 13 chambers. When this occurs, one chamber or more can misfire and the track is still reconstructable. The efficiency of each chamber could thus be obtained on a run by run basis. While this efficiency of course only applies to a partial piece of each chamber, the approximation that the efficiencies were uni-

TABLE 2-8

Trigger Definitions

$BEAM = A \cdot B \cdot C \cdot (\sum H_i) \cdot \overline{V}$

$TS0 = BEAM \cdot S100 \cdot \mu_5$

$TS1 = BEAM \cdot S100 \cdot 1\mu \cdot \overline{K} \qquad \mu = 1,2,3,7,8,9,10$

$TS2 = BEAM \cdot S100 \cdot 2\mu \qquad \mu = 1,2,3,7,8,9,10$

$TS3 = BEAM \cdot S100 \cdot 2\mu \cdot DE/DX$

form across the entire chamber was used in the final analysis (see section 4D). Finally, it was the TS^{o} triggered data that was used to calibrate the target photomultipliers as described in section 2D.

The TS^{1} trigger was designed to accept the single muon final state of deep inelastic scattering in a desired region of Q^{2} and ν. By restricting the rear muon combinations (see Table 2-7), the kinematics of the event could be similarly restricted. Further details on the data taken with this may be found in reference 6.

The TS^{2} and TS^{3} triggers were designed to detect multi-muon final states. The primary addition here is the requirement of at least two muon combinations in the rear filter. The TS^{3} trigger allowed the central counters to participate, as well as requiring $>$ 2 minimum ionizing particles in the DE/DX counters. This is because all three-muon events contain at least one muon in the forward solid angle. While many spurious events containing a beam track may be collected this way, the nature of the trident kinematics necessitates it.

2G. DATA ACQUISITION

The counter system (beam counters, target photomultipliers, hodoscopes, DE/DX) signals were first discriminated and fanned into logic circuitry, ADC's, TDC's, and scalers. A set of 'visual' scalers in the electronics trailer was

used to monitor the counting rates in various combinations of counters, including the trigger combinations. Rates were recorded before, during, and after each run to assure stability in the behavior of the apparatus and fast electronics. In addition, 'blind' scalers recorded the same information on the data tape for each run.

The system was connected to the AGS cycle clock which defined a .7 second time window corresponding to the beam 'flat top'. When the beam gate was open, triggering was allowed. The electronics was interfaced via CAMAC to a Honeywell DDP-516 computer which performed the tape writing. The CAMAC TDC's started counting when the C- counter at the beam entrance fired and stopped upon receiving a pulse from their respective counters. When the trigger condition was satisfied, two CAMAC crates sent the timing and appropriate pulse height (ADC) information to crate controllers which converted each 24 bit CAMAC word into 2 16 bit words. This information was stored in a buffer while the readout from the MWPC system was performed.

Upon triggering, a pulse was sent simultaneously to each component of the MWPC readout system. The chambers read into the system via 150-foot ribbon cable. The delay in this cable ($\simeq$ 225 nsec) was sufficient time for the trigger logic to notify the readout of incoming pulses. Any information from the chambers that is in time with the trigger is 'latched on'. The readout system consisted of

modules containing 16 latch cards, each of which could receive and save pulses from 16 wires. The trigger pulse is also sent to the CAMAC crate which then starts to scan the latch cards. Each set of 16 signals are sent via a Data Multiplexer to a Buffer Memory. The 16 signals are 'OR'd' and if any of them were 'on', the address of those wires and the bit pattern of the pulses are stored in the buffer. When all the latch cards have been processed, the CAMAC crates read into the computer, which saves all the information for tape-writing between beam pulses. This system was capable of handling $\sim$ 20 triggers per pulse.

The system was also interfaced to the AGS PDP-10 On Line Data Facility (OLDF). When time was available (several experiments time-shared on the PDP-10) data was processed by an on-line program which could display histograms of counter and chamber performance on a CRT. It also displayed schematics of events showing counter hits and chamber sparks. Some sample CRT displays are shown in Figure 2-9. On-line monitoring was extremely valuable for immediately locating inefficiencies or faults in the apparatus.

Details of the CAMAC system and readout electronics may Be found in reference 5.

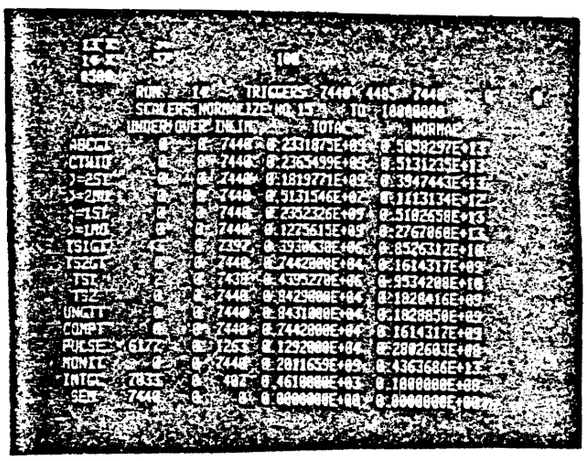

(a)

(b)

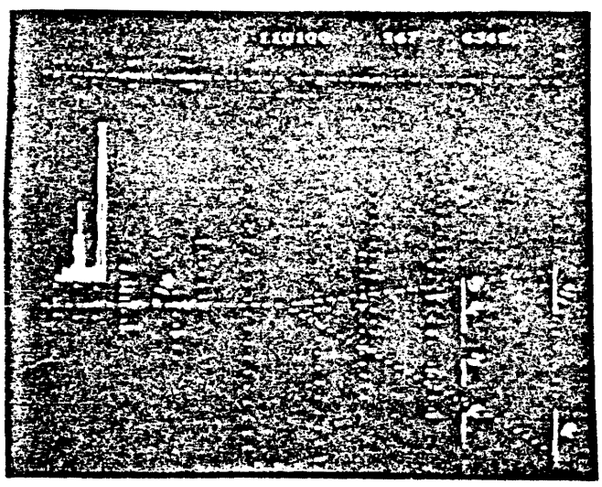

(c)

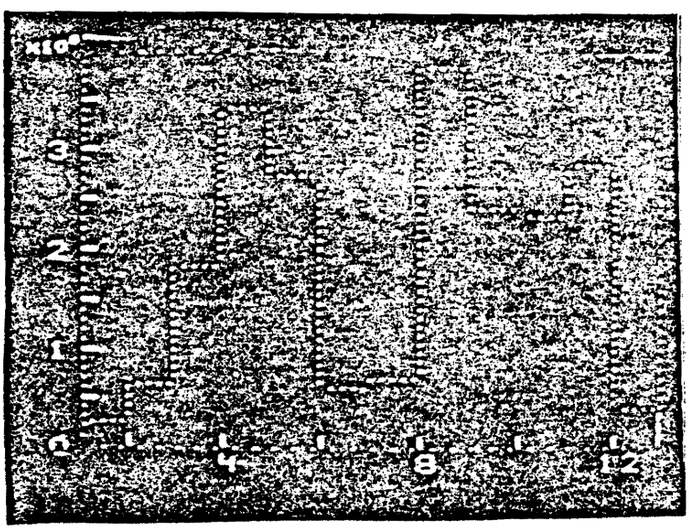

(d)

Figure 2-9. Examples of on-line data displays. (a) scalar summary (b) an MWPC profile (c) schematic of an event (d) S200 hodoscope profile.

REFERENCES

1. A. Entenberg et al., Phys. Rev. Letts. 32, 486 (1974)

2. H. Brown, private communication

3. J. Alspector et al., Phys. Letts. 81B, 397 (1979)

4. D. McCal, University of Rochester thesis, 1979 (unpublished)

5. G. Charpak et al., Nucl. Instr. Meth. 62, 235 (1968); F. Sauli, Principles of Operation of Multiwire Proportional and Drift Chambers, CERN Lecture 77-09

6. M. Miller, University of Rochester thesis, 1979 (unpublished)

CHAPTER 3

MONTE CARLO AND THEORETICAL CROSS SECTIONS

3A. THE MONTE CARLO METHOD

One method of numerically integrating a complicated function is the Monte Carlo method described in Appendix I. This technique has many advantages for high energy physics software. The more useful applications are

(a) Evaluation of total cross sections over any given range of the kinematics variables.

(b) Evaluation of the differential cross section in any kinematic variable once the differential cross section in some set of variables completely specifying an individual event is known.

(c) Providing a set of weighted Monte Carlo events for use in a computer simulation of the experimental apparatus. This is a convenient way to convolute into the acceptance

calculation such effects as variations in the beam spectrum, efficiencies, or correlations between kinematics and event geometry induced by the apparatus.

(d) Predicting the number of expected events in any kinematic bin given a theoretical model of the process involved.

In general, the differential cross section for a given process is quite complex, particularly if there is a multibody final state. Analytic integration is therefore cumbersome and impractical. Integration over the entire region of final state phase space is usually not desirable for two reasons. First, it is possible that only a fraction of the phase space accounts for practically all of the cross section, hence integration over the entire region is a waste of time. Second, the apparatus may only accept a part of the phase space. Clearly both the theoretical cross section and the data are to be compared over the same region of phase space. For example, if a muon in the final state requires 2 Gev of energy to penetrate all hadron absorbers, the piece of the cross section with low energy muons in the final state is of no interest. Choosing the optimal volume of phase space for integration must be done with great care so as not to ignore a significant region, yet must be done as efficiently as possible so as not to waste computer time.

The general procedure is as follows. Select at random (uniformly in a region of phase space ΔV) a particular Monte Carlo event, specifying the four-vectors of all particles in the initial and final states. Next, assign the event a weight

$$W_i = \left[\frac{d^n \sigma}{dx_1 dx_2 \ldots\ldots dx_n} \right]_i \Delta V \qquad (3.1)$$

where x_j $(j = 1,n)$ are a set of kinematic variables sufficient to completely define the event, the expression in brackets is the differential cross section evaluated for the values of x_j for the particular event, and ΔV is the volume of phase space from which the x_j's are chosen

$$\Delta V = \int_{\substack{\text{phase} \\ \text{space}}} dx_1 dx_2 \ldots\ldots dx_n \qquad (3.2)$$

When a sufficient number of events have been accumulated, each weight is divided by N, the number of events, and summed to get the cross section.

$$\sigma = \sum \frac{W_i}{N} = \sum_i \left[\frac{d^n \sigma}{dx_1 dx_2 \ldots\ldots dx_n} \right]_i \frac{\Delta V}{N}$$

$$= \frac{1}{\rho} \sum_i \left[\frac{d^n \sigma}{dx_1 dx_2 \ldots\ldots\ldots dx_n} \right]_i \qquad (3.3)$$

$$\rho = \frac{N}{\Delta V} = \text{density of trials}$$

(The fact that this approximates the integral for sufficiently large N is shown in Appendix I).

The set of Monte Carlo events can then be used to extract the differential cross section in any variable whatsoever. One bins a particular variable and then scans all events, summing the weights of all events falling in each bin, which yields $\Delta\sigma$, the piece of the cross section contributing to the bin. Division by the bin size yields the differential cross section at that point.

$$\frac{d\sigma}{dx_i} = \frac{1}{\rho \Delta x_i} \sum_{\substack{i^{th} \\ bin}} \frac{d^n\sigma}{dx_1 dx_2 \ldots\ldots\ldots dx_n} \qquad (3.4)$$

For evaluating a pure theoretical cross section, the phase space boundaries can be defined in a simple way (e. g. $E > 2$ Gev). However, the many varied effects of an apparatus can put complicated restrictions on the boundaries of the phase space that can be detected. Hence one must use the apparatus to define the phase space. This is done by the standard technique of tracing the Monte Carlo events through a computer simulation of the experiment. By keeping track of the weights of the events traced ('trials') and the weights of events 'detected' in the simulation program ('successes'), one can determine the acceptance of the experiment as a function of the kinematic variables. The details of this procedure will be described in section 3D. For this purpose, it is convenient to multiply the weights

W_i by the flux and target density (target particles per cm^2) corresponding to the data since

$$\text{Number of Events} = \sigma \text{ (FLUX) (TARGET)} \tag{3.5}$$

Thus a prediction on the number of observed events is obtained, fixing the expected normalization. One can then bin the Monte Carlo data in any variable and obtain predicted distributions of events. By keeping track of the sums of the weights of both trials and successes one can calculate the acceptance in any variable.

The above procedure is applied in all Monte Carlo calculations discussed in the following sections, where its versatility will become quite evident. The fictitious events serve simply as a tool of integration, but a very powerful tool. Many complicated factors can be taken into account by simple programming techniques.

3B. TRIDENT CROSS SECTION CALCULATION

The total and differential cross sections for trident production were calculated using the Monte Carlo integration technique. QEDZIA is the program originally written by M. Tannenbaum[1] to evaluate the trident cross section using the matrix elements of Brodsky and Ting[2]. The details and performance of this code have been described in reference 1, but for completeness some of the major points will be

briefly summarized here.

While the complete formula for trident production is known, it possesses extremely complicated traces and summations over spins. Hence, any practical calculation must be performed numerically. The real difficulty is in finding the appropriate regions of available phase space in which to choose Monte Carlo events. Each matrix element contains propagators for the virtual photon coupling to the muon pair (q), the virtual photon exchanged with the nucleus (q_N), and the virtual muon (p^*) (see Figure 1-1).

$$d\sigma \sim \frac{1}{q^4} \frac{1}{q_N^4} \frac{1}{(p^{*2} + m_\mu^2)^2} \tag{3.6}$$

One can see that most of the cross section will come from kinematic regions in which the above denominators are small. Equivalently, virtually all of the cross section is contained in events produced in the forward direction with small transverse momentum ($p_t < 2m_\mu$ for each final state muon and $p_t < 2m_\mu$ for all three).

Monte Carlo events were chosen in the following way. Given an incident energy, the energies of two final state muons are chosen at random and the third energy chosen to balance energy. Directions are assigned to two muons uniformly random in the angles θ and ϕ, but in such a way that each has $p_t < 2m$. The direction of the third muon is calculated so as to balance transverse momentum, then it is

assigned a $p_t < 2m_\mu$ with respect to this direction (again uniformly in θ and ϕ). Finally, the target nucleus is given a recoil to reestablish the final transverse momentum balance.

Each Monte Carlo event is assigned two weights, one for Fermi- Dirac muons and the other for muons with no exchange. The no exchange calculation assumes the two like charge muons behave as non-identical fermions, hence the cross section is derived from the four amplitudes of Figure 1-1

$$M = M_1 + M_2 + M_3 + M_4 \text{ (normal diagrams)} \qquad (3.7)$$

$$d\sigma \sim |M|^2$$

For fermions, one must include the four exchange diagrams in which the momenta of the two like charge muons are interchanged

$$\bar{M} = \bar{M}_1 + \bar{M}_2 + \bar{M}_3 + \bar{M}_4 \text{ (exchange diagrams)} \qquad (3.8)$$

$$d\sigma \sim \frac{1}{2!} |M - \bar{M}|^2$$

$$= \frac{1}{2} (|M|^2 + |\bar{M}|^2 - M\bar{M})$$

$$= |M|^2 - \frac{1}{2} M\bar{M}$$

where $M\bar{M}$ represents the interference of normal and exchange amplitudes. Note that the addition of this interference is

the only net difference between the two calculations.

In general the effect of exchange interference is to lower the total cross section. The exchange term is actually an integral which expresses the 'overlap' of the two beamlike muon wave functions. The overlap is largest when the two muons have a small opening angle and similar momenta. This is the region of low effective mass for the pair. Hence the exchange term produces a depression in the cross section at low mass $M_{\mu\mu}$, the clearest signature of muon fermion exchange independent of the overall normalization.

The cross section program was tested by calculating differential and total cross sections for 12 and 200 Gev muons on lead and proton targets. The lead form factor was taken to be

$$F(q_n^2) = \frac{1}{(1 + 63.0\, q_N^2)} \quad q_n^2 \text{ in } \text{gev}^2 \qquad (3.9)$$

Total cross sections (first Born approximation) obtained are shown in Table 3.1. The agreement with the original calculation of Tannenbaum[1] is very good. The differential cross section $d\sigma / dE_+$ where E_+ is the energy of the non-beamlike muon is shown in Figure 3-1 for a lead target both for the fermion and no exchange cases at 12 Gev. Note that the cross section rises with incident energy and that the exchange interference shrinks the total cross section. The cross section in $M_{\mu\mu}$ (like charge pair mass) is shown in

TABLE 3-1

Theoretical Trident Cross Section

(microbarns per lead nucleus)

	This Calculation	Reference 1
12 Gev		
Pb	$.864 \pm .055$	.875
p	$(.414 \pm .021) \times 10^{-3}$	
200 Gev		
Pb	12.1 ± 2.6	
p	$(.329 \pm .073) \times 10^{-2}$	

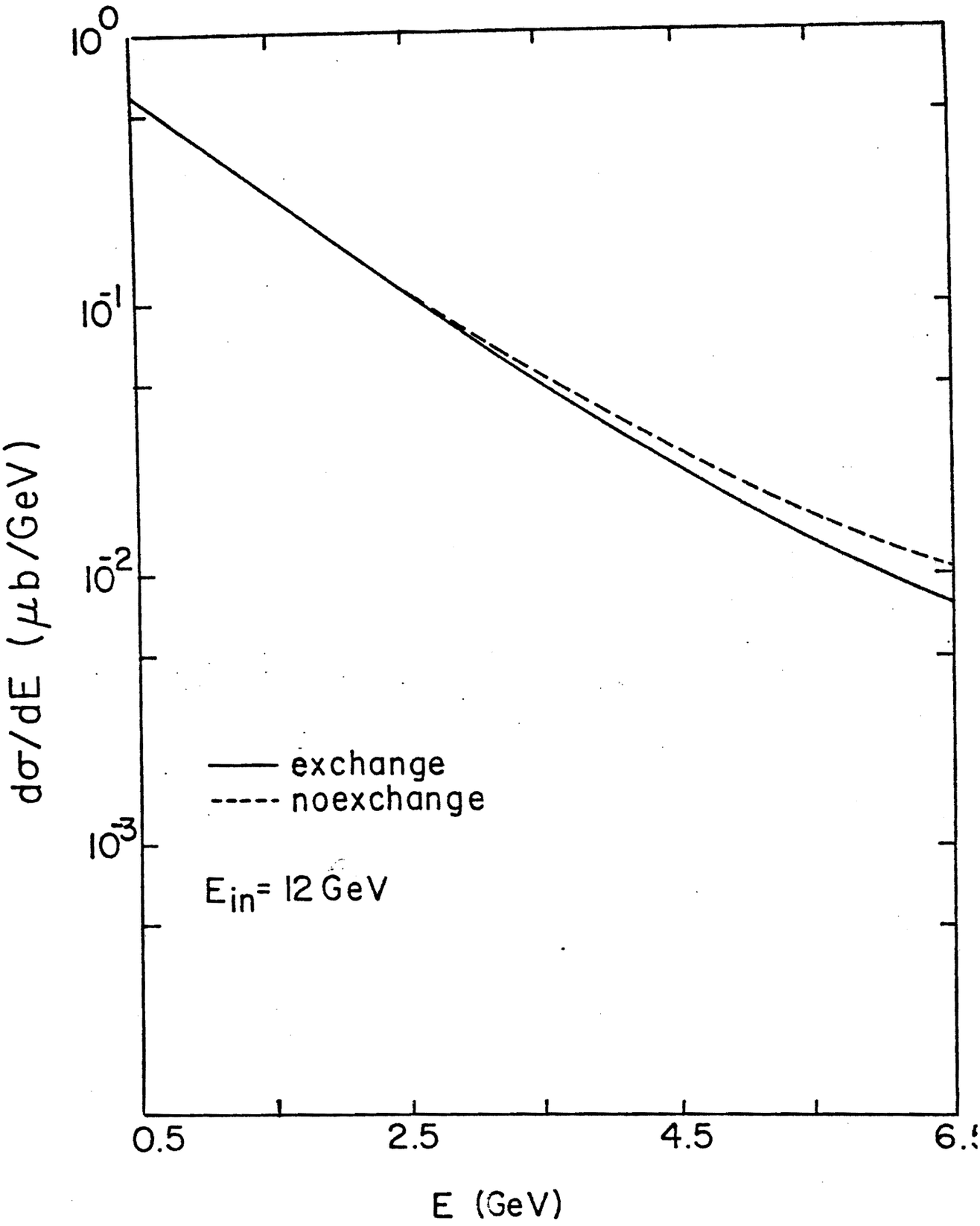

Figure 3-1. The theoretical differential cross section in the energy of the non-beamlike muon for the trident process off a lead nucleus at 12 Gev.

Figure 3-2 for a lead target at 12 and 200 Gev with exchange. Here the interference is seen to depress the cross section in one particular kinematic region. These distributions agree well with both reference 1 and an independent calculation[3] performed for high energies.

Having verified the consistency of QEDZIA, it was modified to perform the cross section calculation for this experiment. A sample of 25,000 beam tracks measured in the apparatus were fed to the program. The direction and momentum of each beam muon were defined by the entrance hodoscope system as described in section 2A. A vertex position along the z axis was chosen in a uniform random way within the leadglass target and the track was traced to that point accounting for energy loss and randomly chosen multiple scattering. The energy of the muon at that point is then fed to QEDZIA which creates a Monte Carlo event along with the two associated weights. The four-vectors of the beam and three final state muons, the weights, the vertex coordinates, and the beam energy at the target entrance were saved on tape. This procedure accounts for the variation in the beam momentum ($\pm$ 1.3 Gev c) and any correlations between the direction of the beam track and its momentum. To assure the stability of this procedure the same 25,000 beam tracks were used three times with different sets of random numbers. The total cross sections obtained in this way are summarized in Table 3-2. The variation is reasonably small, but the cross section applied to the final analysis is taken to be

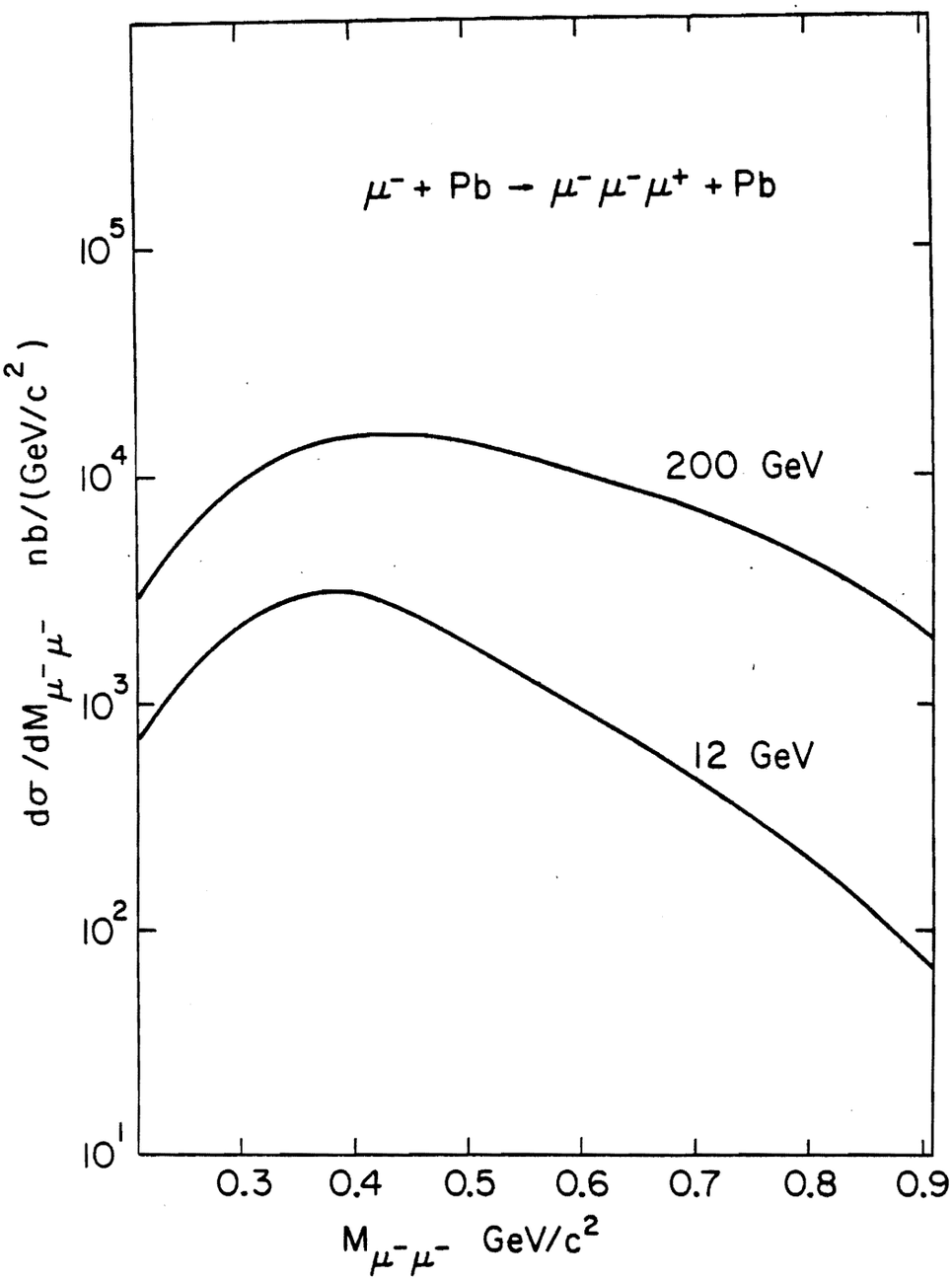

Figure 3-2. The theoretical differential cross section in the effective mass of the two like-sign muons for the trident process. The low mass suppression is due to the Pauli principle.

TABLE 3-2

σ_{total} (theoretical) tridents for the beam momentum distribution of this experiment (microbarns per nucleus, first Born approximation)

	Exchange	No Exchange
Lead		
Run 1	$.700 \pm .049$	$.778 \pm .050$
Run 2	$.660 \pm .036$	$.747 \pm .037$
Run 3	$.608 \pm .028$	$.693 \pm .029$
Average	$.656 \pm .067$	$.739 \pm .069$
Copper	$.105 \pm .005$	$.118 \pm .005$

the average of the three results.

For studies of the data taken with the brass hadron absorber following the target, it was necessary to account for muons penetrating the leadglass and interacting in the absorber. This cross section was calculated exactly as described above except that the vertex was chosen randomly within the brass. The copper form factor was taken to be

$$F(q_N^2) = \frac{1}{(1 + 32.9\, q_N^2)^2} \qquad q_N^2 \text{ in Gev}^2 \tag{3.10}$$

The total cross section for this process is also listed in Table 3-2.

Since the trident process is coherent off of a nucleus, the amplitudes are proportional to Z^2, where Z is the nuclear charge, moderated by the nuclear form factor. Hence, the Born series is in powers of $Z\alpha$ ($\sim .6$ for Pb). The first order term in the cross section is proportional to $(Z\,\alpha)^2$ while the second order (two photon) term $\sim(Z\alpha)^4$ with an interference term $\sim(Z\alpha)^3$. It is clear that for a heavy nuclear target higher order corrections can be significant. Some of the possible two photon exchange diagrams are shown in Figure 3-3. The calculation of these amplitudes for trident production has not been done due to the complexity of evaluating the large number of diagrams. Fortunately, it is possible to estimate the effect since the graphs of Figure 1-1a-b dominate the cross section ($\sim 95\%$). The photon producing the pair is at very low q^2 ($\lesssim .2$

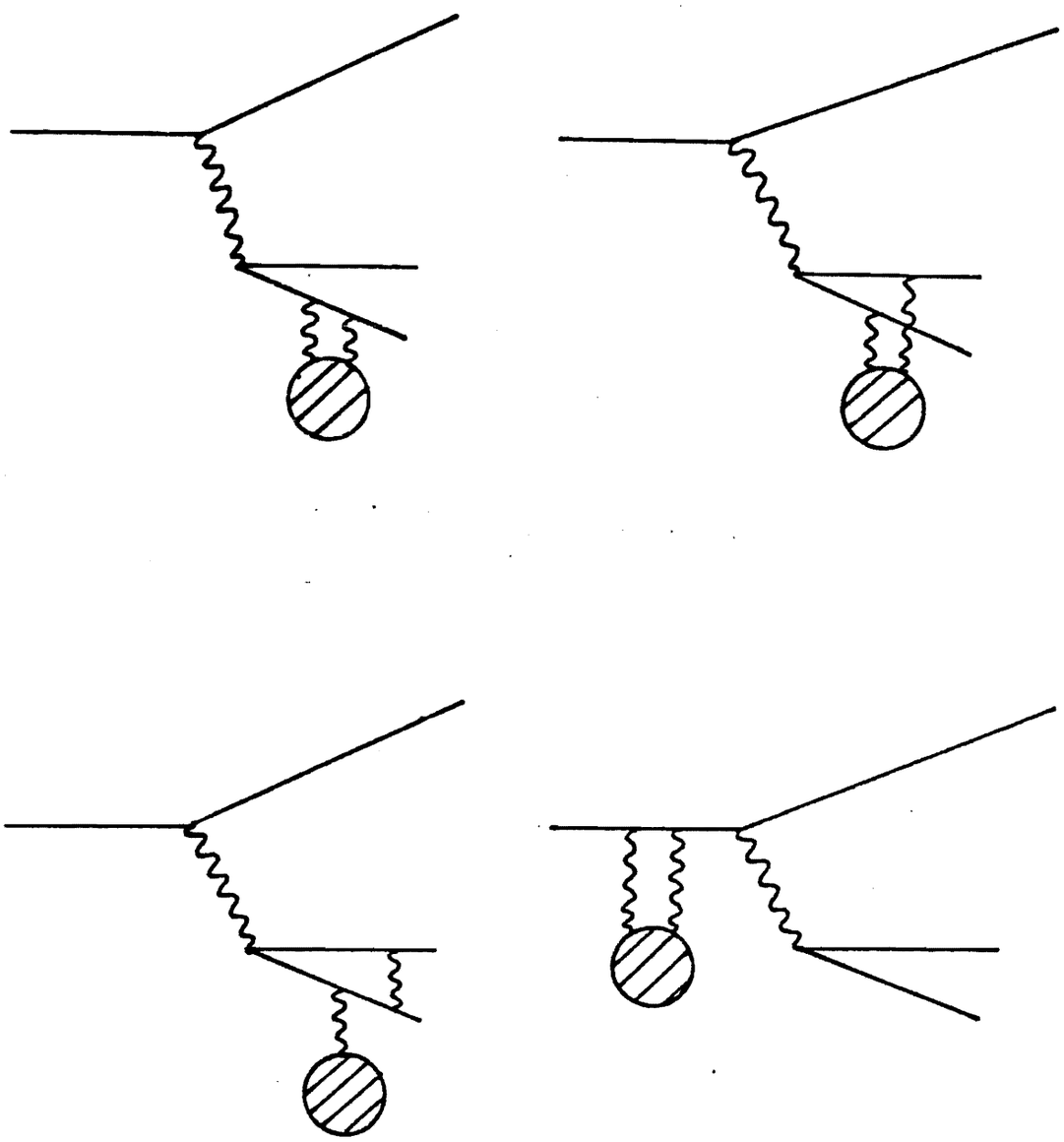

Figure 3-3. Feynman diagrams for higher order corrections to the trident process of Figure 1-1. The large number of possible diagrams makes the second order calculation extremely complex.

Gev^2), so the process is very close to the usual Bethe-Heitler pair production mechanism by real photons. The two photon exchange photoproduction cross section for muon pairs has been calculated by Bethe and Maximon[4] for scattering off a central Coulomb field and by Brodsky and Gillespie[5] for a nuclear target. The correction to the first Born term is given in reference 4 to be

$$R = \frac{\text{correction}}{\text{First Born}} = -\frac{1}{2}\,\frac{Q(Z)}{\left[\log\frac{2E_+E_-}{km_\mu} - \frac{1}{2}\right]} \qquad (3.11)$$

where $Q(Z) = .67$ for lead, k is the photon energy and E_+, E_- are the muon energies. For this experiment $R \simeq -12\%$, with very little variation ($\sim 1\%$) over the available phase space due to the slow logarithmic dependence of the denominator.

The interference of the first and second Born amplitudes is taken to be negligible. This has not been rigorously established but the expression for the interference correction in reference 5 leads us to believe it cannot exceed a few percent for this experiment. This is due to the fact that the effects of the interference are largest for wide-angle pair production.

3C. DEEP INELASTIC HADRON PRODUCTION

A significant background in the detection of muons at AGS energies is the production and muonic decay of π and K mesons. The mechanism for muon-induced hadron production is deep inelastic scattering in which the incident muon exchanges a virtual photon of four-momentum q with the target nucleon, as shown in Figure 3-4. This process has received considerable attention[6] both experimentally and theoretically since it was observed that electron (or muon) scattering from nuclei behaves as if taking place from point-like structures in the nucleon. This gave rise to the quark-parton model of the nucleon. Thus, if the nucleon really does contain pointlike charged constituents, inelastic lepton-nucleon scattering should reflect in its kinematics the elastic lepton-parton scattering. The most striking prediction of this picture is Bjorken scaling[7].

The process

$$\mu + N \rightarrow \mu + \text{hadrons} \qquad (3.12)$$

can be reduced to the subprocess of virtual photon-nucleon inelastic scattering[8], because the behavior at the muon-photon vertex is well known from quantum electrodynamics. In this experiment one measures the four-momentum of the initial and final state muons

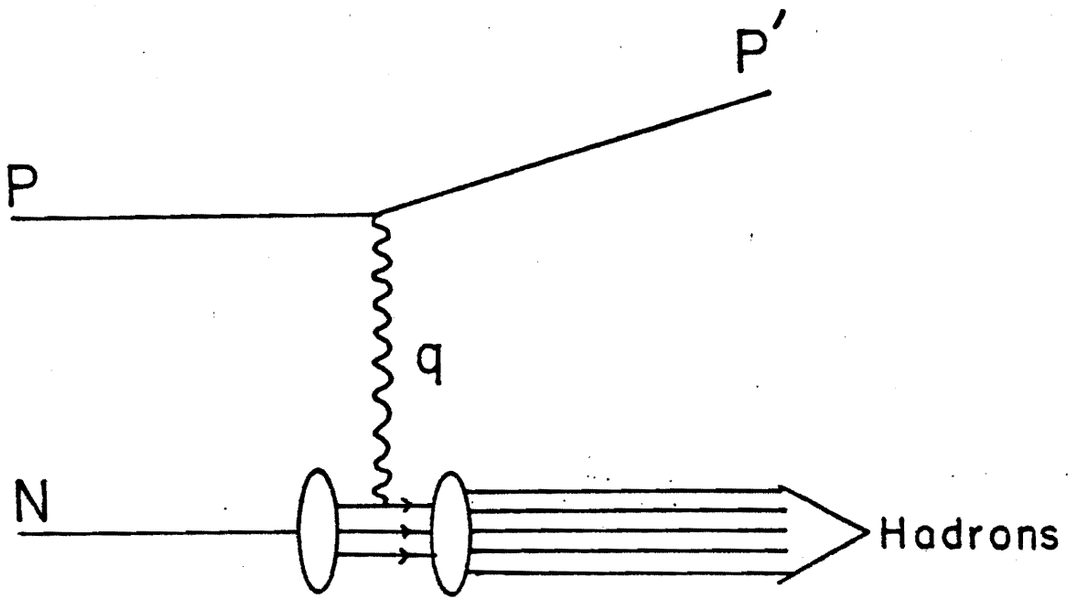

Figure 3-4. Hadron production from deep inelastic muon scattering off of a nucleon. In the parton model, this process is viewed as the exchange of a virtual photon between the muon and a charged pointlike constituent of the nucleon.

$$p = (p,E) \qquad p' = (p',E') \tag{3.13}$$

hence the four vector of the virtual photon is known

$$q = p - p'$$
$$Q^2 = -q^2 \qquad \nu = E - E' = q_0 \tag{3.14}$$

This, together with the considerations of Lorentz covariance and parity conservation leads to a general expression for the differential cross section

$$\frac{d^2\sigma}{dQ^2 d\nu} = \frac{\pi\alpha^2}{Q^4E^2}\left(2Q^2W_1(Q^2,\nu) + (4EE' - Q^2)W_2(Q^2,\nu)\right) \tag{3.15}$$

where W_1 and W_2 are called the nucleon's electromagnetic structure functions and are solely determined by the physical structure of the nucleon.

Since the photon-nucleon collision is the real process of interest, it is convenient to rewrite Equation (3.15) in terms of the photon- nucleon cross sections. We define σ_T (σ_L) as the total cross section for transversely (longitudinally) polarized photons on an unpolarized target nucleon. Then

$$\frac{d^2\sigma}{dQ^2\, d\nu} = \Gamma_T(Q^2, \nu)\ \sigma_T(Q^2, \nu) + \Gamma_L(Q^2, \nu)\ \sigma_L(Q^2, \nu) \quad (3.16)$$

where Γ_T and Γ_L are the flux of virtual photons per unit Q^2 and ν of transverse and longitudinal polarization respectively. If we define the ratio

$$\varepsilon = \Gamma_L / \Gamma_T \quad (3.17)$$

one can derive the correspondence between Equations (3.15)and (3.16) namely

$$\frac{d^2\sigma}{dQ^2\, d\nu} = \Gamma_T(Q^2, \nu)\ [\ \sigma_T(Q^2, \nu) + \varepsilon\sigma_L(Q^2, \nu)\ ] \quad (3.18)$$

where

$$\Gamma_T = \frac{\alpha}{4\pi}\frac{1}{Q^2}\frac{1}{E^2}\left(\nu - \frac{Q^2}{2M}\right)\left(\frac{2}{1-\varepsilon}\right)$$

$$\frac{1}{\varepsilon} = 1 + 2\left(\frac{Q^2+\nu^2}{Q^2}\right)\tan^2\frac{\theta}{2} \qquad (3.19)$$

$$W_1(Q^2,\nu) = \frac{\sigma_T}{4\pi^2\alpha}\left(\nu - \frac{Q^2}{2M}\right)$$

$$W_2(Q^2,\nu) = \frac{\sigma_T + \sigma_L}{4\pi^2\alpha}\,\frac{Q^2}{Q^2+\nu^2}\left(\nu - \frac{Q^2}{2M}\right)$$

M = proton mass

θ = scattering angle in the lab frame

The advantage of this formalism is that one may easily compare data from different experiments on γ_v-N cross sections by unfolding the flux factor. The γ_v-N cross section $\sigma_T + \varepsilon\sigma_L$ in a particular bin in Q^2 and ν is simply the number of events per incident muon divided by the flux factor Γ_T. The flux factor is plotted in Figure 3-5. This will be applied in the following sections.

An alternate method is the equivalent photon approximation[9] of Weiszacker and Williams[10], which gives the connection between leptoproduction and photoproduction cross sections. When a lepton scatters into a small forward angle, the virtual photon is at very low Q^2 (almost real). By making the approximation that the photon is on mass shell and ignoring its longitudinal part, it can be shown that[11]

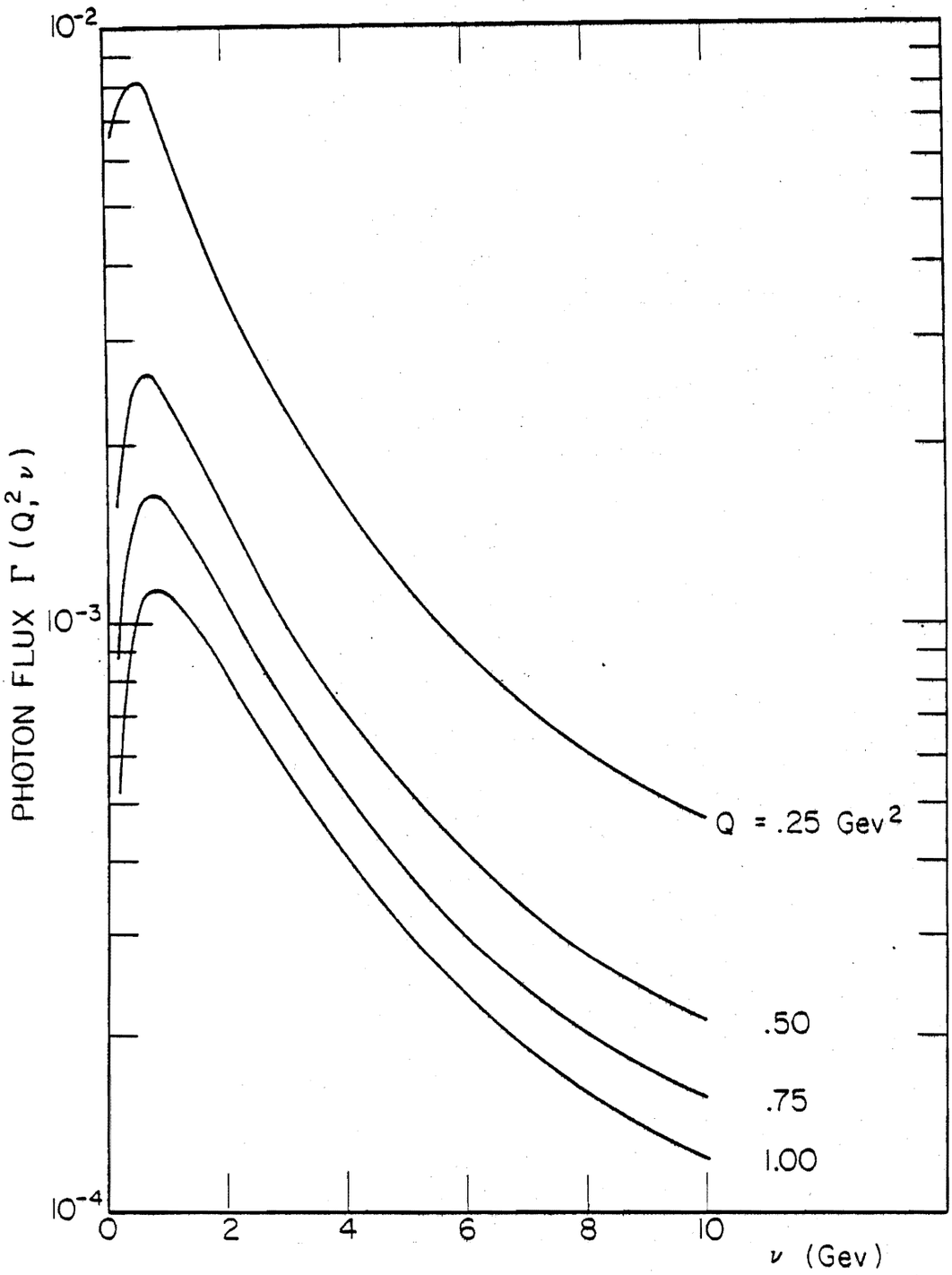

Figure 3-5. The flux of virtual photons per unit Q^2 and ν for a 10.5 Gev beam muon shown as a function of ν for several values of Q^2.

$$\sigma_{ep \to eX} = \int_0^E \frac{d\nu}{\nu} N(\nu)\, \sigma_{\gamma p \to X}(\nu) \qquad (3.20)$$

where ν is the photon energy and E the beam energy. $N(\nu)$ is a photon flux factor given by

$$N(\nu) = \frac{\alpha}{\pi} \int d(\cos\theta)\, \frac{2\nu^2 E'}{E}\, \frac{1}{Q^4} \left[\frac{1}{2} Q^2 + \frac{E^2 E'^2}{\vec{q}^2} \sin^2\theta \right] \qquad (3.21)$$

where $\nu = E - E'$. The advantage of this formalism is that one can estimate leptoproduction cross sections at low Q^2 if the corresponding photoproduction cross section is known. This form of the photon flux was also applied in weighting Monte Carlo events.

The actual distribution of hadrons produced in deep inelastic scattering has not been well measured. This is due to the experimental difficulty in observing many-particle final states. Hence, we assumed a phenomenological formula for the angle and momentum distribution of produced hadrons

$$\frac{dN}{d(\cos\theta)\, dp} = 2 \left(1 - \frac{p}{p_{max}} \right) \frac{(4.5)^2}{p_{max}}\, e^{-4.5\theta} \qquad (3.22)$$

where θ is the angle of the hadron relative to the virtual photon direction and p its momentum in the γ_v-N center of mass system. Note that this expression assumes a flat momentum distribution and a steep angular dependence characteristic of such processes. Also, as shown above, it is normalized to a mean multiplicity of 1. This can be adjusted by a constant factor.

Having established a model for producing hadrons, it was then necessary to estimate the probability that a π or K meson would decay in flight in the apparatus and be detected as part of a valid trigger. The probability of escaping the target was found by calculating an absorption length for leadglass using the total absorption cross sections measured by Denisov et al[12]. These values are given in Table 3-3. Next, one needs the probability of decay in flight between the target and muon filter. This is shown in Figure 3-6 as a function of momentum for π's and K's as calculated using special relativity and the known π and K lifetimes. Note that, while K production should be at a lower level than π production, its decay probability is larger due to the higher mass of the K.

The relative multiplicities of π^+, π^-, K^+, and K^- were taken from SLAC[13] and Cornell[14] electroproduction data. Figure 3-7 shows the π^+/π^- and K/π ratios with simple fits which were used in the Monte Carlo calculation. The mean number of π^+'s per event was taken to be .5 and all other particles were scaled from this using the ratios of

TABLE 3-3

Total Absorption Cross Sections

(mb per nucleus, 2 Gev/c < p < 10 Gev/c)

Nucleus	π^-	π^+	K^-	K^+
Pb	1910	1690	1603	1488
Si	427	378	344	320
O	280	248	223	207
K	547	485	444	412
Na	368	326	295	274

Absorption Lengths in Leadglass (cm)

π^-	30.5
π^+	34.5
K^-	37.3
K^+	40.2

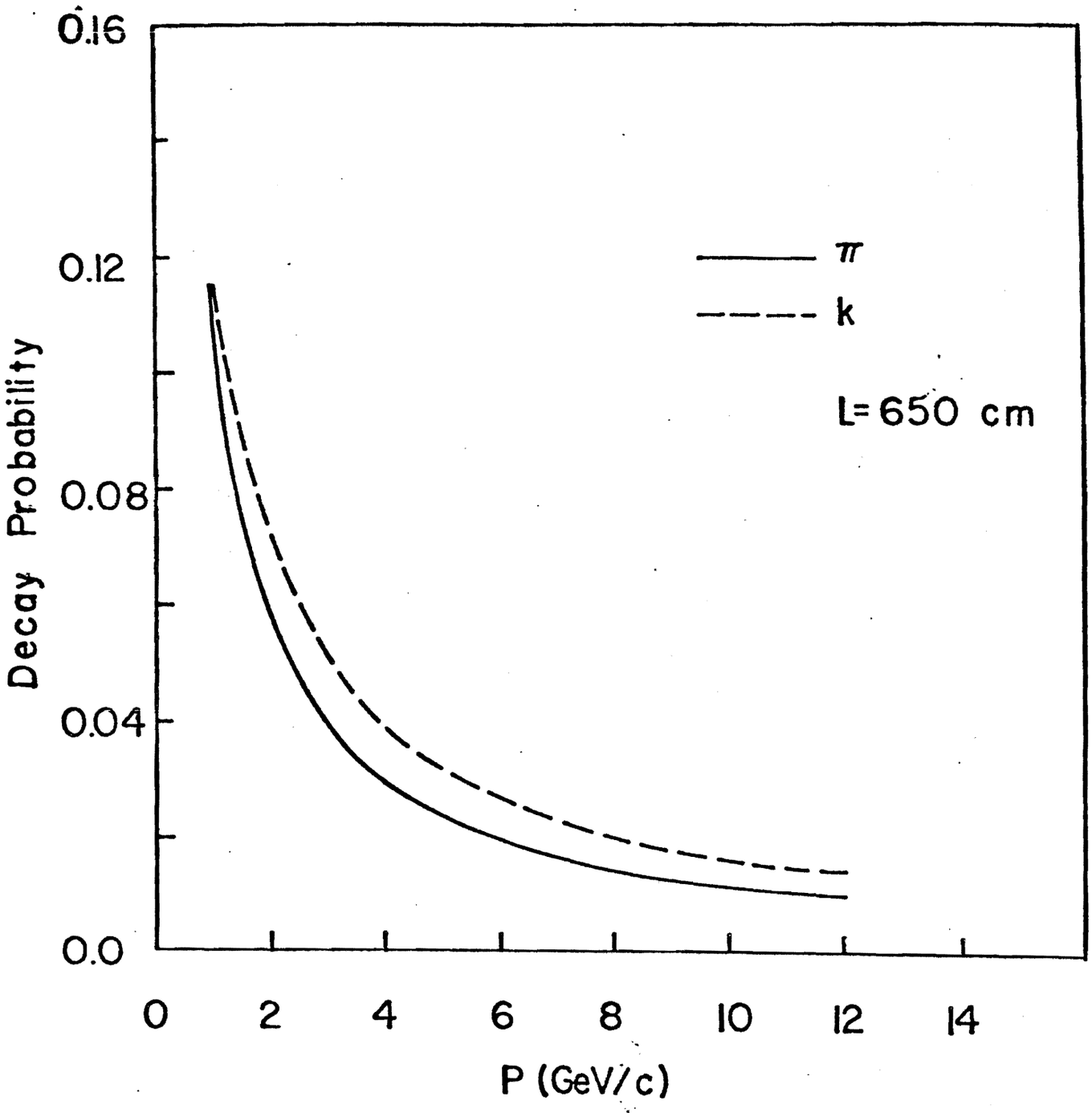

Figure 3-6. The probability of pion and kaon decay over a flight path of 650 cm. (length typical in this apparatus).

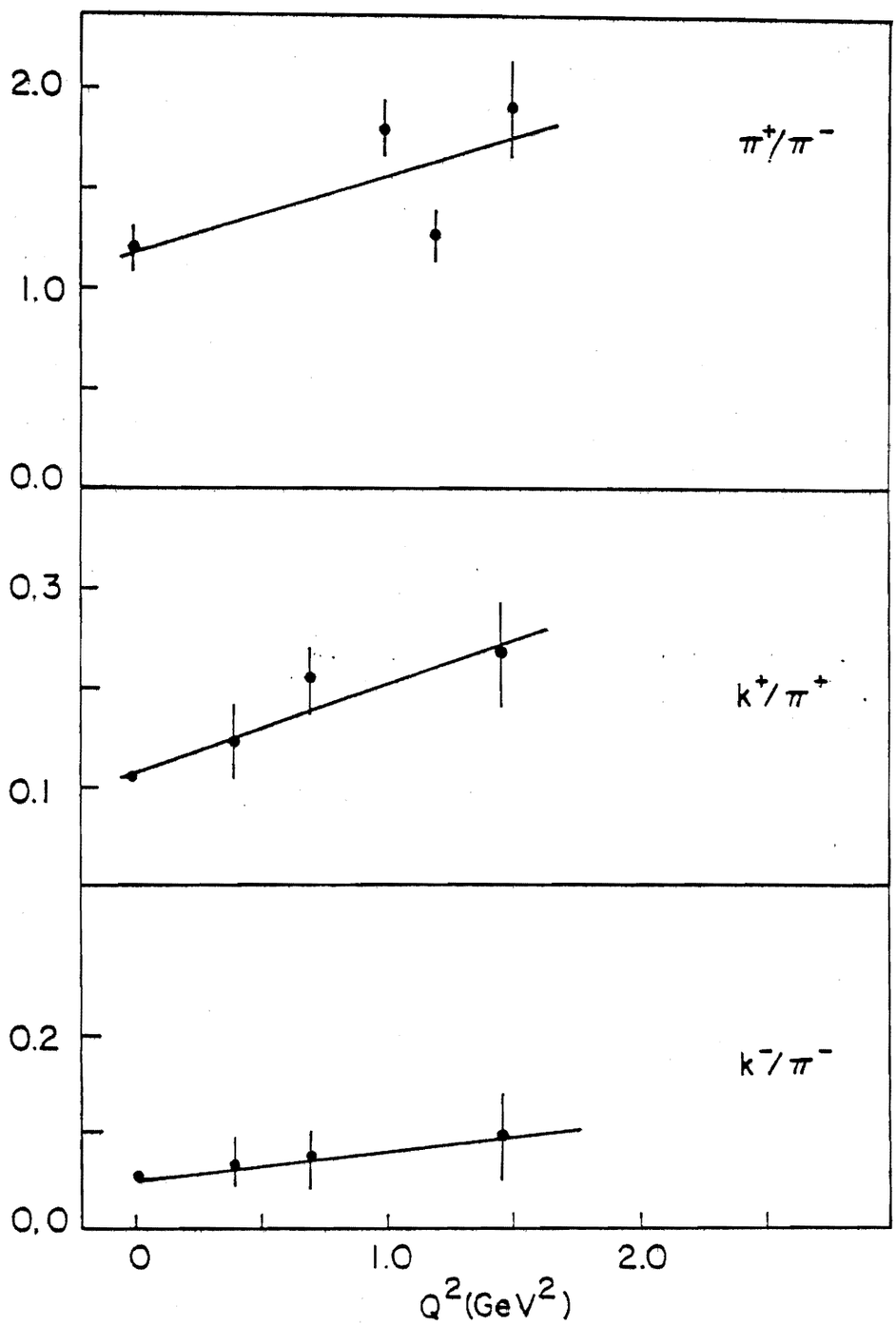

Figure 3-7. Ratios of multiplicities of pions and kaons produced in inelastic lepton-nucleon collisions. The data points are from references 13 and 14. The lines are the ratios applied in the Monte Carlo program.

Figure 3-7.

As will be seen in the following section, all Monte Carlo events for hadron production and decay allowed the hadron to escape the target and decay every time. Hence, the escape and decay probabilities had to be included in the weight for the event.

$$W_{total} = W_{\mu} W_{hadron} \text{ (escape prob) (decay prob)} \quad (3.23)$$

where W_{μ} is given by Equation 3.15 times the muon flux and target density. The form factors W_1 and W_2 were taken from fits to Fermilab muon-scattering data[15]. W_{hadron} is given by Equation 3.19 times the appropriate multiplicity factor.

3D. MONTE CARLO PROGRAM

The program CHANCE was a general purpose Monte Carlo particle tracing program written specifically for this apparatus. In its raw form, it contained routines for tracing particles through chambers, counters, air gaps, the magnetic field region, the muon filter, and ten different types of materials. In tracing through each piece of the apparatus, or 'element', each particle was multiple scattered and its energy loss calculated. Up to 15 different particles could be traced. The physics of any particular process was input through user-supplied routines which read Monte Carlo events, determined the characteristics of decays in the ap-

paratus, described the trigger, performed kinematic cuts, and wrote Monte Carlo data tapes.

A schematic of the tracing program is shown in Figure 3-8. The input was always a file created when the weighting for the particular type of event was performed. This file contained a vertex position, the four-vectors of the beam muon and final state particles (μ, π, or K), and all associated weights. For ease of theoretical calculation the final state four-vectors were always relative to a beam direction along the z axis, hence the program first performed a rotation to align the 'theoretical z axis' with the actual direction of the beam muon.

If a π or K was present, the next step was to modify the weight of the event to account for target absorption and the probability of decay. The weight was multiplied by the probability the meson would escape the target and by the probability it would decay into a muon between the target and muon filter. Since this decay probability depended weakly on the distance it traveled (it can vary only a few percent over the range of distances possible in this apparatus), the decay factor was considered only as a function of the particle momentum (see Figure 3-5). An estimate of the length of the particle's potential trajectory was made and the decay point was chosen randomly along this distance.

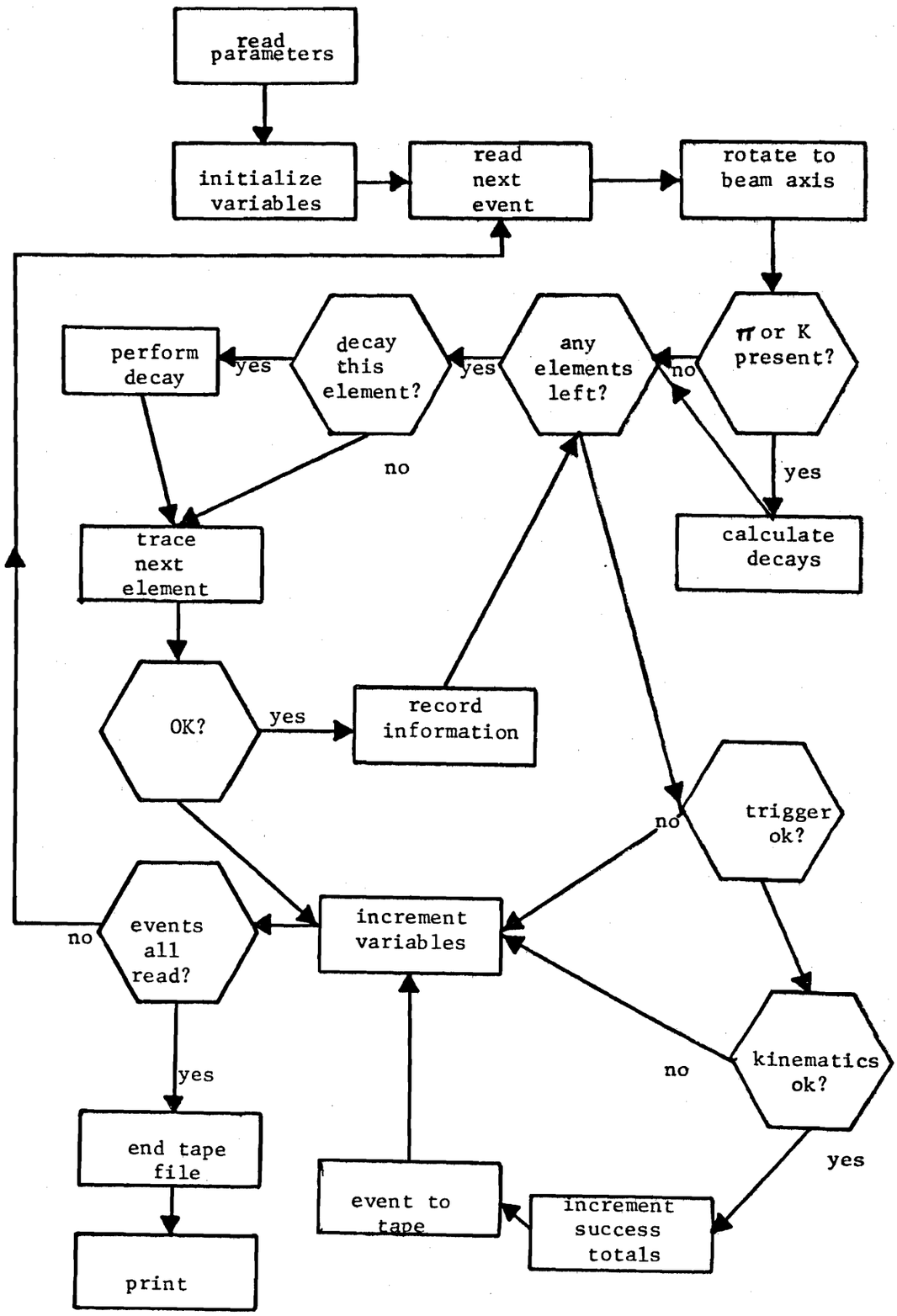

Figure 3-8. Flow diagram of Monte Carlo tracing program CHANCE.

All final state particles were then traced through successive elements of the apparatus, the energy and trajectory being modified each time. The range-energy relations given by Joseph[13] were applied. If a meson was tagged to decay in a particular element it's identity was changed to a muon at that point. Since muons from the decays $\pi \rightarrow \mu\nu$ and $K \rightarrow \mu\nu$ appear in the forward direction in the lab, the direction of the muon was taken to be the same as that of the meson. However, the muon energy was randomly chosen over the flat momentum spectrum of the two-body decay.

After each element, a check was made to see if enough particles remained to warrant continuation of the tracing. For example, if one of the muons in a trident event missed the magnet aperture, the event, having no chance of success, was tagged a failure and a new event was started. If however, enough particles did remain, appropriate information was recorded before proceeding to the next element. For example, if the element was an MWPC, the numbers of the wires nearest to the trajectories were saved.

When all elements had been traversed, the program decided if the event would have triggered the apparatus. This was done with a user-supplied routine which defined the trigger in question (i. e. TS^3 for a trident event). If the trigger failed, the event was tagged as a failure. If it was a success, however, a routine was called which interpreted the traced trajectories as they would show up on an

actual data tape. For example, the slopes of each track were 'smeared' randomly under a normal distribution in accordance with the resolution of the MWPC system. Also each track was assigned a momentum based on its trajectory and the 120D36 field map (in general the momentum so assigned could differ from the original momentum used during the tracing).

Each successful event was written on tape in precisely the same format as the compressed DST described in section 4B. This allowed the use of the same program in analyzing both real and Monte Carlo data. When all events had been traced, a summary of the tracing and the weights of successes and failures were printed. A typical summary of a Monte Carlo for π^+ production and decay (which simulates the dimuon data) is shown in Figure 3-9.

PARTICLE TRACE SUMMARY FOR PI-

ELEMENT		PASS	LEFT	RIGHT	BOTTOM	TOP	STOP	DECAY,ETC.
AIR GAP	1	0	0	0	0	0	0	0
TARGET	1	0	0	0	0	0	0	0
TARGET	2	25000	0	0	0	0	0	0
TARGET	3	25000	0	0	0	0	0	0
PIDECAY	1	23106	146	155	57	60	0	1476
CHAMBER	1	20144	59	38	0	0	0	0
CHAMBER	2	19006	278	301	0	0	0	0
CHAMBER	3	14892	337	247	0	0	0	0
COUNTER	1	13343	228	292	0	0	0	0
CHAMBER	4	6887	0	4005	0	0	0	0
CHAMBER	5	6761	3861	0	0	0	0	0
CHAMBER	6	6275	164	3944	0	0	0	0
CHAMBER	7	5500	3581	431	0	0	0	0
AIR GAP	2	5035	0	0	0	0	0	0
MAGNET	1	8327	0	0	0	0	0	0
MAGNET	2	6534	0	0	0	3	0	0
MAGNET	3	5854	124	0	156	136	0	0
CHAMBER	8	961	499	565	3	3	0	0
CHAMBER	9	813	322	184	5	5	0	0
CHAMBER	10	449	157	0	54	8	0	0
CHAMBER	11	303	1	140	49	13	0	0
CHAMBER	12	76	8	53	7	4	0	0
CHAMBER	13	0	0	0	0	0	0	0
AIR GAP	3	0	0	0	0	0	0	0
COUNTER	2	0	0	0	0	0	0	0
FILTER	1	0	0	0	0	0	0	0
FILTER	2	0	0	0	0	0	0	0
FILTER	3	0	0	0	0	0	0	0
COUNTER	3	0	0	0	0	0	0	0
TRIGGER	1	0	0	0	0	0	0	0
KINEMATIC	1	0	0	0	0	0	0	0

MULTIPLICITY OF SUCCESSES 1291 0 0 0 0 0 0

Figure 3-9. A typical particle trace summary from the Monte Carlo simulation of muon pairs resulting from the production and decay of negative pions. Note that all pions were required to decay between the target and the muon filter. The probability of such a decay was accounted for in the weighting procedure.

REFERENCES

1. M. Tannenbaum, Phys. Rev. 167, 1308 (1968)

2. S. Brodsky and S. Ting, Phys. Rev. 145, 1018 (1966)

3. CERN- European Muon Collaboration, private communication

4. H. Bethe and L. Maximon, Phys. Rev. 93, 768 (1954)

5. S. Brodsky and J. Gillespie, Phys. Rev. 173, 1011 (1968)

6. W. Loomis et al., Phys. Rev. Letts. 35, 1483 (1975)

7. J. Bjorken, Phys. Rev. 179, 1547 (1969)

8. L. Hand, Phys. Rev. 129, 1834 (1963)

9. H. Terazawa, Rev. Mod. Phys. 45, 615 (1973)

10. C. Weiszacker and E. Williams, Z. Phys. 88, 612 (1934)

11. R. Curtis, Phys. Rev. 104, 211 (1956); R. Dalitz and D. Yennie, Phys. Rev. 105, 1598 (1957)

12. S. Denisov et al., Nucl. Phys. B61, 62 (1973)

13. J. Martin et al., Phys. Letts. 65B, 483 (1976)

14. C. Bebek et al., Phys. Rev. D15, 3085 (1977); Phys. Rev. D15, 594 (1977); E. Lazarus et al., Phys. Rev. Letts. 29, 743 (1972)

15. H. Anderson et al., Phys. Rev. Letts. 38, 1450 (1977)

16. P. Joseph, Nucl. Instr. Meth. 75, 13 (1969) and references quoted therein

CHAPTER 4

DATA REDUCTION

4A. RECONSTRUCTION

A total of 202 runs were performed with the TS^3 trigger and the lead glass target. For 96 of these runs the absorber was placed downstream of the target. Each run recorded between 10K and 30K triggers. A total of 1546K TS^2 and TS^3 events were recorded with the bare target and 1988K with the aborber in place. The total accumulated flux was 2.1×10^{10} muons without the absorber and 1.15×10^{10} with it. This data was recorded on 7-track tape at 800 BPI. These tapes were translated onto 9-track tape in format compatible with the Broookhaven CDC 7600.

The first step in the off line analysis was the reconstruction of particle tracks from the raw MWPC and hodoscope data. All tracks so found were written onto Data Summary Tapes (DST), which contain for each event the chamber and counter hits, TDC and ADC counts, the geometric parameters

of all reconstructed tracks, and their momentum.

The chambers can only measure the position of a particle in one coordinate. Of course, since the chambers are mounted perpendicular to the z (beam) axis, the z coordinate is given if the chamber fires at all. In Figure 4-1 the spectrometer is shown again. The X chambers measure position along the x (horizontal) axis and Y chambers along the y (vertical) direction. Chambers designated U or V measure position along an axis rotated relative to the y axis 14^{o} and 10.5^{o} respectively. The basic idea of track reconstruction in 3 dimensions is to search for sets of wires that pulsed in a straight line in a series of X chambers, then use the tilted (U and V) chambers to connect or 'link' them with a similar set of wires in the Y chambers. The result is a line in 3-space.

Two X chambers (8,9) formed a plane directly downstream of the 120D36 magnet, followed by two tilted chambers (10,11), and finally two more X chambers (12,13). Chambers 8-9 overlapped 87.8 cm and chambers 12-13 56.0 cm. The reconstruction program first looked at the two planes of X chambers and formed all possible 'segments' connecting hits that intersected an S200 counter that had fired. The counter requirement reduces significantly the number of possible segments. The intersection of a wire in a tilted chamber with the plane formed by the two x-wires determines a unique y coordinate.

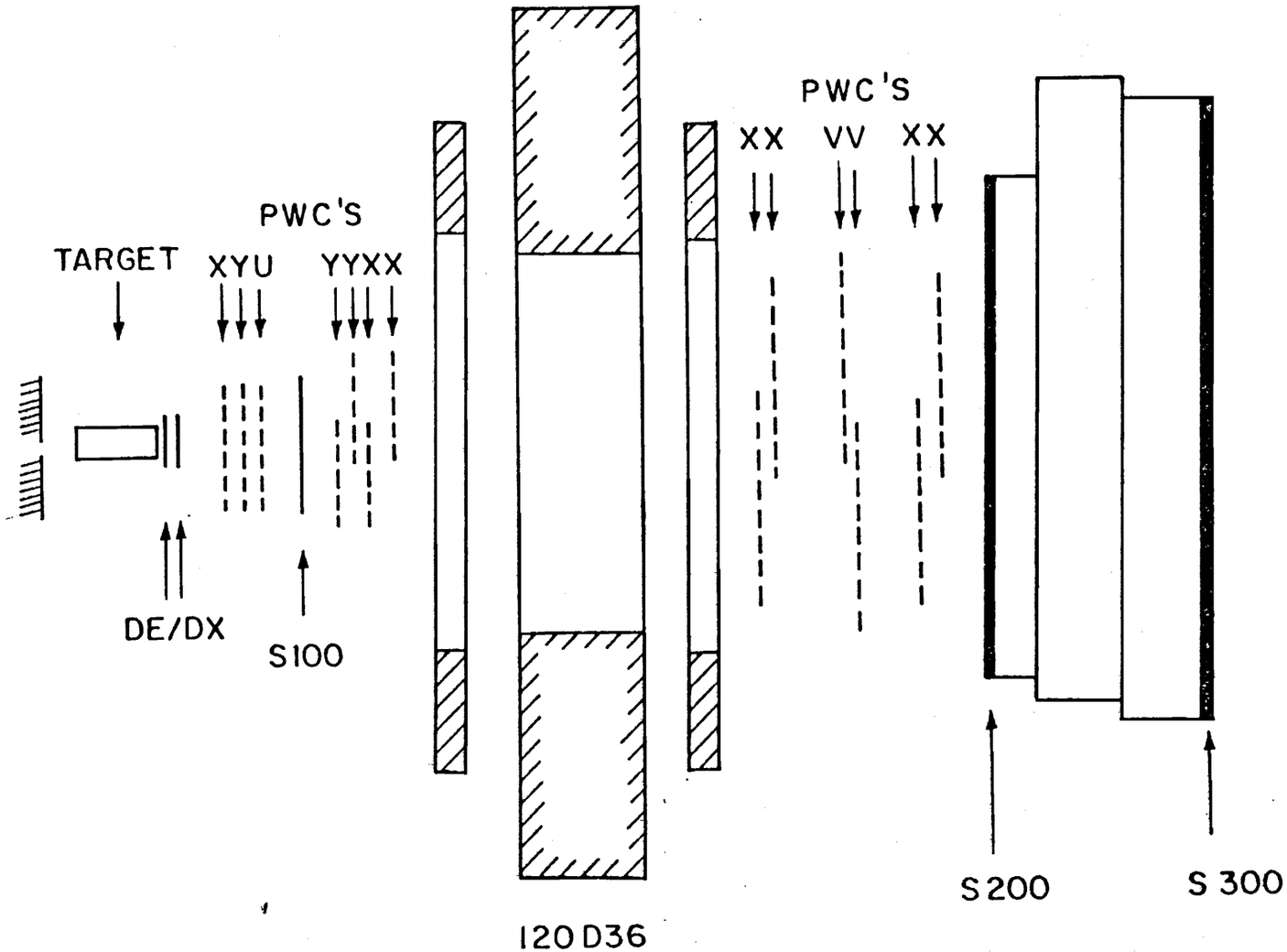

Figure 4-1. A schematic of the muon spectrometer indicating the positions of the MWPC's.

Upstream of the magnet were located three X chambers (1,4,7), three Y chambers (2,5,6), and one U chamber (3). Segments were formed using the Y chambers and, since particles in the magnet bend primarily in the x-z plane (except for vertical focussing which is very small), were extrapolated through the magnet to the rear tilted chambers. Similarly in the front of the magnet one could form all possible x segments from 2 or 3 X chambers (including the appropriate S100 counter). If the extrapolation of the front y segment coincided with a rear y coordinate, an attempt was made to link the front x and y segments via the U chamber. A successful link thus defined 2 lines in 3-space, one in front and one in back of the magnet. If the two lines intersected near the center of the magnet (typically within $\sim$ 5 mm) the lines were labelled as a valid track.

Throughout the above algorithm cuts are made on the χ^2 of the segments formed and the meeting of segments in the magnet. If all chambers were 100% efficient this procedure would be relatively simple. Unfortunately, this is not the case. For example, if chambers 1-2-3-6-7-8-10-13 fired and chambers 4-5 missed, the track is still well defined. The program handled this problem by first looking only for spark combinations in the ideal case of all chambers firing. If valid tracks were found, the participating sparks were 'extinguished' (labelled as used) and thereafter ignored. Then the program would look for possible chamber combinations in which one misfired, and so forth.

One problem with track reconstruction was the possibility of electromagnetic showers accompanying an event and causing a large number of hits in the front chambers. This made the number of possible combinations forming segments too large for the program to search in an efficient way. Thus an event was not considered for reconstruction if more than 8 hits were in a single front chamber. (A 'hit' here means a 'logical hit', whereby several adjacent wires pulsing are considered as one hit). This did not seriously affect the efficiency of multi-muon event detection since a genuine prompt trimuon at our energy leaves little missing energy to be found in the form of a shower.

All the original information from the raw data tapes plus the track information was written onto DST's which formed the data base for all further analysis.

4B. EVENT EXTRACTION

In the search for trimuon and dimuon events, all of the DST's were scanned for events with at least two reconstructed tracks. The only other cut made was on run number (calibration runs and runs with equipment failure were not included). This resulted in 3 DST's containing 9890 events from the bare target runs and 14579 events from the brass absorber runs.

All multimuon events discussed in the following sections were extracted with several initial cuts. It was always required that there be only one beam track in the entrance hodoscope system in order to eliminate events containing beam muons. However, if adjacent elements of a hodoscope plane fired, their positions were averaged and one beam muon was assumed. From the TDC information it was required that all tracks be in time with each other to within ± 4 nsec in the front S100 hodoscope and ± 6 nsec in the rear S200 and S300 hodoscopes. This helped cut down on events containing beam halo tracks or beam tracks which arrived out of time. Finally, the event was considered only if it was set by the TS^2 or TS^3 trigger. This procedure left 8146 candidates from the bare target and 12525 candidates from the absorber runs. These cuts are summarized in Table 4-1.

Trimuons were extracted by first making a series of 'loose' cuts. The multi-muon DST's were scanned for events containing three tracks of the charge combination +--. At least one of these tracks had to have momentum $p > 2$ Gev/c since the muon detection threshold was of that order. The trajectories of the tracks were extrapolated to the S300 plane, where it was required that at least two tracks intersect to within 75 mm S300 counters that were on. Of course the trigger required that two S300's be set, but they very often fired when not associated with a reconstructed track (false triggers can be caused by knock-on electrons,

TABLE 4-1

Initial Cuts on Multimuon Data

	Events Surviving	
	Bare Target	Absorber in
Raw candidates	9890	14579
One beam track in beam hodoscope	9445	13573
Timing and trigger	8146	12525

beam halo muons, etc.).

Next the three tracks were tested for vertexing. They were extrapolated into the target and the point of closest approach of the beam track and the three tracks was defined as the vertex. The technique used is described in reference 1 and yields the 'copunctuality', a measure of the relative separation of the four tracks. This was cut at 100 mm^2. It was then required that the vertex lie within the target in the x-y plane and within 40 cm of the target in the z direction. Vertex resolution was worst along the z axis since the trimuons (especially tridents) were produced at narrow angles relative to the beam and multiple-scattering in the target and absorber severely smeared the apparent z coordinate of the vertex.

An attempt was made to compensate for the multiple scattering by performing a maximum likelihood fit to the slopes of each track under the assumption that they came from a point[2]. This method is described in reference 3. While in principle this technique extracts the geometry of an event more accurately than direct extrapolation of the observed tracks, its validity was questionable. For many events ($\sim$50%) no solution for the maximum of the likelihood function could be found within the boundaries of the target, perhaps due to the large effect multiple scattering has on vertex resolution when the particles are produced at very small angles. Events with no solution were retained in the data set.

Finally, each of the three tracks and the beam track were assigned energies at the vertex position by taking their measured momentum and tracing them through all materials, accounting for energy loss along the way. We define the missing energy

$$\Delta E = E_{beam} - \sum_{i} E_i \qquad (4.1)$$

and a cut -4 Gev $< \Delta E <$ 10 Gev was imposed.

These 'loose' trimuon cuts are summarized in Table 4-2. Events satisfying the cuts were written onto 'compressed DST' tapes which contained all track information, the counters and chambers participating in each track, and the trigger. These tapes were used in the final physics analysis of the events.

Dimuon candidates were extracted in a very similar way. The DST's were scanned for events with 2 reconstructed tracks of the charge combinations +- and --. Both tracks were required to have sufficient energy to penetrate the muon filter and both had to intersect different S300 counters which were latched. All other cuts were the same as for the trimuons and are summarized in Table 4-3. Candidates were recorded on compressed DST's for further analysis.

TABLE 4-2

Initial Trimuon Cuts, Bare Target

	Events Surviving
Candidates	8146
3 tracks +--,	
one with P > 2 Gev c	843
2 tracks hit S300	748
Copunctuality < 100 mm	721
Vertex position	694
-4 Gev $< \Delta E <$ 10 Gev	670

TABLE 4-3

Initial Dimuon Cuts, Bare Target

	Events Surviving	
	+ -	- -
Candidates	8146	8146
2 muons correct charges	570	593
Vertex position	528	568
Copunctuality	519	557

4C. CROSS SECTIONS

To obtain differential and total cross sections from raw data it is necessary to impose certain restrictions on the kinematic variables of the data that is accepted. Furthermore, a good understanding of the acceptance of the apparatus in a variety of kinematic variables is required. It is for this reason that practically any high energy physics experiment requires a detailed Monte Carlo program. It is the only practical way of accounting for the many complex restrictions on the events that will be detected due to the configuration of the apparatus. This procedures requires a model of the physical process under study. While the acceptance is in principle only dependent on the geometry and characteristics of the apparatus, in practice the acceptance becomes dependent on the properties of the reactions one inputs to the calculation. When one integrates over some range of some variables (instead of the entire phase space over a complete set of variables), correlations occur between different kinematic variables. For example, if one desires the acceptance in momentum for a single track, that acceptance can depend on the correlations between angle and momentum assumed in the Monte Carlo model.

Nevertheless, for trident production fairly reliable theoretical models exist. The muon trident model is quantum electrodynamics, certainly the most accurate and reliable dynamical theory in physics. The muon-induced hadron production of section 3C possesses a number of uncertainties

(most notably in the distribution of the final state hadrons), yet the structure functions have been well measured.

The acceptance was calculated as follows. The weights of events input to the Monte-Carlo programs (trials) were summed in each bin of each kinematic variable. After tracing events through the apparatus, checking the trigger requirements, and making kinematic cuts the weights of the surviving events (successes) were summed. Then the acceptance is defined

$$A = \frac{\sum_{\text{succ}} W_i}{\sum_{\text{trials}} W_i} \qquad (4.2)$$

As straightforward as this procedure sounds, special care is necessary to avoid errors. When an event is fed to the Monte Carlo program ('picked') the values of its kinematic variables are precisely defined and the weights added to the appropriate bins. However, the values of the same variables as measured in the apparatus ('seen') are shifted from the picked values due to the finite experimental resolution of the detectors (i.e. multiple scattering, measurement errors, etc.). For example, if a muon pair final state with 'picked' effective mass M is traced through the apparatus with the leadglass target (no absorbers) its 'seen' mass will typically lie within the range $M \pm 40$ Mev c^2.

Since the effective mass has a physical lower limit, the effect here is to 'smear' the Monte Carlo events from lower to higher bins. As long as the smearing is only of the order of a bin size (masses were binned in 50 Mev/c^2 intervals), the uncertainty introduced into the acceptance is not too serious, as the results of this analysis will bear out. The severity of the problem of course will vary with different experiments.

We define the differential cross section in a variable x in the i^{th} bin to be

$$\left.\frac{d\sigma}{dx}\right|_{x=x_i} = \frac{\Delta N}{F \cdot T \cdot A_i \cdot \Delta x} \tag{4.3}$$

where ΔN_i is the number of observed events in the bin, F is the accumulated flux of incident beam particles, T is the number of target particles per unit area, A_i is the acceptance for the variable x in the i^{th} bin, and Δx is the bin size. The total cross section is the integral of $d\sigma/dx$ over the entire kinematic range of x. If the experiment covers the entire range of x we can write

$$\sigma_{TOT} = \sum_i \left.\frac{d\sigma}{dx}\right|_{x=x_i} \Delta x \tag{4.4}$$

$$= \sum_i \frac{\Delta N_i}{F \cdot T \cdot A} = \frac{N}{F \cdot T \cdot A}$$

Since we expect the majority of trimuon events to be accounted for by the trident process, acceptances found with the trident Monte Carlo were used. Some of these are shown in Figures 4-2 a-c. Figure 4-2a shows A as a function of like-charge dimuon mass, Figure 4-2b for the energy of the non-beamlike muon, and in Figure 4-2c for the transverse momentum of a single muon.

Acceptances for dimuons were more difficult to obtain since the actual source of the large yield of events wasn't known. We assumed that dimuons were due to a combination of tridents where one muon escapes detection, and meson decay. The procedure was as described above except that weights from both types of events were summed in the bins. The normalizations for both dimuon backgrounds were absolute, so their relative contributions were fixed.

4D. FINAL EVENT CUTS

To obtain the final set of events for interpreting the physics in the data, the compressed DST's were scanned and the cuts 'tightened'. This section describes the cutting procedure which defined the events used in the analysis in the following chapter. These final cuts were sometimes motivated by the results from the Monte Carlo studies.

The trimuon events were subjected to a tighter vertex cut of $\pm$20 cm from the target along the z direction and a copunctuality cut of 30 mm. Next, all three muons were re-

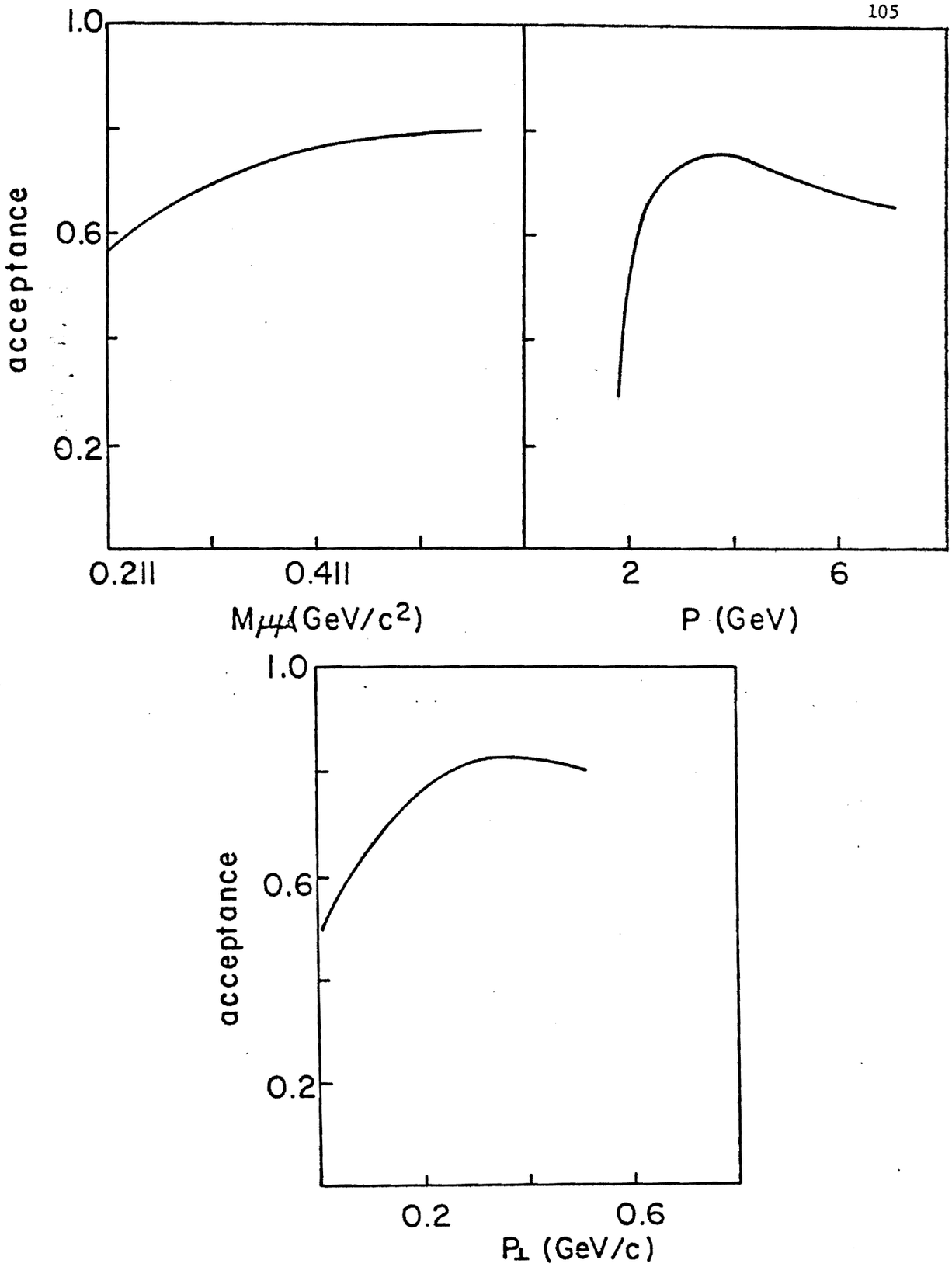

Figure 4-2. Acceptances calculated from the trident Monte Carlo. Shown are acceptances in the like-charge pair mass, the momentum of a final state muon, and the transverse momentum of a final state muon (all for $p > 1.8$ Gev/c).

quired to have momentum p > 1.8 Gev/c. The momentum cut helped guarantee muon identification and restricted the events to kinematic regions of good detection efficiency (low momentum tracks were bent through large angles in the dipole magnet and often missed the rear chambers and counters). All three tracks were required to extrapolate to S300 counters that had fired. However, in approximately 25% of the events two of the tracks intersected the same counter making absolute muon identification impossible. These events did not seem to differ from events with three identified muons in terms of the distributions of the physical variables. Also, if the event was a 'real' trident, the presence of two muons implied a third one. Finally, the presence of events with ambiguous μ-identification was consistent with the predictions of the Monte Carlo calculation. For these reasons, and in the interest of preserving statistics, these events were retained in the sample.

This procedure left 158 raw trimuon candidates. Their ΔE distribution is shown in Figure 4-3, where a clear peak is seen about $\Delta E = 0$ with FWHM = .920 Gev. The width of this peak is in excellent agreement with the Monte Carlo prediction for tridents. We took this to imply that the majority of trimuons are due to energy balancing processes (i.e. muon tridents and diffractive vector-meson production).

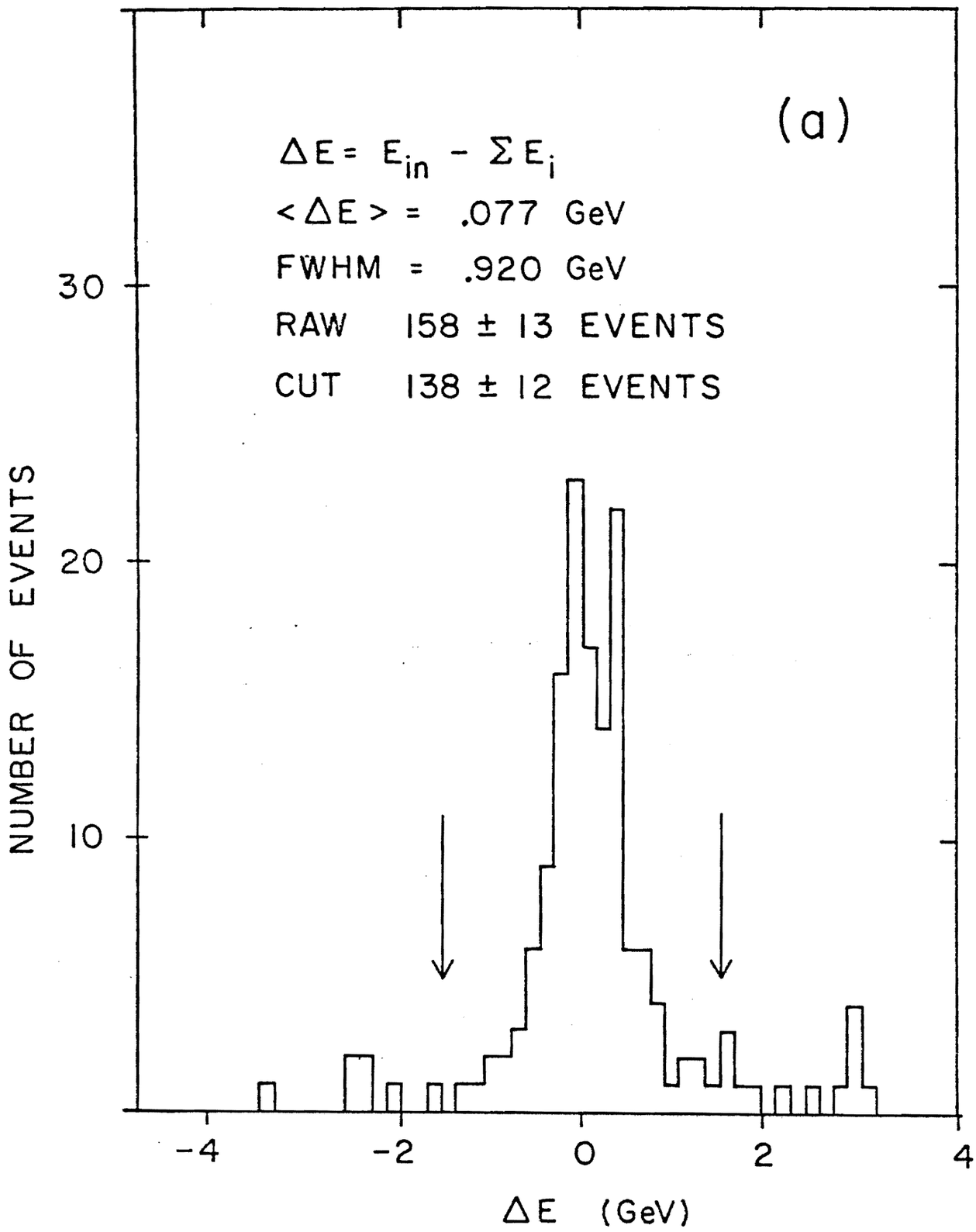

Figure 4-3. The missing energy distribution of the trimuon data. The clear peak indicates that these events are almost entirely due to energy balancing processes.

The raw events had to be corrected for detection efficiency and backgrounds. For each event, the probability that each track was reconstructable was calculated based on the efficiency of the chambers it intersected. The event was then assigned a weight

$$W = \frac{1}{P_1 P_2 P_3} \tag{4.5}$$

equal to the inverse of the product of the three reconstruction probabilities. Typically, $P_i = .90$ and $W_i = 1.35$. Thus, instead of summing the number of observed events in each bin, their weights were summed.

A possible background indistinguishable from a prompt trimuon is muon bremstrahlung followed by the conversion of the real photon into a muon pair in the target. The number of events expected from this process was calculated using the photon distributions and conversion lengths given by Tsai[4]. The calculation is given in Appendix 1, where a prediction of 6 ± 2 events is obtained. Finally, in searching for events that balance energy, we had to consider backgrounds in the ΔE distribution of Figure 4-3. Trident and vector meson production candidates were taken to be all events in the region $|\Delta E| < 1.5$ Gev assuming a uniformly flat background. This amounted to a correction of -28 ± 5 events in the final normalization. In the case of event distributions the appropriate fraction of the corresponding

spectrum of the events falling outside the ΔE cut was subtracted from the spectrum of the events inside the ΔE cut.

The final trimuon cuts are listed in Table 4-4. As a check of the above procedures, Figure 4-4 shows the final corrected event sample's Z-vertex distribution together with the Monte Carlo prediction. The agreement in absolute normalization and in shape is very good.

One other check applied throughout this procedure was a visual inspection of all trimuon and dimuon events on the compressed DST. This was done by creating CALCOMP tapes of schematic pictures of the apparatus and all reconstructed tracks. The pictures were then photographed on rolls of 35 mm film. A typical event schematic is shown is Figure 4-5. Scanning the events individually aided in determining the necessity or validity of the various cuts, and especially helped in understanding the muon identification problem.

TABLE 4-4

Final Trimuon Cuts

Raw candidates	670
2 different S300 counters	456
Geometry and momentum cuts, muon identification	158
$\|\Delta E\| < 1.5$ Gev	138 ± 12
Corrections	
Detection and reconstruction efficiency	$+33 \pm 6$
Background	-28 ± 5
Bremstrahlung plus pair-production	-6 ± 2
Total yield	137 ± 14

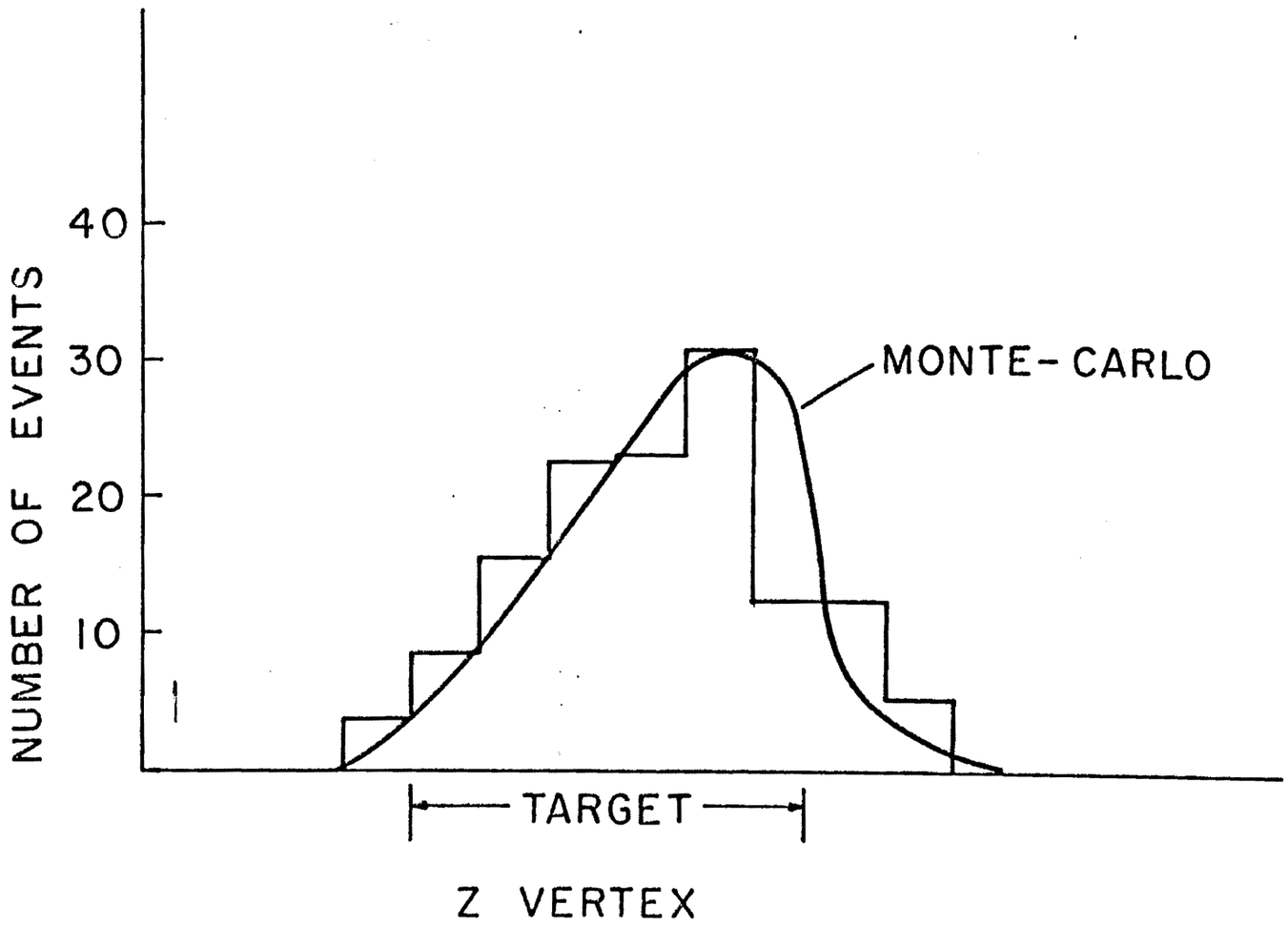

Figure 4-4. The event distribution in the vertex position of the trident events. The curve represents the Monte Carlo prediction with absolute normalization.

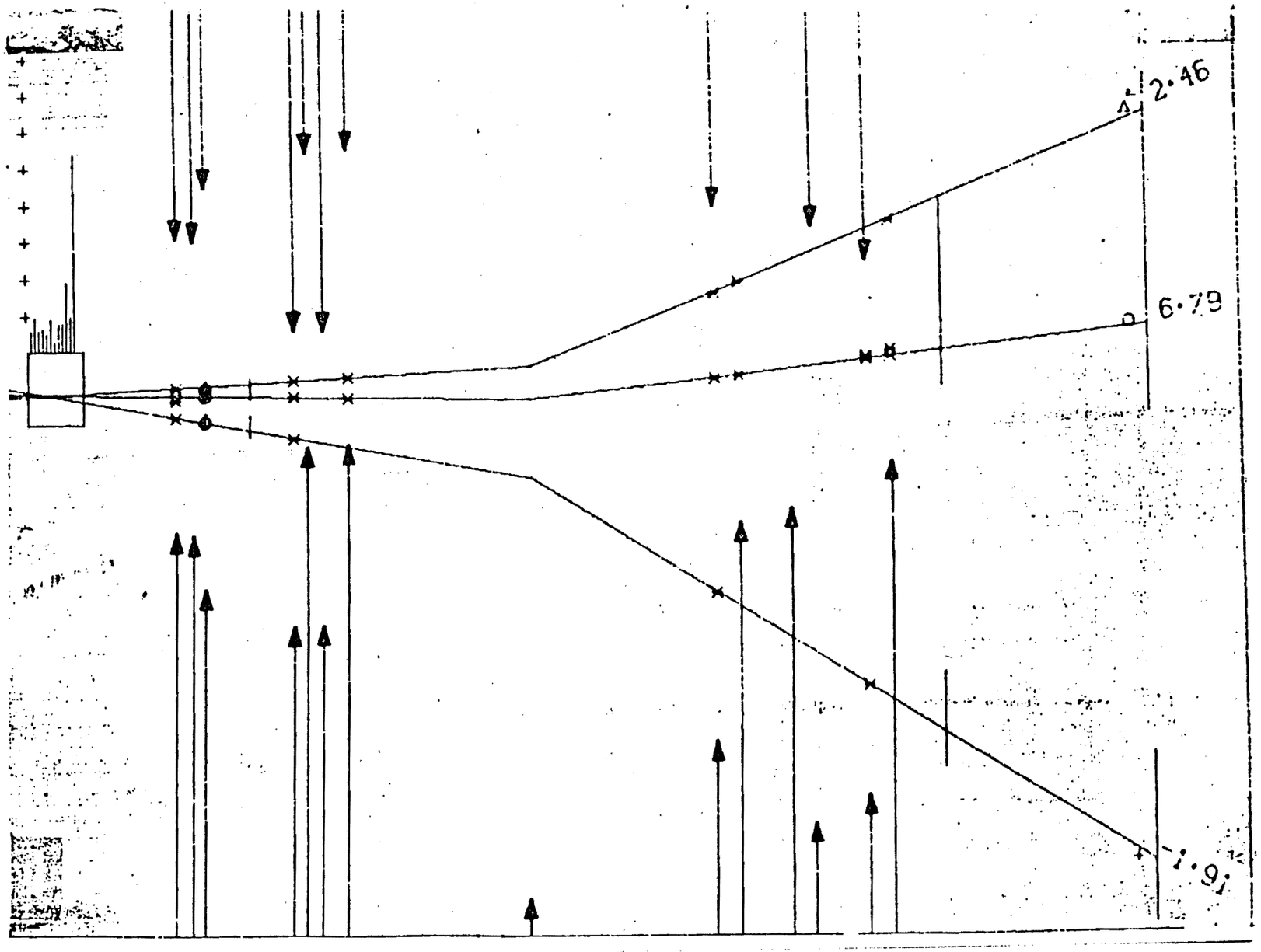

Figure 4-5. A schematic of a trimuon event.

REFERENCES

1. S. K. Tewksbury, University of Rochester thesis, 1969 (unpublished)

2. Chicago-Princeton collaboration, private communication

3. D. McCal, University of Rochester thesis, 1979 (unpublished)

4. Y. Tsai, Rev. Mod. Phys. 46, 815 (1974)

CHAPTER 5

RESULTS

5A. ELASTIC EVENTS -TRIDENTS

We first turn our attention to the events satisfying the 'tight' trimuon cuts described in section 4D, including the elasticity cut $|\Delta E| < 1.5$ Gev. The majority of these events can probably be accounted for by the trident process. Therefore, in this section the results of the QED calculation and Monte Carlo are compared with the observed differential cross sections. In each of the figures in this section, the solid curves represent the theoretical cross section for tridents <u>with</u> fermion exchange and a momentum cut $p > 1.8$ Gev/c for each final state muon. These curves are to be compared with the data. Dotted curves show the same cross section assuming no exchange for muons. Dashed curves represent the total cross section (no momentum cut) for Fermi-Dirac muons, and are only meant to illustrate what piece of the total cross section is actually observed.

Figure 5-1 shows the differential cross section in the energy E_+ of the final state μ^+. The agreement with the QED prediction is excellent both in normalization and shape.

A clearer check of QED is shown in Figure 5-2, where $d\sigma / dM_{\mu^-\mu^-}$ is plotted. As mentioned in section 1B, this distribution tests for the low mass suppression of the cross section expected from the exchange interference between muons. Not only is the good agreement with QED clear, but the fermion hypothesis is clearly favored. Figure 5-3 displays (on a linear scale) the number of (corrected) observed events as a function of $M_{\mu^-\mu^-}$. The two bands represent the predictions for fermions and for no exchange, the band widths corresponding to the error in the Monte Carlo integration of the cross section. This is the second observation of the exchange effect for muons.

To make a comparison with previously recorded data[1] and to give a quantitative measure of the strength of the exchange interference for muons, we follow references 1 and 2 and define a parameter α such that

$$\left(\frac{d\sigma}{dM_{\mu^-\mu^-}}\right)_{MEAS} = \left(\frac{d\sigma}{dM_{\mu^-\mu^-}}\right)_{NO\ EX} + \alpha \left[\left(\frac{d\sigma}{dM_{\mu^-\mu^-}}\right)_{FERM} - \left(\frac{d\sigma}{dM_{\mu^-\mu^-}}\right)_{NO\ EX}\right] \qquad (5.1)$$

Defined in this way, $\alpha = 1$ for fermions and $\alpha = 0$ for no exchange. A bin by bin maximum likelihood fit to α was performed using the observed cross section yielding

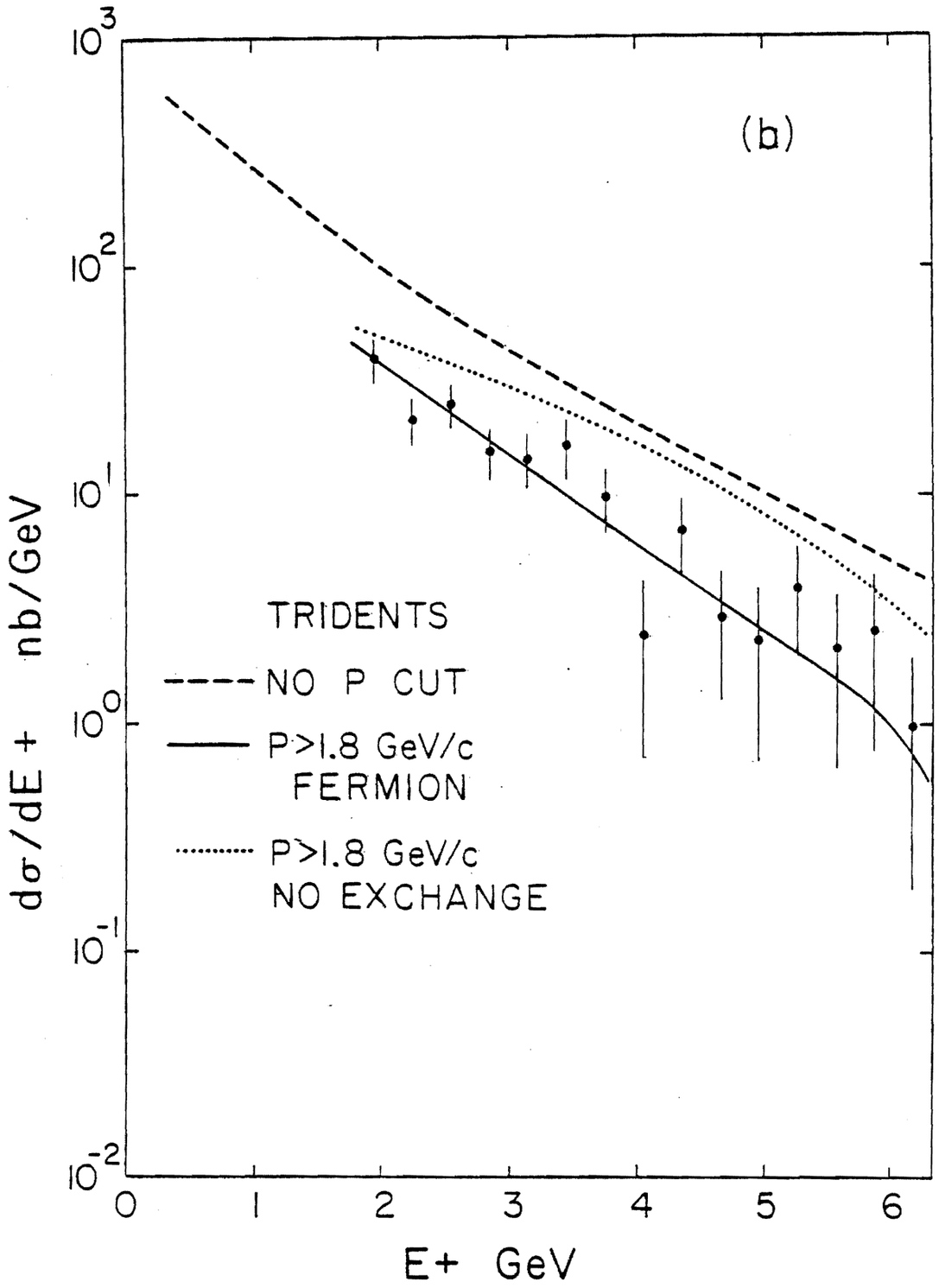

Figure 5-1. The measured differential cross section in the energy of the positive (non-beamlike) muon in the trimuon final state. Curves are described in the text.

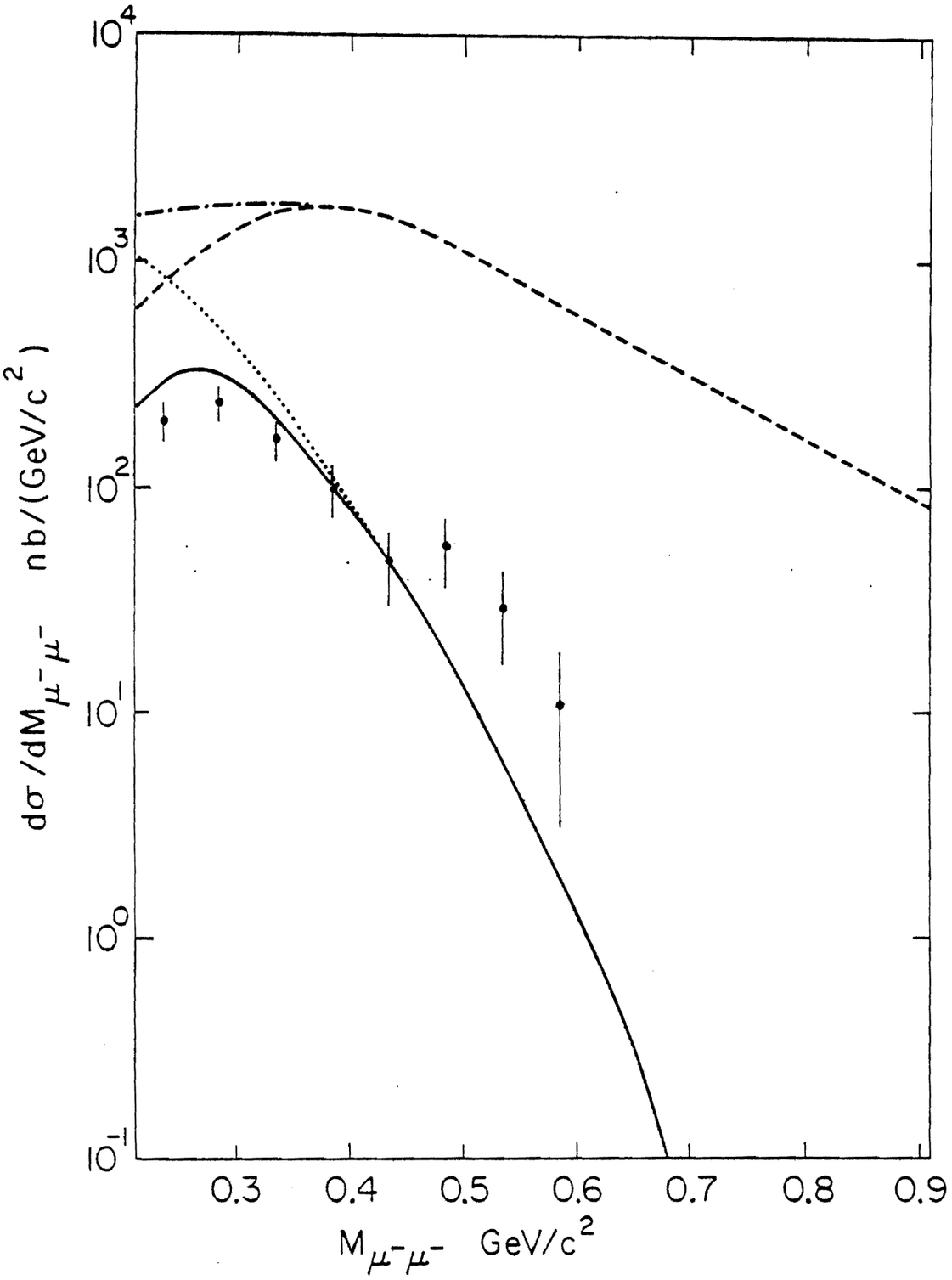

Figure 5-2. The measured differential cross section in the effective mass of the two like-charge muons in the trimuon final state.

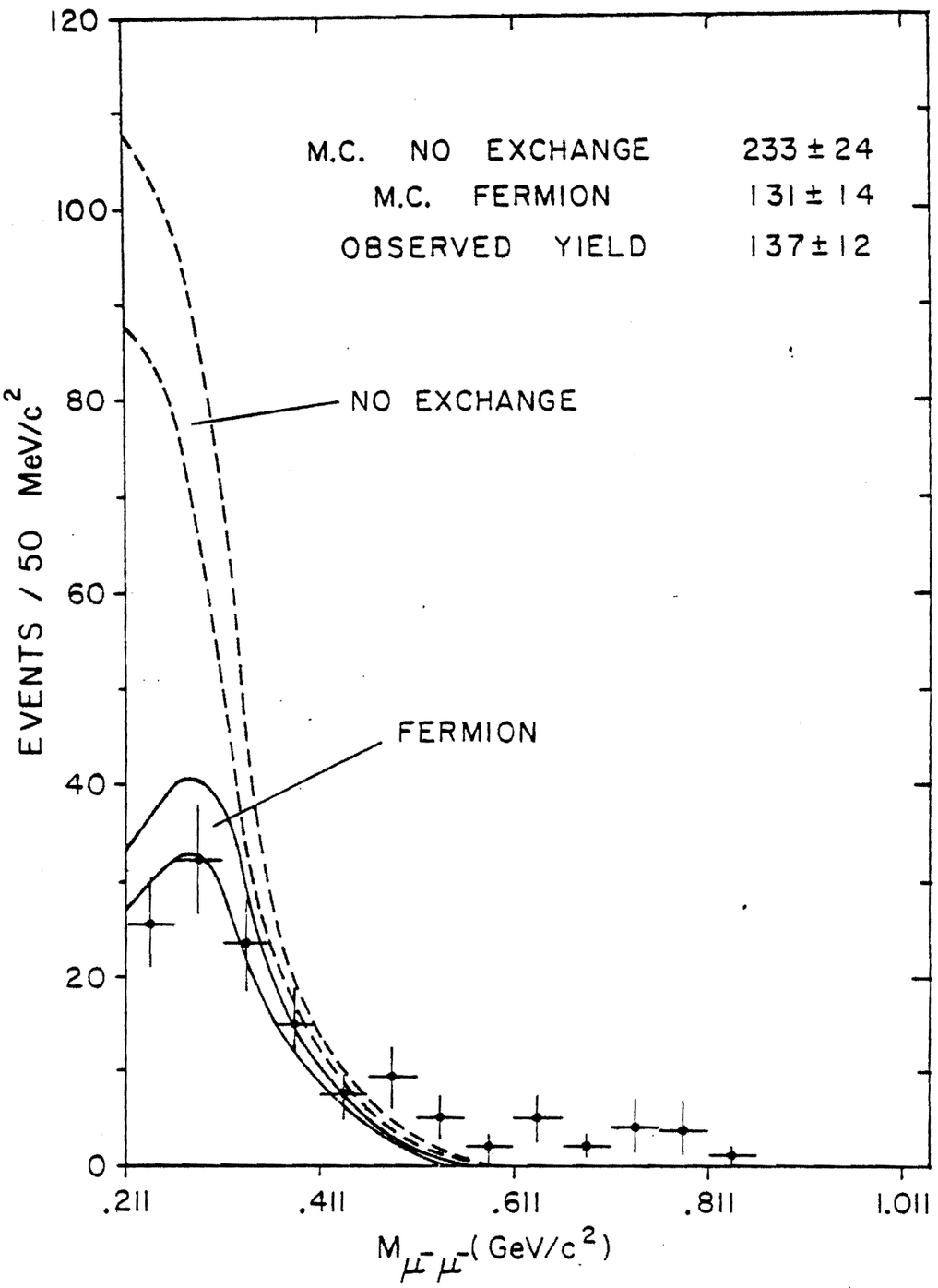

Figure 5-3. The corrected event distribution in the effective mass of the two like-charge muons in the trident final state indicating the effect of exchange interference between muons.

$$\alpha = 1.08 \pm .13 \qquad (5.2)$$

where the error combines both the fitting error and the error in the calculated theoretical cross section. Note that the fitted value of α depends almost entirely on the first four 50 Mev/c^2 bins in $M_{\mu^-\mu^-}$ where the relative (i.e. for $p > 1.8$ Gev/c) acceptance is $\sim 60\%$. This is an 8 standard deviation effect, in excellent agreement with the result of references 1 and 2, where it was found that $\alpha = 1.15 \pm .25$.

While the agreement with QED seems excellent, the absolute normalization on the data and theoretical cross sections can vary by $\pm 10\%$. The total cross sections (over the apparatus acceptance) obtained from the data and Monte Carlo integration are compared in Table 5-1. Again, the agreement is good, indicating that the large majority of trimuons must be muon tridents.

Note, however that in Figures 5-2,3 there appears to be an excess in the cross section at large dimuon effective mass $M_{\mu^-\mu^-}$. This excess also appears in the other combinations of dimuon effective mass $M_{\mu^+\mu^-}$ fast and $M_{\mu^+\mu^-}$ slow (where we use the positive muon and the fast and slow negative muon to form a pair) shown in Figures 5-4,5. This tends to indicate that the data sample contains events with opening angles larger than the $\theta \sim m_\mu / E$ expected from QED. The cross section in the effective mass of all three muons is also indicative of this effect as seen in Figure 5-6.

TABLE 5-1

Trident Cross Sections and Yields
(Nanobarns per lead nucleus)

	No exchange	Fermion	Observed
σ_{total} 1st Born approximation	739 ± 69	656 ± 67	-
σ_{total} 2nd order corrections	650 ± 61	577 ± 59	-
σ_{within} acceptance	61.8 ± 5.8	34.6 ± 3.5	36.3 ± 3.2
Number of events	233 ± 22	131 ± 14	137 ± 12

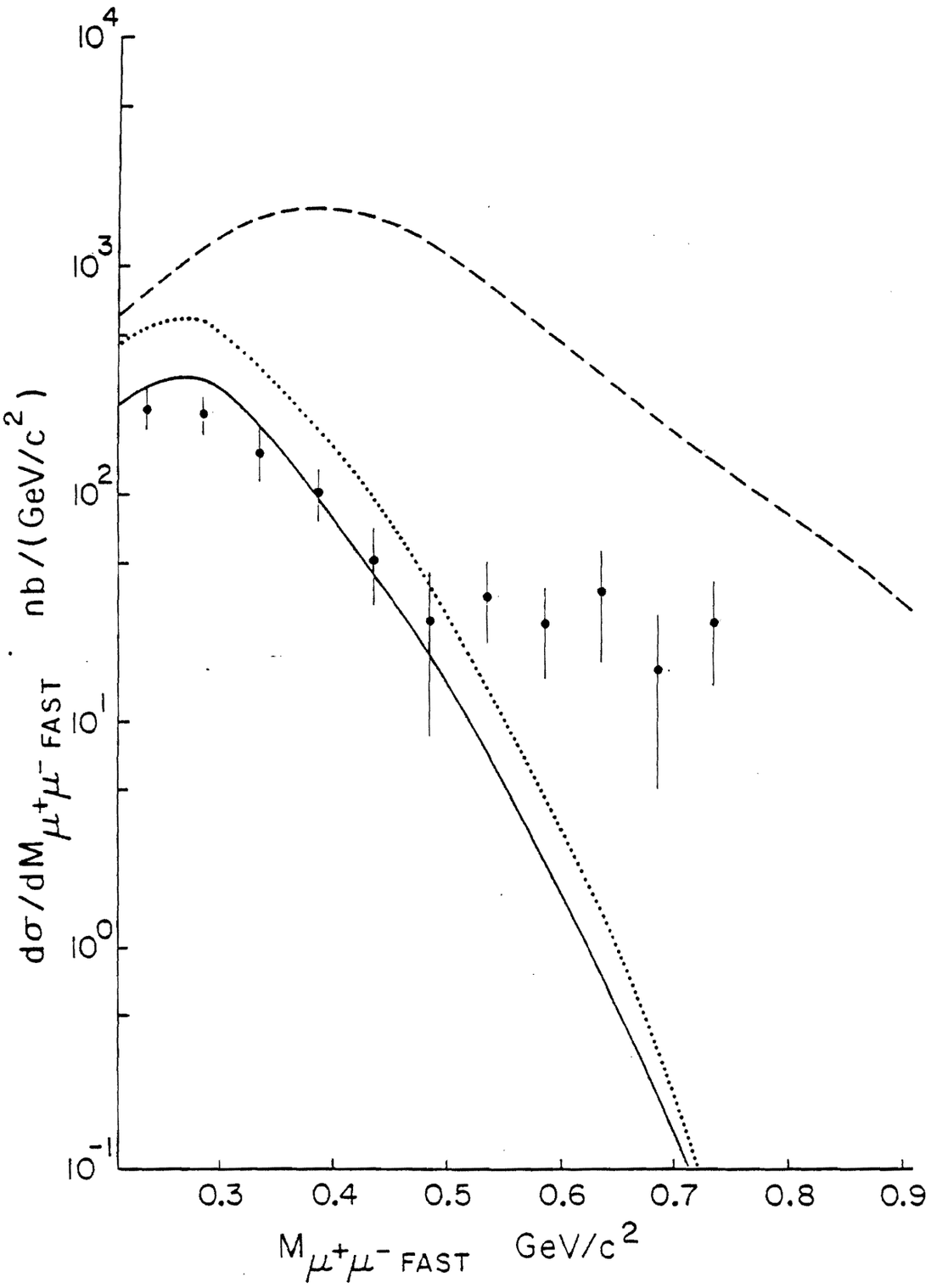

Figure 5-4. The measured differential cross section in the effective mass of a pair of opposite-sign muons in the trimuon final state where the fast beamlike muon has been used.

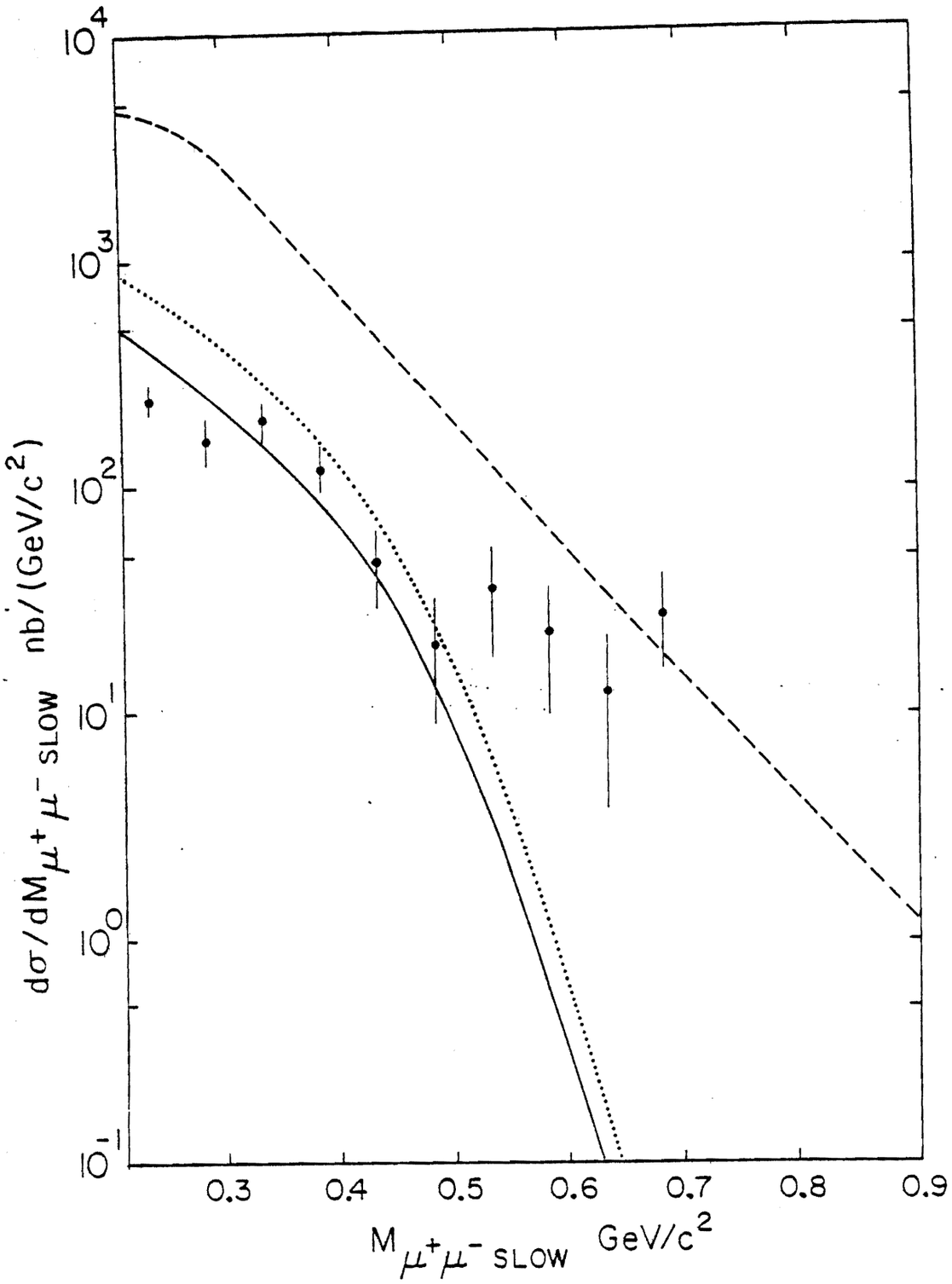

Figure 5-5. The measured differential cross section in the effective mass of a pair of opposite-sign muons in the trimuon final state where the slow beamlike muon has been used.

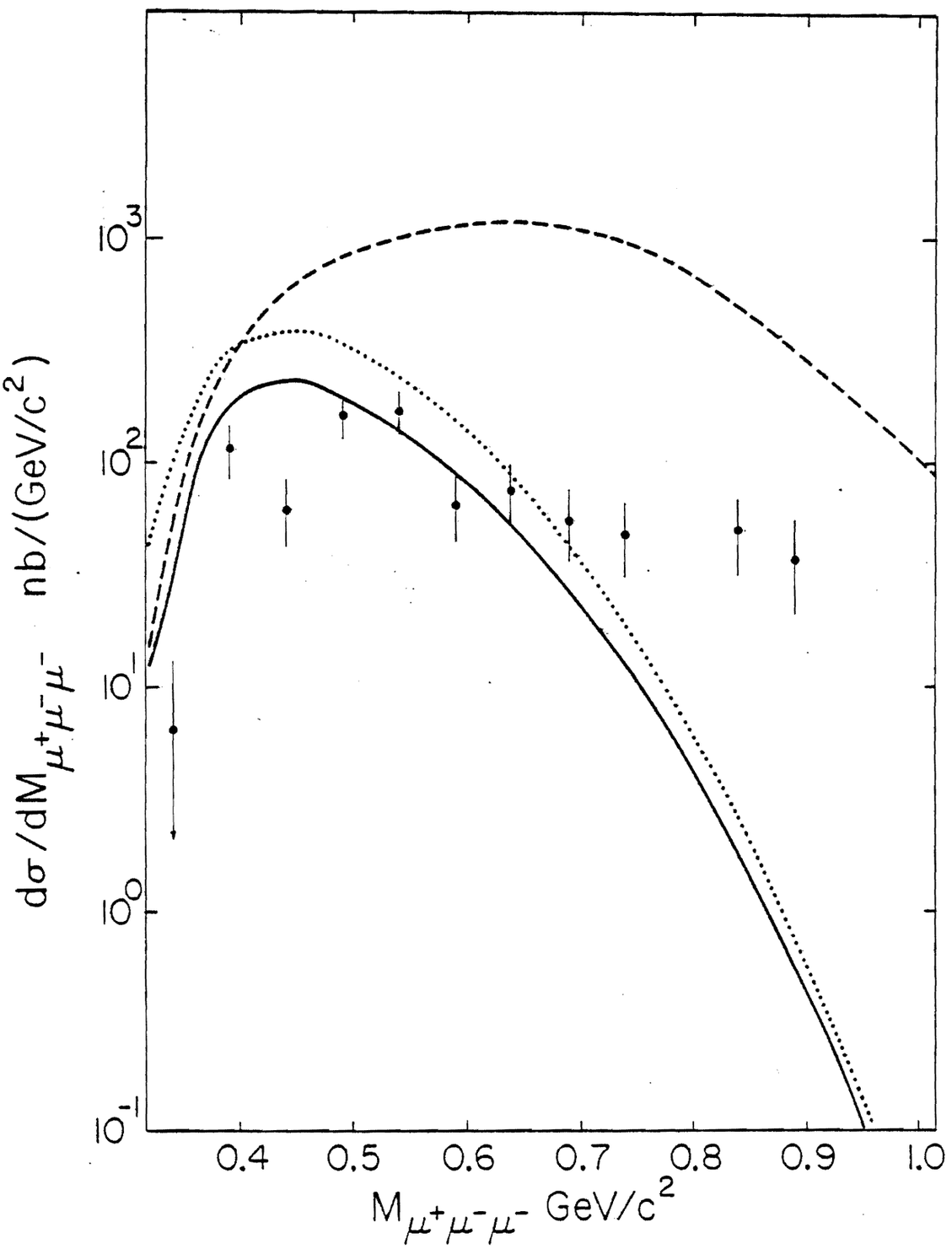

Figure 5-6. The measured differential cross section in the three-muon effective mass for the trimuon data.

As a final check of QED and of this possible excess we show in Figure 5-7 $d\sigma/dp_t^+$, the differential cross section in the transverse momentum of the produced μ^+. Again, while at low p_t the agreement with QED is good, some other mechanism seems to be making a small contribution to the data. This is discussed in the following section.

4B. ELASTIC EVENTS - NON-TRIDENTS

To investigate the events produced at relatively wide angles all of the trident cuts (including ΔE) are retained and a cut on the three-muon mass $M_{3\mu} > 700$ Mev/c^2 (see Figure 5-6) is made. This yields a sample of 16 events. In the following figures, events with $M_{3\mu} > 700$ Mev/c^2 are shown as shaded. The curves represent the Monte Carlo prediction for tridents with fermion exchange.

Figure 5-8 shows the event distribution in the change in longitudinal (beam direction) momentum. All events are uniformly spread about $\Delta p_{long} = 0$, characteristic of tridents or diffractive processes. In Figure 5-9, however, we see that the final state muons of the high mass events possess significantly more transverse momentum than could be explained by a one-photon QED process (this is to be expected since a cut on the three-muon mass was made). The data are consistent with vector meson production, where a muon from ρ-decay whould have $p_t \sim .3$-$.5$ Gev/c.

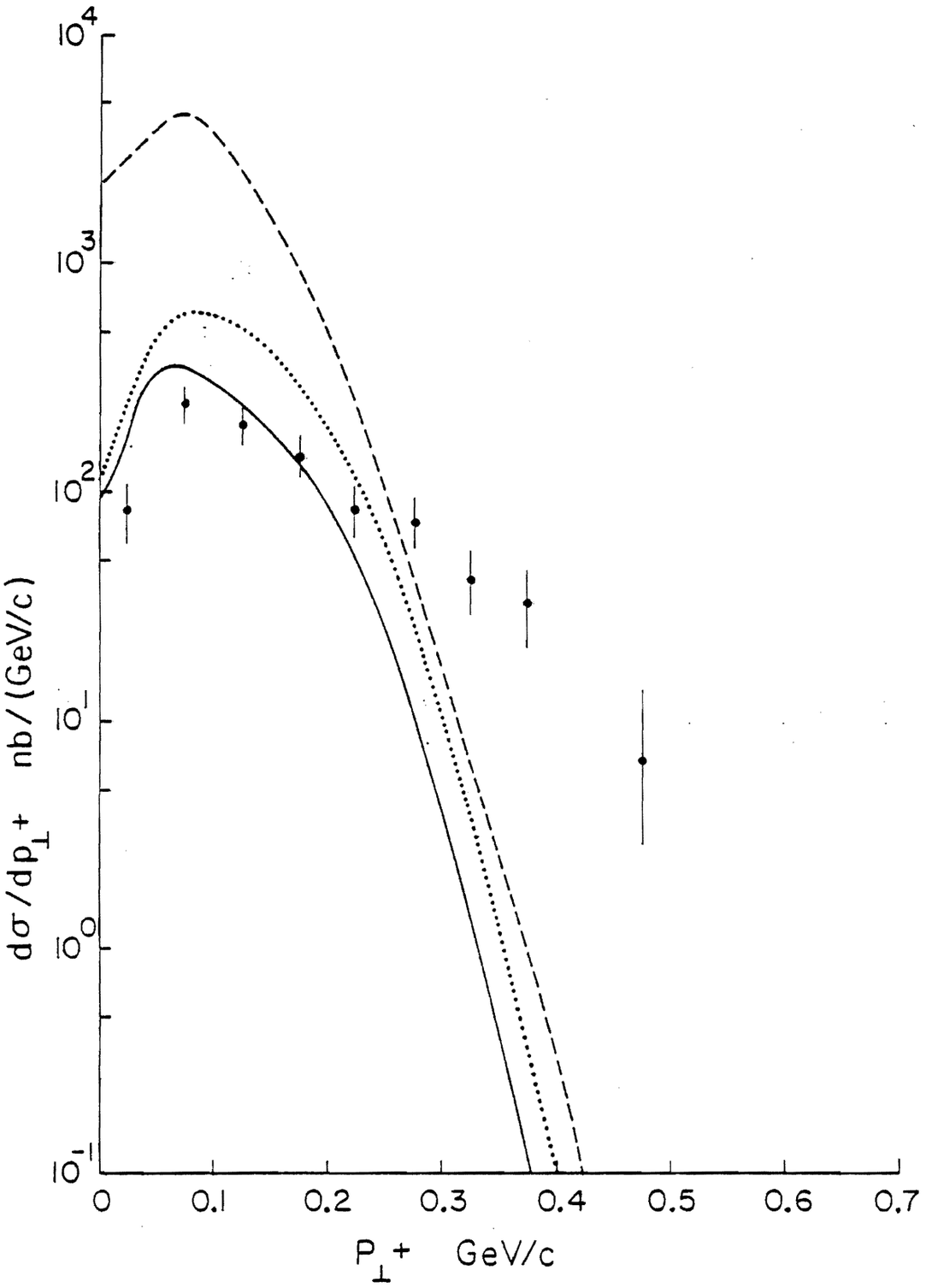

Figure 5-7. The measured differential cross section in the transverse momentum of the non-beamlike muon in the trimuon final state.

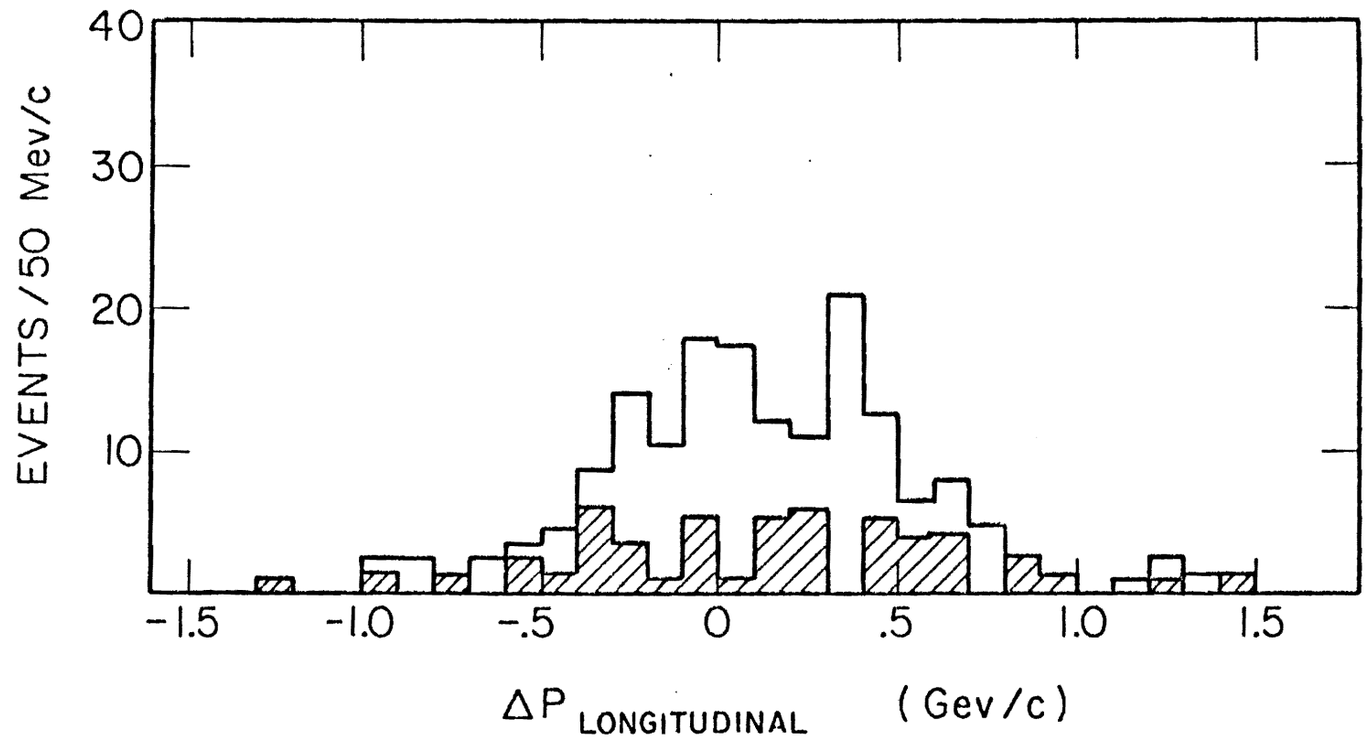

Figure 5-8. The event distribution in the change of momentum along the beam direction for the trimuon data. Shaded events indicate a three-muon mass greater than 700 Mev/c^2.

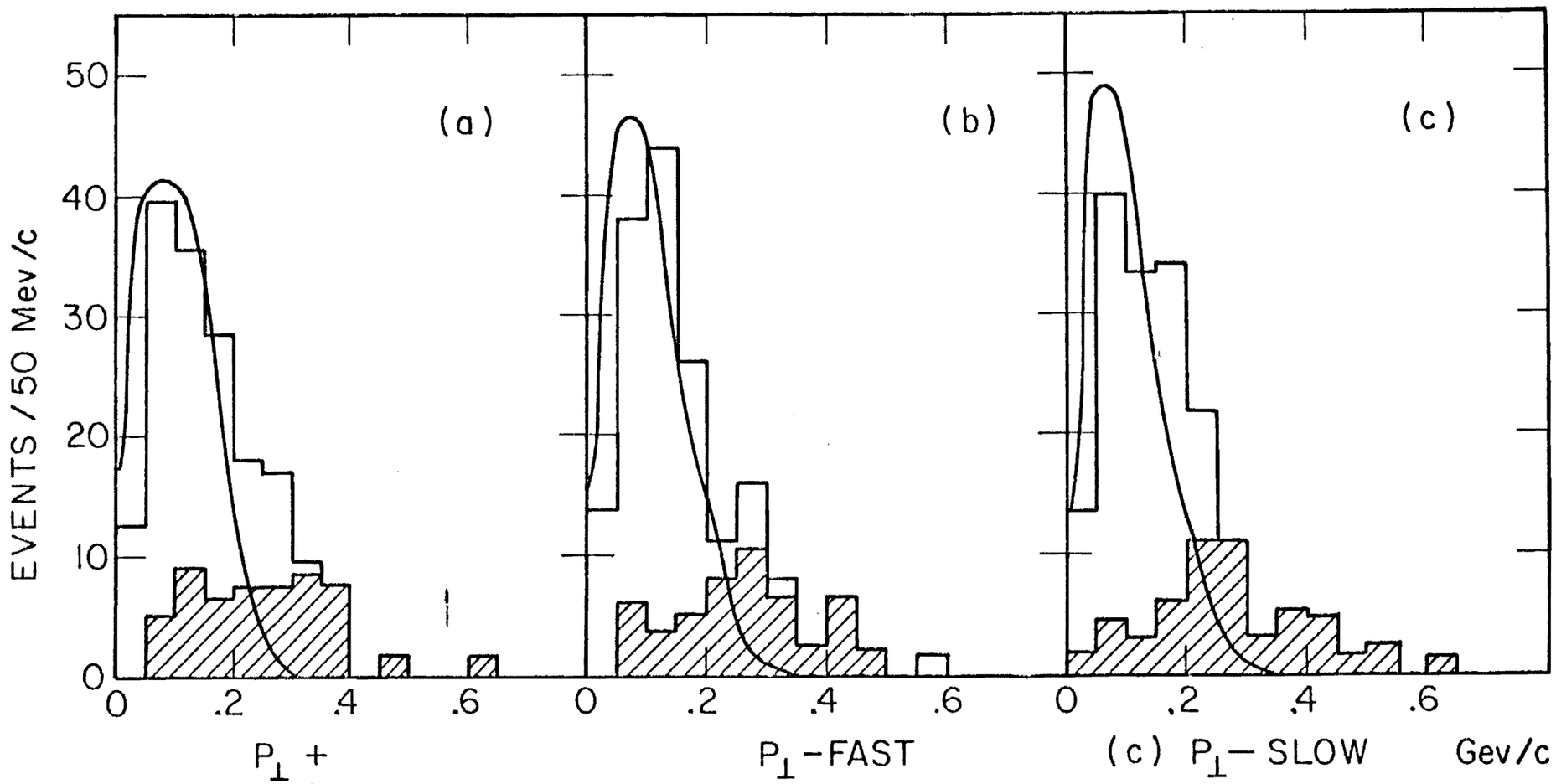

Figure 5-9. The trimuon event distributions in the transverse momentum of each final state muon. Curves indicate the distribution expected from muon trident production alone.

The clearest indicator of ρ production by the mechanism of Figure 1-3a would be a peak in the $\mu^+\mu^-$ mass distribution. Figures 5-10 a,b show the event distributions in $M_{\mu^+\mu^-}$ where we have used the fast and the slow μ^- respectively. Note that while the shaded events cluster about the ρ mass (770 Mev/c^2), no distinct peaks are evident. This can be explained by the large width of the ρ ($\sim$ 150 Mev/c^2) and the branching ratio ($\simeq 7 \times 10^{-5}$) for $\rho \rightarrow \mu^+\mu^-$. Also, the QED trident cross section falls so steeply with mass that no tridents can be expected (for this experiment's sensitivity) at the ρ mass.

In Figure 5-10c, the two $\mu^+\mu^-$ masses for the elastic trimuons are compared in a scatterplot. The two bands correspond to one full width of the ρ meson. Note that 13 events fall in this region, and that if one $\mu^+\mu^-$ pair is near the ρ , the other possible pair in fact has a lower mass. These thirteen events possess an average mass $\langle M \rangle$ = 766 Mev/c^2 with full width (2σ) 135 Mev/c^2.

The production of the ρ by virtual photons has been measured in several experiments[3]. One can therefore test the diffractive production hypothesis by extracting a cross section for comparison. This is done by using the virtual photon flux factor (see section 3C) corresponding to the Q^2 and ν of each event to obtain the cross section for

$$\gamma_v + Pb \rightarrow \rho + Pb \qquad (5.3)$$

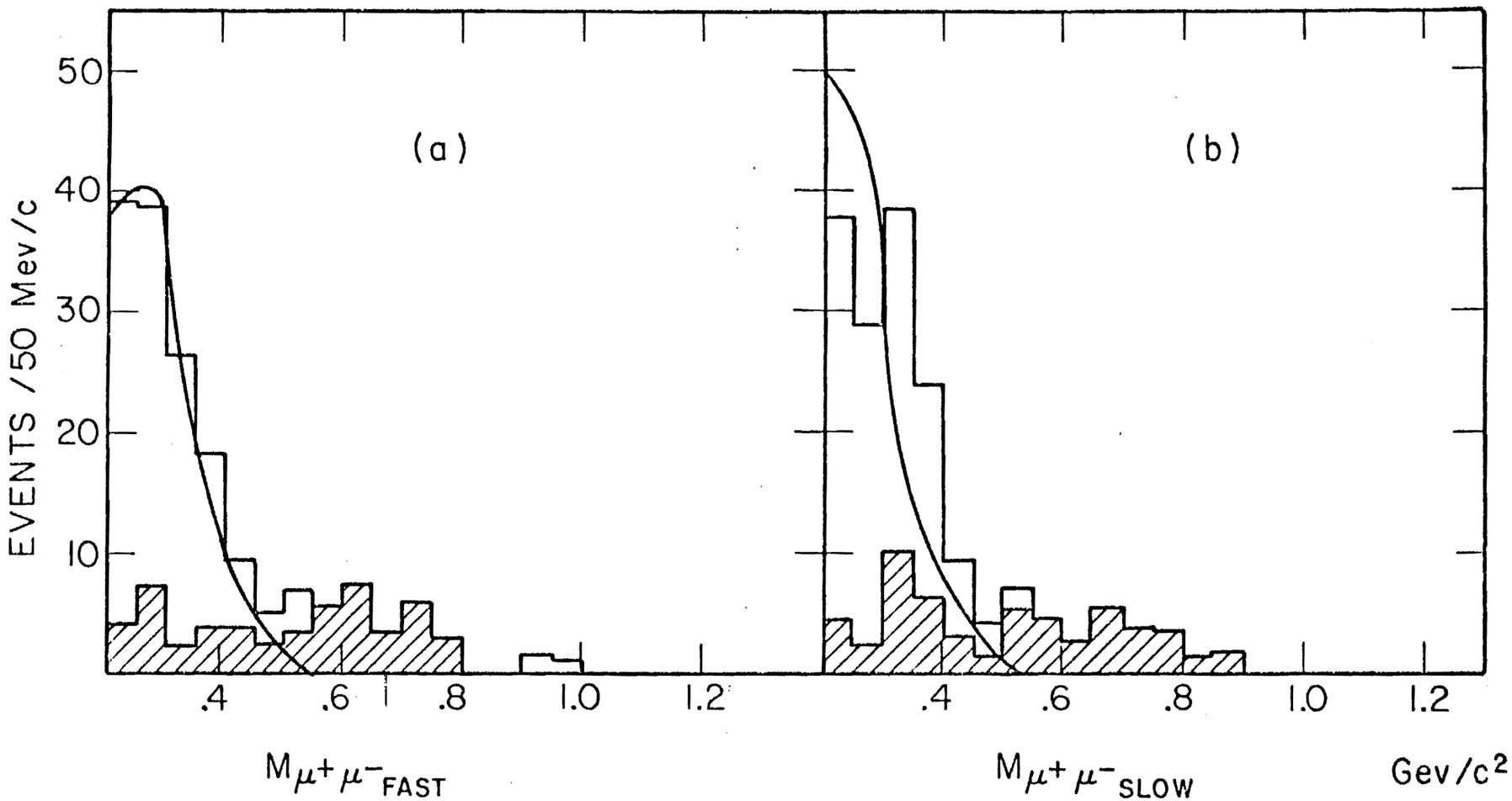

Figure 5-10. Event distributions in the effective masses of the two possible pairs of opposite sign muons from the elastic trimuon data. Shaded events have a three-muon effective mass greater than 700 Mev/c^2.

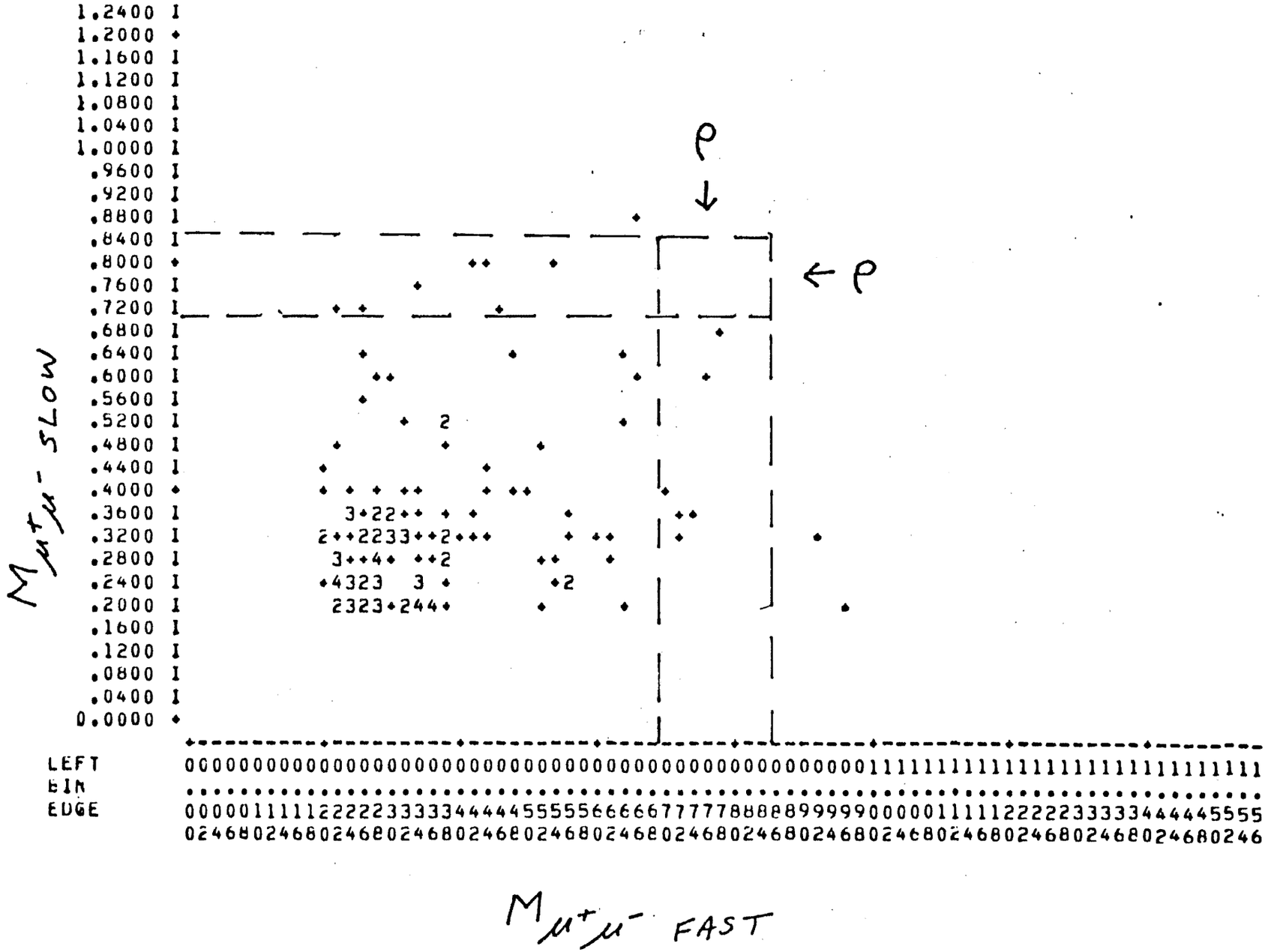

Figure 5-10(c). A scatterplot of the two effective masses of opposite-sign muon pairs for the elastic trimuon data. Thirteen events are seen to possess a pair in the region.

From simple VMD arguments, the ratio of the ρ production cross section by virtual photons to the cross section for real photons ($Q^2 = 0$) should be

$$\frac{\sigma(Q^2)}{\sigma(0)} = \frac{M_\rho^2}{(M_\rho^2 + Q^2)} \qquad (5.4)$$

The cross section ratio obtained is shown in Figure 5-11, where it is compared with SLAC[4] and Cornell[5] electroproduction data. We have assumed an $A^{1.0}$ dependence for lead and taken the real photon cross section to be 18.5 μb for our range of ν [6]. Clearly, these excess trimuons are consistent with diffractive ρ production. A more conclusive test would have to involve detecting the $\pi^+ \pi^-$ decay mode of the ρ to acquire reasonably good statistics.

5C. COMPLETE TRIMUON SAMPLE

We next examine all the trimuon events, including those outside the ΔE cut. it has been shown that muon tridents and ρ production can account for the data within the ΔE cut, yet we will examine other possibilities.

Figure 5-12 gives the complete event distribution in the three-muon effective mass. No peak appears to be present, as could be possible according to the predictions of quark dissociation in reference[10]. A total of 158 raw e-

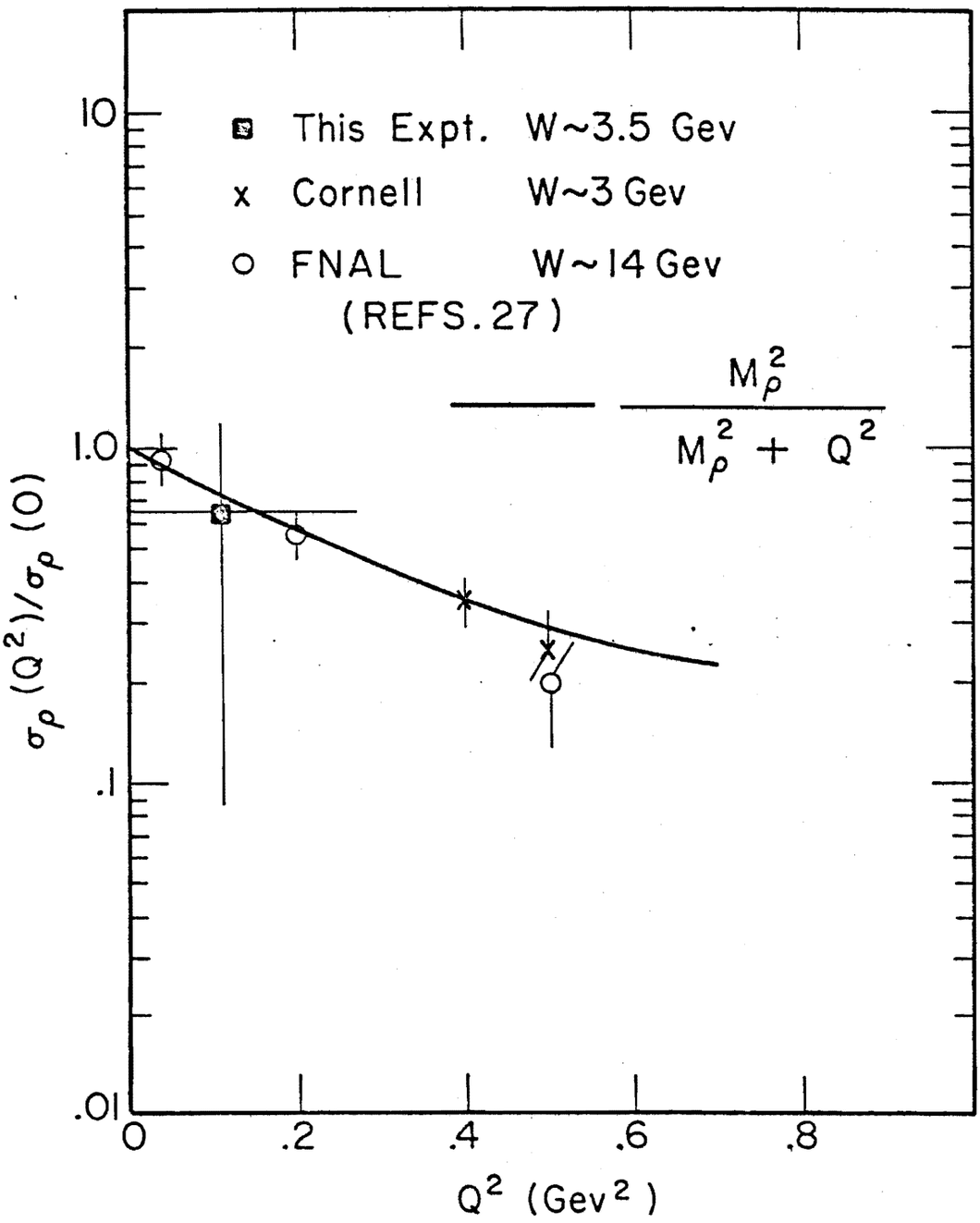

Figure 5-11. The cross section for the production of the meson by virtual photons as obtained from the 13 possible ρ events compared to other data. The hypothesis of diffractive production is clearly consistent with the results of references

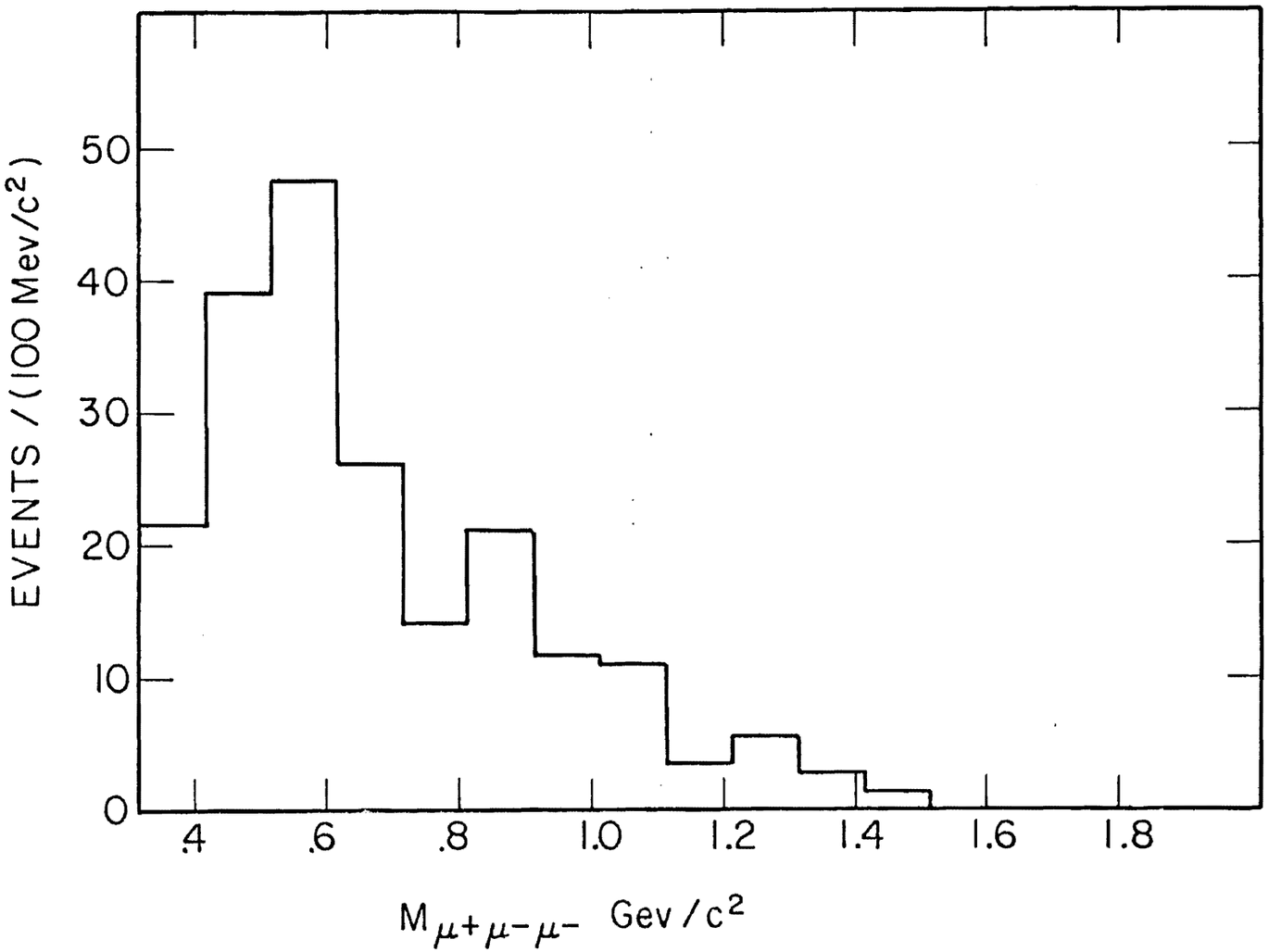

Figure 5-12. The event distribution in the three-muon mass for all 158 trimuon events.

vents are shown. Since muon tridents account so well for the data when $M_{3\mu} < 700$ Mev/c^2, we subtract the predicted trident yield and use the remaining events to establish an upper limit on $B\sigma$ for the production and decay of a particle with a three-muon decay mode. The three-muon mass resolution was typically $M_{3\mu} = \pm 70$ Mev/c^2, so the data is divided into 100 Mev/c^2 bins and the number of events in each bin is used to obtain the 90% confidence level upper limit on $B\sigma$ for that bin. The process was assumed to have an $A^{1.0}$ dependence, and the entire target composition (8.7 X 10^{25} nucleons per cm^2) was included. Mass acceptances derived from the trident Monte Carlo were used. Figure 5-13 shows the result, which applies to any exotic particle accessible at these energies which may decay into three muons.

As discussed in Chapter 1, any search for inelastic trimuons is hindered by the lack of available phase space detectable by the apparatus. A muon needs at least 2.2 Gev to be detected (> .3 Gev to exit the target and > 1.9 Gev to penetrate the muon filter).

Nevertheless the sample contains 6 events with $\Delta E > 1.5$ Gev. The effective masses of the different combinations of muons are shown in Figure 5-14. The one event shaded in is the only event of the six to show appreciable energy deposited in the leadglass target. Since there is only one unambiguous candidate for inelastic trimuons we assign 1^{+5}_{-1} events to this process. Using the entire target composition

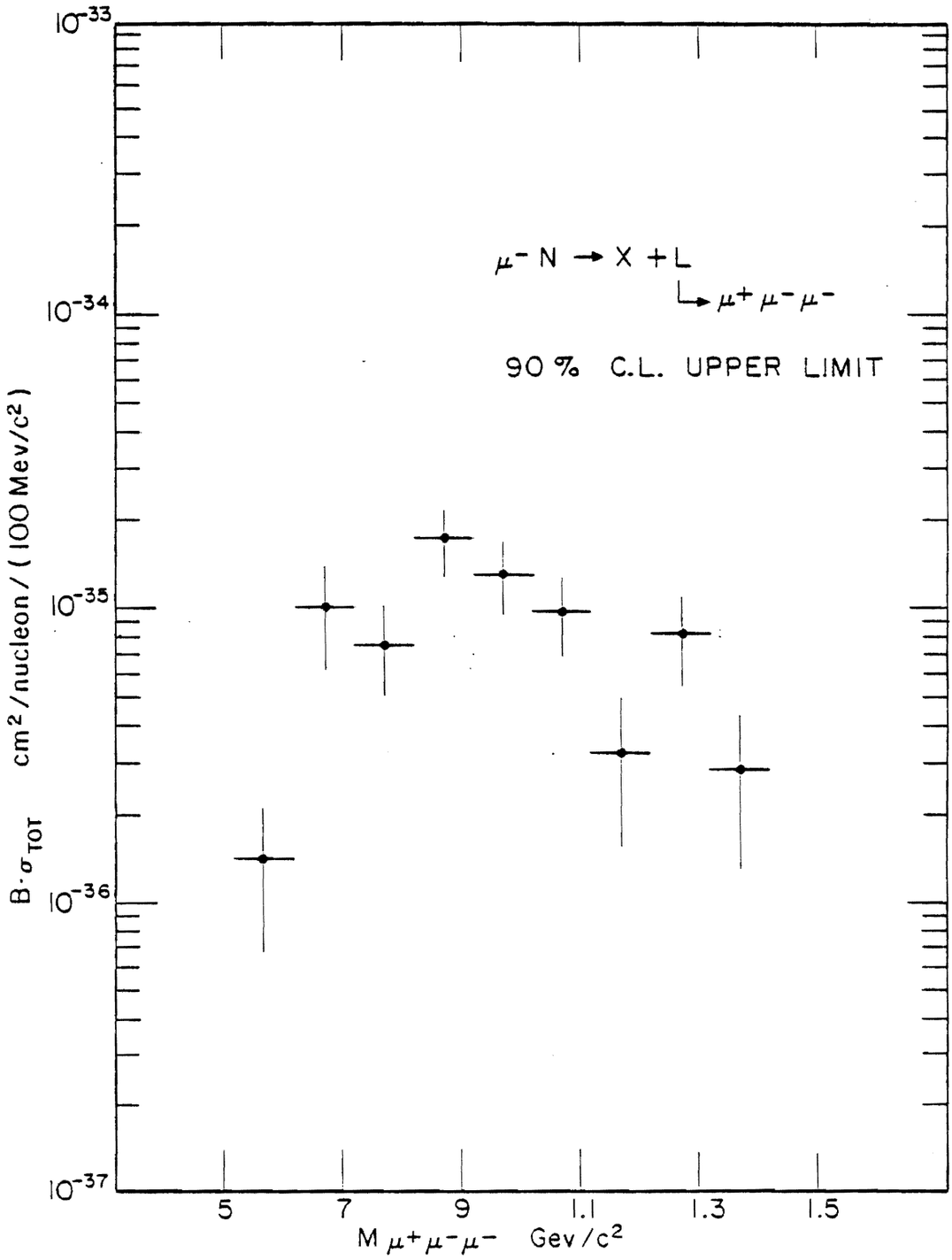

Figure 5-13. Upper limits (90% C. L.) on the production and decay of a particle possessing a three-muon decay mode as a function of the trimuon mass.

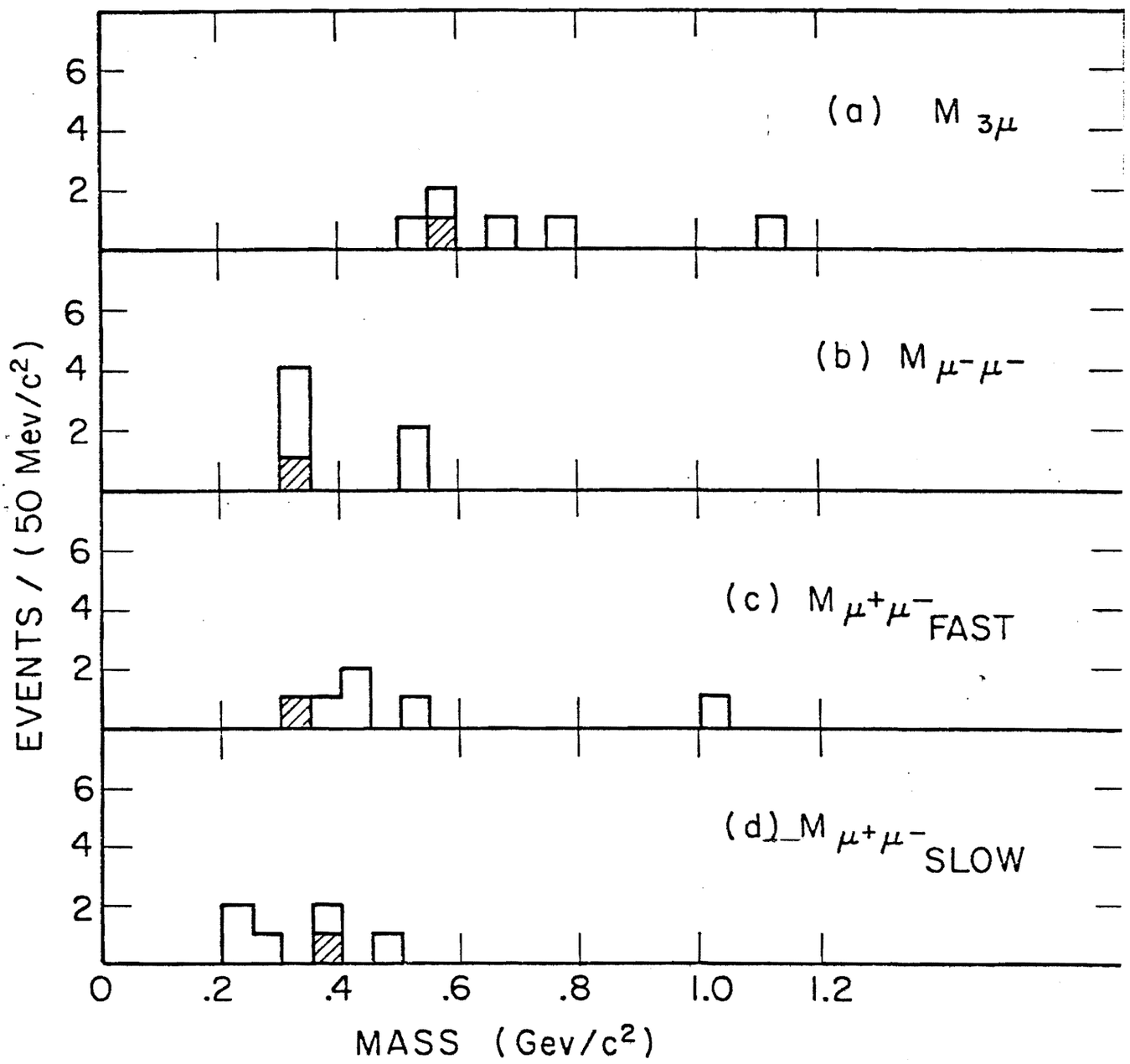

Figure 5-14. Effective mass distributions for the six trimuon events with missing energy greater than 1.5 Gev. The shaded event is the only one that indicated energy deposition in the leadglass target.

and again assuming an $A^{1.0}$ dependence and trident acceptances, we obtain a cross section

$$\sigma = 3.6^{+14.6}_{-3.6} \text{ pb/nucleon} \qquad (5.5)$$

It is important to note that this is the total cross section for a 10.5 Gev muon to induce a final state of three muons with energy $E > 2.2$ Gev and missing energy $\Delta E > 1.5$ Gev. The cross section quoted above is in qualitative agreement with a theoretical estimate for the inelastic Compton process assuming no restrictions on the final state. Hence, if indeed we are observing this type of reaction, we are seeing it at a level above what is expected theoretically.

Alternatively we can use the equivalent photon method to estimate the inelastic scattering cross section for quasi-real photons. The six events have $\langle Q^2 \rangle = .03$ Gev^2 and $\langle \nu \rangle = 8.7$ Gev where Q^2 is the square of the four-momentum transfer of the leading particle to the target and ν the energy loss. Dividing by the virtual photon flux factor for each event we obtain

$$(\gamma_v N \rightarrow \mu^+\mu^- + X) = .30^{+.50}_{-.09} \text{ nb/nucleon} \qquad (5.6)$$

All the restrictions on the final state described above apply here. This does not agree with the significant excess of events found in the photon scattering experiments of Caldwell et al.[7] and Davis et al.[8], as we would expect to

observe a cross section of 6.5 nb/proton for Bethe-Heitler pair-production (an elastic process) on a proton target.

5D. DIMUON EVENTS

As described in section 4B, a surprisingly large signal for the $\mu^+\mu^-$ (519 events) and $\mu^-\mu^-$ (557 events) final states was observed. A careful study of all possible conventional backgrounds that could induce this yield was necessary before any new physics could be claimed. In sections 3C-D the Monte Carlo calculation for dimuon final states arising from meson production and decay and from the detection of only two muons in a trident event was described. In this section the results of that calculation are compared with the data.

A useful variable for studying the dimuons is the missing energy $\Delta E = E_{in} - E_1 - E_2$. We expect 'trident dimuons' to cluster near $\Delta E = 0$ since the missed muon would have tho have low energy to escape detection. On the other hand, the production and decay of π and K mesons could leave substantial missing energy in the hadronic final state. In Figures 5-15,16 the ΔE distributions for the $\mu^+\mu^-$ and $\mu^-\mu^-$ samples are shown. There are 450 $\mu^+\mu^-$ and 223 $\mu^-\mu^-$ events which satisfy all of the 'tight' cuts applied to the trimuons plus the requirement of absolute muon identification. The dashed curves represent the yield expected from tridents, the dotted curves correspond to meson decay, and the solid curves the sum of the two contributions. Note that the normalizations of all curves have not been adjusted

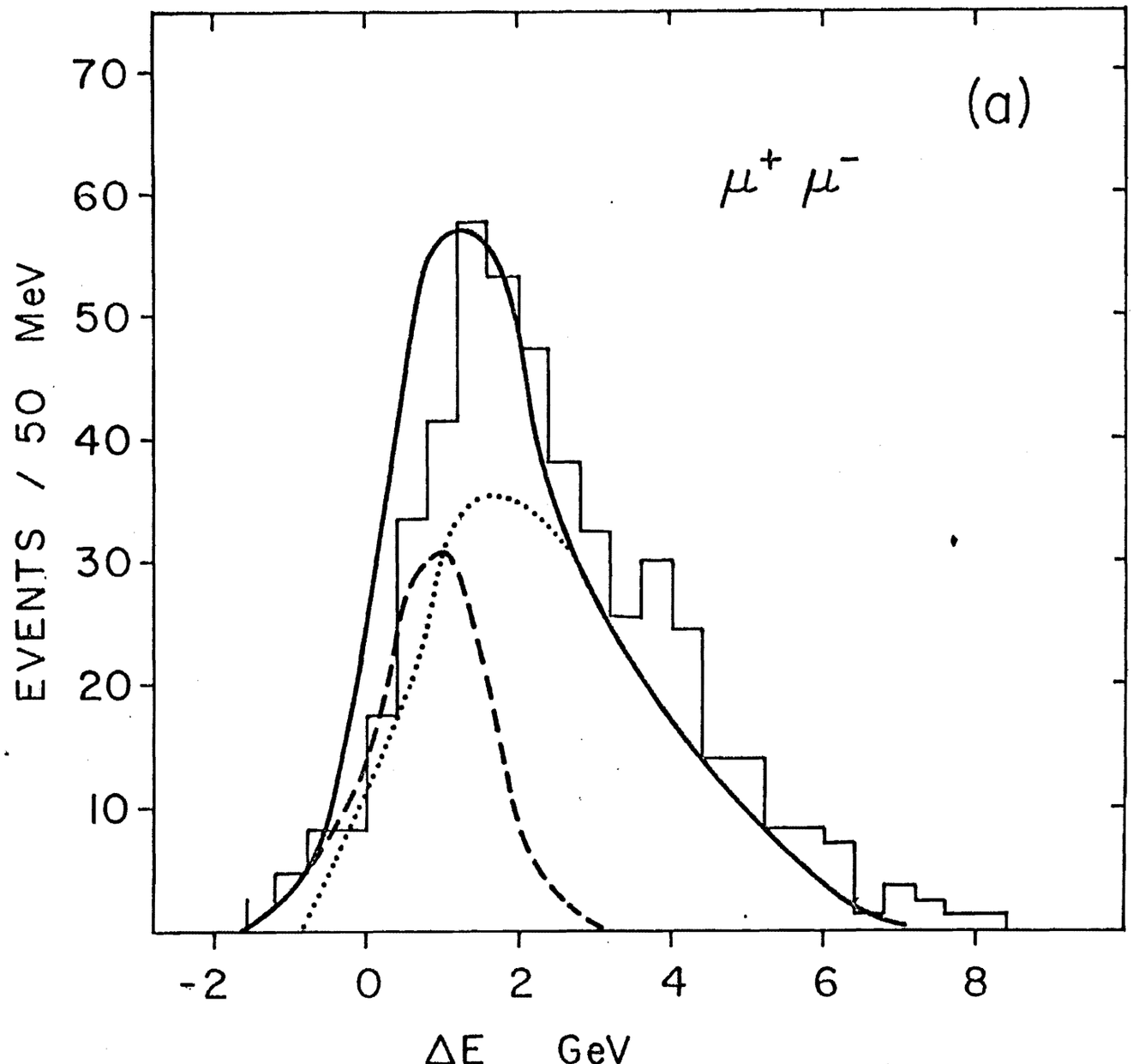

Figure 5-15. Event distribution in the missing energy for the $\mu^+\mu^-$ dimuons.

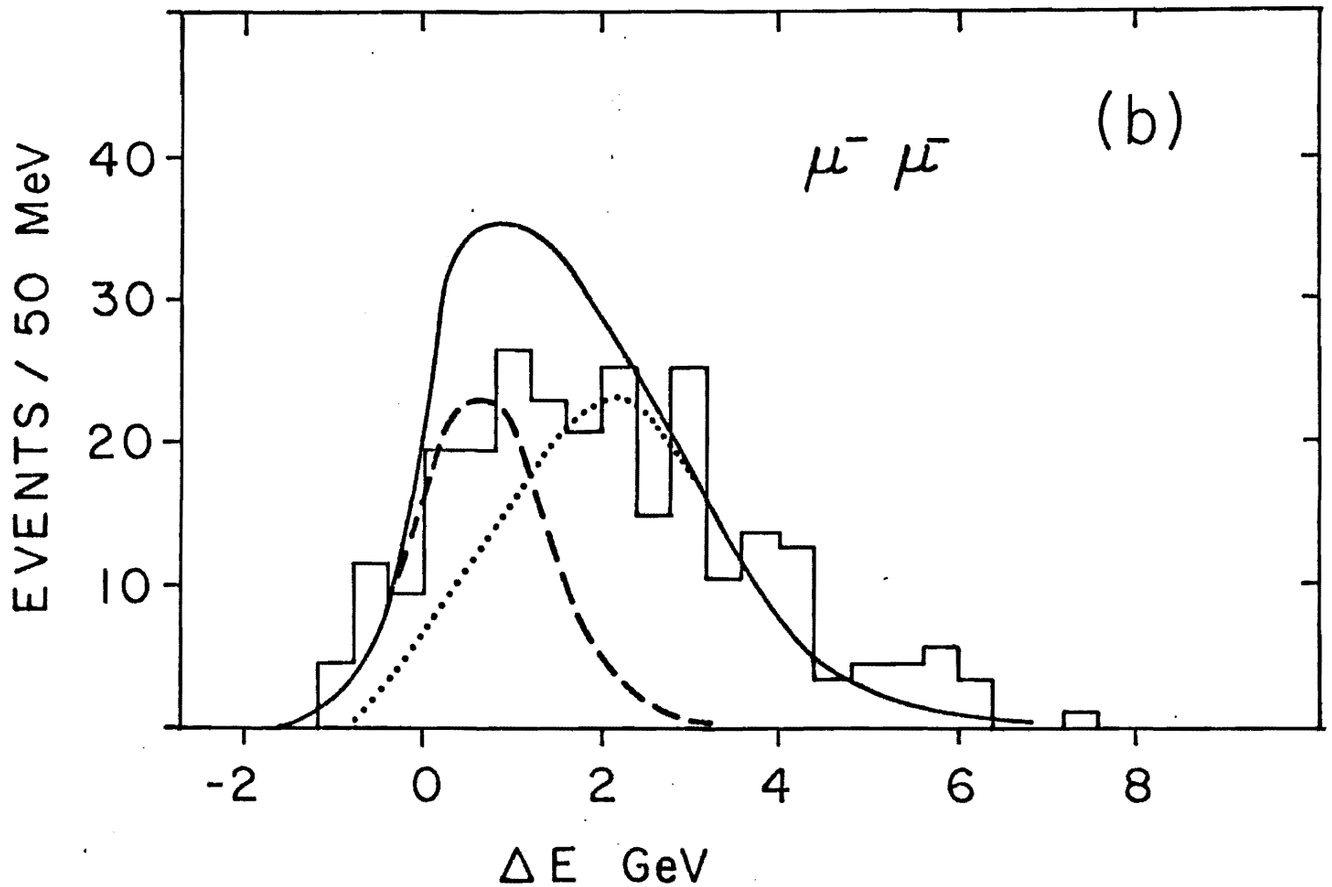

Figure 5-16. Event distribution in the missing energy for the $\mu^-\mu^-$ dimuons.

in any way. The agreement is surprisingly excellent considering the uncertainties in the Monte Carlo calculation (see section 3C). This agreement persists in other distributions.

For example, the effective mass of the muon pair is shown in Figures 5-17,18, again in comparison with the Monte Carlo predictions. We are forced to conclude that even if a genuine prompt single muon signal is there, it is impossible to separate it from the dominant backgrounds discussed above.

In Table 5-2 the actual dimuon yields are listed along with those expected from the Monte Carlo calculation for $\Delta E > -1$ Gev and $\Delta E > +2$ Gev. These numbers include corrections for detector and reconstruction efficiency. Note that for $\Delta E > 2$ Gev (data expected to have only a small contribution from trident production) there is a small excess of observed over predicted events. The systematic uncertainties in the Monte Carlo results prohibit interpreting this excess as a new source of prompt muons. However, an upper limit can be extracted from the 48 $\mu^+\mu^-$ and 17 $\mu^-\mu^-$ events above the predicted yields. At the 90% confidence level, the cross sections for the production of prompt single muons below charm and τ threshold satisfy

$$\begin{aligned} \sigma(\mu^+) &< 164 \text{ pb/nucleon} \\ \sigma(\mu^-) &< 81 \text{ pb/nucleon} \end{aligned} \qquad (5.7)$$

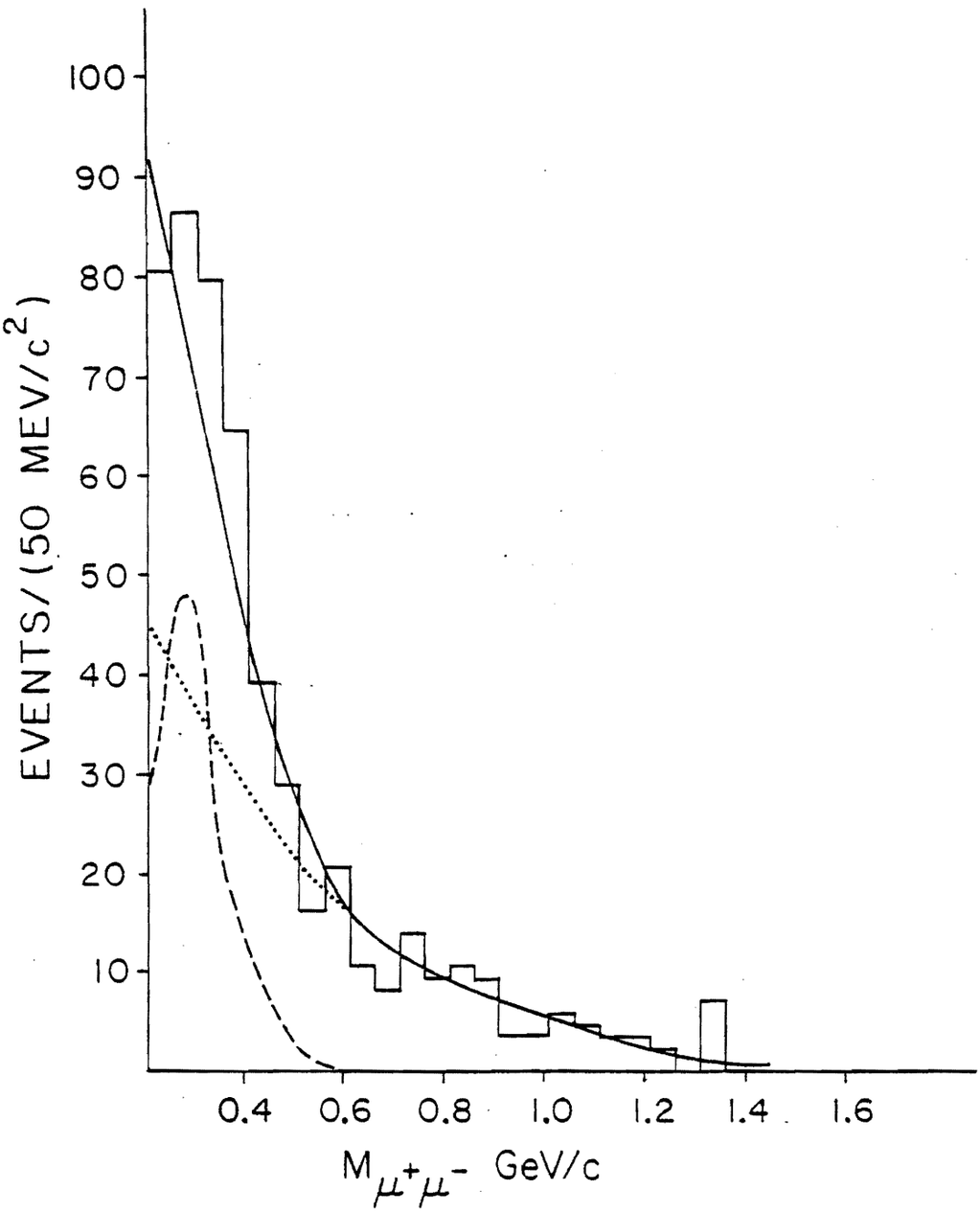

Figure 5-17. Event distribution in the effective mass of the $\mu^+\mu^-$ dimuons.

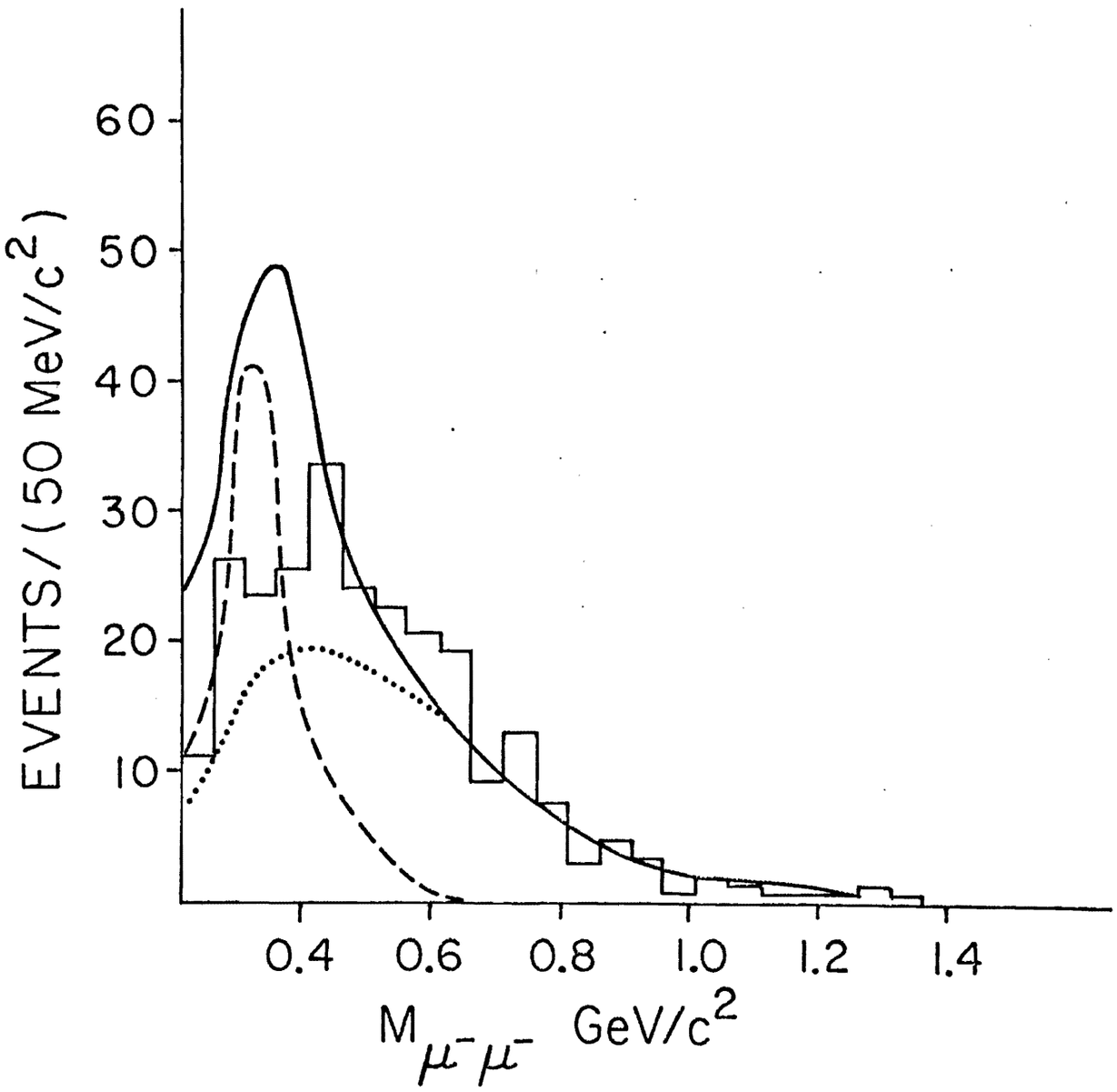

Figure 5-18. Event distribution in the effective mass of the $\mu\ \mu$ dimuons.

TABLE 5-2

Predicted and Observed Dimuon Events

	$\mu^+\mu^-$	$\mu^-\mu^-$
$E > -1$ Gev		
Monte Carlo		
Trident production	$143^{+}_{-}15$	$118^{+}_{-}12$
decay	$153^{+}_{-}20$	$131^{+}_{-}20$
K decay	$168^{+}_{-}26$	$59^{+}_{-}21$
Totals	$464^{+}_{-}36$	$308^{+}_{-}31$
Observed	$476^{+}_{-}23$	$256^{+}_{-}17$
$E > +2$ Gev		
Monte Carlo		
Trident production	$7^{+}_{-}2$	$5^{+}_{-}2$
decay	$83^{+}_{-}10$	$71^{+}_{-}10$
K decay	$117^{+}_{-}17$	$32^{+}_{-}11$
Totals	$207^{+}_{-}20$	$108^{+}_{-}15$
Observed	$256^{+}_{-}17$	$125^{+}_{-}12$

An interesting possibility discussed in section 1D was the production and decay of a neutral heavy lepton[9]

$$\mu^- p \rightarrow M^o n \quad (5.8)$$
$$\hookrightarrow \mu^+\mu^-$$

Since the ratio of positive to negative decay muons is known with more certainty than the absolute yield, and since M^o decay would only contribute to the $\mu^+\mu^-$ signal, we form the ratio

$$R = \left[\frac{\mu^+\mu^-}{\mu^-\mu^-}\right]_{OBSERVED} = \frac{(\mu^+\mu^-)_{BH} + (\mu^+\mu^-)_{DECAY} + (\mu^+\mu^-)_{M^o}}{(\mu^-\mu^-)_{BH} + (\mu^-\mu^-)_{DECAY}} \quad (5.9)$$

which gives a limit on events (90% C.L.)

$$N_{M^o} < 36^{+}_{-}78$$
$$B\sigma_{\mu^- N \rightarrow M^o X} < 100 \text{ pb/nucleon} \quad (5.10)$$

REFERENCES

1. J. Russell et al., Phys. Rev. Letts. 26, 46 (1971)

2. R. Sah, Harvard University thesis, 1970 (unpublished)

3. see for example C. del Papa et al., Phys. Rev. D19, 1303 (1979)

4. J. Martin et al., Phys. Letts. 65B, 483 (1976)

5. C. Bebek et al., Phys. Rev. D15, 3085 (1977); Phys. Rev. D15, 594 (1977); E. Lazarus et al., Phys. Rev. Letts. 29, 743 (1972)

6. P. Joos et al., Nucl. Phys. B113, 53 (1976)

7. D. Caldwell et al., Phys. Rev. Letts. 33, 868 (1974)

8. J. Davis et al., Phys. Rev. Letts. 19, 1356 (1972)

9. J. Bjorken and C. Llewellyn Smith, Phys. Rev. D7, 887 (1973)

10. J. Pati and A. Salam, Phys. Rev. Letts. 31, 661 (1973); Phys. Rev. D10, 275 (1975)

CONCLUSION

In summary, the characteristics of one and two muon production by 10.5 Gev/c muons on a heavy nuclear target have been studied. The most prevalent source of trimuons is the QED trident process. The observed total and differential cross sections are in excellent agreement with the predictions of QED. We have shown that muons exhibit exchange interference at a confidence level of 8 standard deviations. Approximately 10% of the trimuons are most likely due to vector meson production by virtual photons. We have searched for enhancements in the three-muon mass spectrum and observe no such effect at a level of about 10 pb/nucleon. We have observed 6 possible inelastic Compton scattering events which correspond to a cross section 5 pb/nucleon. Finally, the study of dimuon production shows (at the 100 pb/nucleon level) that single prompt muon production at these energies can be fully accounted for by the two known processes of trident production and meson decay.

APPENDIX I

Monte Carlo Integration of a Function

Consider an integrable function f(x) to be integrated over a range [a,b]

$$I = \int_a^b f(x)\, dx$$

Divide the interval into N subintervals of widths $\Delta_i x$, i=1,N and take the Riemann sum

$$I = \lim_{\substack{\Delta_i x \to 0 \\ N \to \infty}} \sum_{i=1}^{N} f(x_i)\ \Delta_i x$$

where x_i is the central value of x in $\Delta_i x$. Now suppose in each interval $\Delta_i x$ we choose at random n_i points x_{ij}, $j=1,n_i$ and calculate an average value of f from these points

$$\langle f(x_i) \rangle = \frac{1}{n_i} \sum_{j=1}^{n_i} f(x_{ij})$$

so we get

$$I = \lim_{\substack{\Delta_i x\ 0 \\ N \to \infty}} \sum_{i=1}^{N} \sum_{j=1}^{n_i} f(x_{ij})\ \frac{\Delta_i x}{n_i}$$

If each n_i gets very large, we can assume that each interval is uniformly populated with points so that

$$\rho_i = \frac{n_i}{\Delta_i x} = \rho = \text{density of points} = \text{constant}$$

$$I = \lim_{\substack{\Delta_i x \to 0 \\ N \to \infty}} \sum_{i=1}^{N} \sum_{j=1}^{n_i} \frac{f(x_{ij})}{\rho}$$

which becomes simply the sum over η ($= \sum_{i=1}^{N} n_i$) trials

$$I = \lim_{\to \infty} \sum_{k=1}^{\eta} \frac{f(x_k)}{\rho}$$

where

$$\rho = \frac{\eta}{\int_a^b dx} = \frac{\eta}{b-a}$$

Since η is always finite we must assign an error to I. We are summing a set of weights. If each weight were equal to one, the error on each weight would be one, therefore the error on each term is the weight itself. Combining all errors in quadrature we get that the error in I is the square root of the sum of the squares of the weights.

$$(\Delta I)^2 = \sum_{k=1}^{N} \frac{f(x_k)^2}{\rho^2}$$

This proof can be easily extended to a function of n variables $x_1, x_2, \ldots . x_n$ integrated over some volume V

$$I = \int_V f(x_1 \ldots\ldots x_n)\ dx_1 \ldots\ldots dx_n$$

$$= \sum_{k=1}^{N} \frac{f(x_{1k}, x_{2k}, \ldots\ldots x_{nk})}{\rho}$$

where

$$\rho = \frac{1}{N} \int_V dx_1 dx_2 \ldots\ldots dx_n$$

$$\Delta I^2 = \sum_{k=1}^{N} \frac{f(x_{1k}, x_{2k}, \ldots\ldots x_{nk})^2}{\rho}$$

APPENDIX II

Estimate of Trimuon Yield from Muon Bremstrahlung

The photon spectrum from muon bremstrahlung given by Tsai is

$$\rho(k)dk = \frac{T}{X_0}\left(\frac{m_e}{m_\mu}\right)^2 \left(\frac{4}{3} - \frac{4}{3}\frac{k}{E} + \frac{k^2}{E^2}\right)\frac{dk}{k}$$

where k is the photon energy, E the incident muon energy, T the target length, and X_o the target's radiation length. The non-lead content of the target will be ignored. Using the density and composition of the target given in Table 2-5 and taking a radiation length of lead to be 6.37 g cm^2

$$\text{lead density in target} = 2.24\ T\ \text{g cm}^2, \quad T \text{ in cm.}$$

$$\frac{T}{X_o} = \frac{2.24\ \text{g/cm}^2}{6.37\ \text{g/cm}^2} T = .352\ T$$

$$T = 32.4\ \text{cm} \qquad \frac{T}{X_0} = 11.4$$

Taking E = 10.5 Gev, the range of photon energy of interest is 3.6 Gev < k < 8.7 Gev since the scattered muon and the produced muons must all have E > 1.8 Gev. Thus the number of photons per incident muon is

$$N = \frac{T}{X_o}\left(\frac{m_e}{m_\mu}\right)^2 \int_{3.6}^{8.7} \frac{dk}{k}\left(\frac{4}{3} - \frac{4}{3}\frac{k}{E} + \frac{k^2}{E^2}\right) = 2.15 \times 10^{-4}\ \text{photons}/\mu$$

Next assume that all photons convert in the target. The number of muon pairs can be found from the ratio of the photoproduction cross sections of muons and electrons

$$\sigma_{\mu\mu} = 9.12 \times 10^{-29} \left(\frac{28}{9} \log \frac{2k}{m_\mu} - \frac{218}{27} \right) \text{cm}^2$$

$$\sigma_{ee} = 3.90 \times 10^{-24} \left(\frac{28}{9} \log \frac{2k}{m_e} - \frac{218}{27} \right) \text{cm}^2$$

$$\frac{\sigma_{\mu\mu}}{\sigma_{ee}} = 5.46 \times 10^{-6} \qquad \text{at } k = 3.6 \text{ Gev}$$

$$\frac{\sigma_{\mu\mu}}{\sigma_{ee}} = 7.48 \times 10^{-6} \qquad \text{at } k = 8.7 \text{ Gev}$$

$$N_{\mu\mu} \simeq (3.87 \times 10^{6})(7 \times 10^{-6}) = 27.1 \text{ muon pairs}$$

Assuming a flat energy distribution for the produced muons

$$f(k) = \text{fraction of pairs with } E_1, E_2 > 1.8 \text{ Gev}$$

$$= \frac{\int_{1.8}^{k-1.8} dE}{\int_{0}^{k} dE} = 1 - \frac{3.6}{k}$$

$$\langle f(k) \rangle = \frac{\int_{3.6}^{8.7} f(k)\ \rho(k)\ dk}{\int_{3.6}^{8.7} \rho(k)\ dk}$$

where $\rho(k)$ is given above.

$$\langle f(k) \rangle = .326$$

The acceptance for 'no exchange' tridents with $p_{1,2,3} > 1.8$ Gev/c is $\simeq$ 70%, therefore the number of observed bremstrahlung trimuons is

$$N_{3\mu} = (27.1)(.326)(.7) = 6.2 \text{ events}$$